March 2017

Astrophysical Accretion and Feedback: The Bayesian Linchpin of Theory and Observation

Shawn Roberts

ASTROPHYSICAL ACCRETION AND FEEDBACK: THE BAYESIAN LINCHPIN OF THEORY AND OBSERVATION

A Dissertation Presented

by

Shawn R. Roberts

Submitted to the Graduate School of the
University of Massachusetts Amherst in partial fulfillment
of the requirements for the degree of

DOCTOR OF PHILOSOPHY

February 2017

Astronomy

ASTROPHYSICAL ACCRETION AND FEEDBACK: THE BAYESIAN LINCHPIN OF THEORY AND OBSERVATION

A Dissertation Presented

by

Shawn R. Roberts

Approved as to style and content by:

Q. Daniel Wang, Chair

Michael Lavine, Member

Neal Katz, Member

Min Yun, Member

Stephen Schneider, Department Chair
Astronomy

DEDICATION

To Rob, without whom I would never have dreamed.

ACKNOWLEDGEMENTS

I would first like to thank my advisor, Daniel Wang, for always encouraging me to explore my own ideas and always having an open door. His open-minded mentorship has been a driving impetus behind much of my growth as a researcher and a human being.

I would also like to thank my collaborators (Yan-Fei Jiang, Jeremiah Ostriker, and Ya-Ping Li), with whom much of this work was done. I would like to thank the astronomy faculty at UMass for many interesting discussions, most notably Martin Weinberg, Neal Katz, and Houjun Mo. As for my fellow grad students: I would like to thank Christina Williams for listening with an open mind, Joe Burchett for having the best dance moves, Mike Petersen and Frank Ripple for never giving up despite the constant billiard beatings, Kati Grasha and Tim Conklin for keeping me sane during my first year in grad school, and Hansung Gim for always bringing a smile to the office and my face. I would like to thank Nevena Francetic, Andrew DeGroot, and Thompson Nguyen for their support during my last year of grad school.

Of course, these acknowledgements would be incomplete without mentioning the support of my family. I want to thank Kumi Ebihara for all of her love and support during my exit of grad school; I could not have done it without you. I want to thank Robert Weir for sparking the creativity and intellectuality in my life. Lastly, I would like to thank my parents for only ever offering encouragement.

ABSTRACT

ASTROPHYSICAL ACCRETION AND FEEDBACK: THE BAYESIAN LINCHPIN OF THEORY AND OBSERVATION

FEBRUARY 2017

SHAWN R. ROBERTS

B.Sc., UNIVERSITY OF NEBRASKA - LINCOLN

M.Sc., UNIVERSITY OF MASSACHUSETTS, AMHERST

Ph.D., UNIVERSITY OF MASSACHUSETTS AMHERST

Directed by: Professor Q. Daniel Wang

Despite being a major pillar of galaxy evolution, galactic feedback from stars and supermassive black holes (SMBHs) is subject to very little observational constraint. This is particularly true of the hot component, as viewed in X-rays. Yet, the hot component is directly linked to much of the energetic feedback released from these compact objects. X-ray observations suffer from several challenges that make placing this constraint a difficult task. In the face of considerable model uncertainty, these challenges underscore the need for novel X-ray data analysis techniques. In this dissertation, I seek to lend a unique perspective to X-ray data analysis and initiate the steps towards unravelling the hot component of galactic feedback. This is done through spatio-spectral fitting with Markov Chain Monte Carlo (MCMC). First, I fit 2D simulations of SMBH accretion to three separate bands of Chandra imaging data

of Sgr A*, the SMBH at our galactic center. In this study I place the first observational constraint on the angular momentum of accreting gas and self-consistently deconvolve residual point-like emission from the spatially extended accretion flow. I extend this analysis in Appendix B by re-examining the spectral energy distribution of Sgr A* from radio to X-ray. I find that a 1D accretion flow model cannot be reconciled with the more detailed X-ray modelling results. I further speculate on the origin of very steep synchrotron emission, suggesting that the residual point-like emission is accelerated by magnetic turbulence. Second, I describe the methodology for extracting spatial information from the RGS grating spectrometer onboard the XMM-Newton satellite. I demonstrate this method using 32 observations of M31 by fitting the OVIII Lyα and OVII Kα transitions. I show that the observed spectral peculiarities are much more likely the result of resonance scattering, rather than SMBH feedback effects seen through plasma overionization. A semiparametric extention of that work is also provided in an appendix. Finally, I conclude with a discussion of the usefulness of spatio-spectral analysis and highlight the promising research toward understanding galactic feedback that can be done as an extention to the work herein.

TABLE OF CONTENTS

LIST OF TABLES

LIST OF FIGURES

Figure **Page**

CHAPTER 1

GALAXY EVOLUTION: A TALE OF ACCRETION AND FEEDBACK

When observing galaxies in optical light, they typically appear quite tame. The "island universes" stretch through time *ad infinitum*; isolated, self-sustaining entities with no relationship to their apparent surrounding void. But visible light is only the tiniest piece of the puzzle. As we broaden our perspective, we discover the dynamically rich nature of the universe. At its heart lies an interconnected macrocosm, the cosmic web, directing the flow of baryonic matter [149, 109, 11]. Within this macrocosm, galaxies are delicate ecosystems, plagued by powerful and violent feedback events that regulate and drive evolution. Their stability is an illusion created by their vast scales and our inability to view the various galactic gas phases with optical light.

There are two ways that a galaxy can grow through the accretion of gas; smoothly from its surroundings or violently from a galactic merger (e.g., [62]). Both of these are primarily driven by one thing, the cosmic web. The cosmic web is a poeticism referring to the structure growth of dark matter, collisionless matter that does not interact with light. This dark matter comprises the vast majority of the universe's mass budget. Perturbations in the early universe led to density fluctuations that grow unabated, creating the web-like structure. Through gravity, it shapes the visible universe. Baryons are funnelled along the web's filaments to pool in halos. Halos at the intersection of many filaments house the richest clusters of galaxies, the most massive bound objects in the universe. But, the processes of structure growth on a macro scale are fairly well understood. Dark matter is simpler to theoretically deal

with due to its collisionless nature. Baryons, on the other hand, are much more nuanced.

Radiative cooling, which is unique to baryons, is the ultimate arbiter of all feedback processes through the creation of compact objects. Within collapsed regions of dark matter, if the temperature and density are conducive to cooling, the baryons will continue to collapse beyond and within the relaxed dark matter distribution. At some point, the baryons become compact enough that their self gravity locally dominates. After this tipping point, the gas undergoes a runaway collapse, typically fragmenting to form stars. As these stars evolve, they deposit energy and momentum into their local ISM through a variety of processes. If large enough, they will collapse in on themselves after expending their nuclear fuel, forming black holes. As BHs formed in the early universe they sowed the seeds of today's supermassive BHs (SMBHs), BHs with masses up to 10^{10} solar masses, found ubiquitously at the center of galaxies. Despite their small scale relative to the galaxy, stars and SMBHs are microcosms of feedback, collectively exerting their influence throughout the galaxy and beyond.

The feedback from SMBHs and stars has taken center stage in recent years. They are some of the last misunderstood foundational pieces of a fully functional model of galaxy evolution. Unfortunately, both of these feedback mechanisms operate in a highly non-linear way. Further, both deposit energy into their surroundings through multiple physically distinct modes. As such, they each suffer from many of the same unanswered questions. What is the dominant driver of feedback in each mode, mechanical energy or radiation? How efficient are the feedback processes? Where does the energy deposition occur? These are a few of the key questions that have very little observational constraint for current models of galaxy evolution.

1.1 SMBH Feedback

Black hole accretion is one of the most fundamental physical processes for energy generation in the universe. Current wisdom suggests that SMBH accretion is crucial for explaining a wide range of phenomena. In particular, it is widely believed that feedback from accreting SMBHs is instrumental for the regulation of galactic growth, most notably for galaxies that lie at the center of large halos ($M \geq 10^{13} M_{\odot}$) [38]. In these halos, star formation becomes extremely inefficient despite rapid cooling of the surrounding gas [39]. Presumably, this results from a preventative feedback mechanism. That is, the accreting SMBH keeps the gas surrounding these galaxies in a perpetually hot state, despite the fickle nature of SMBH luminosity. In addition, due to the fairly tight correlation between central black hole mass and and galactic bulge size, it is believed that the growth of SMBHs is strongly linked with the growth of galactic spheroids more generally [117].

SMBH accretion can be well demarcated into two regimes: those with high accretion rates, whose emission is well characterized by the thin disk model and are seen as the iconic high luminosity active galactic nuclei (HL-AGN or quasars), and those with low accretion rates, which result in low luminosity AGN (LL-AGN), where SMBHs spend the bulk of their time [38]. Both of these AGN modes offer a different flavor of feedback. HL-AGN are primarily associated with radiative feedback, while LL-AGN are characterized by kinetic feedback in form of jets. Both modes have an uncertain amount of kinetic feedback from magnetically driven winds. While the feedback from HL-AGN is much more violent, the relatively gentle feedback from LL-AGN is much more long lived, and therefore may have a more prominent role in the regulation of star formation. While current estimates suggest the HL-AGN phase lasts $\sim 10^5$ years [111], the frequency/duration decomposition between the two modes and the coupling of their generated radiative and kinetic energy to the galactic environment, and therefore role in feedback, are still not well understood.

As noted above, the emission from HL-AGN can be well modelled with the standard thin disk [98]. In the HL-AGN phase, the density of accreting gas becomes great enough that cooling is very efficient. This allows the gas to cool, condense, and flatten out into a disk that is supported by angular momentum. Viscous stress causes this disk to heat (energy that is efficiently radiated away) and siphon material inward. Because of the high density, the emission is optically thick and can be treated as approximately a blackbody, "approximately" because the disk spans a range of temperatures. The radiation from the disk typically dwarfs that of the host galaxy by several orders of magnitude in the optical, making the galaxy appear as if it is a point source. Other emission components exist that combine to explain not only the emission in different bands, but also different viewing geometries. These components can also typically be well separated due to their individual dominance in different wavebands. For example, above and below the disk, a hot corona of magnetically excited particles exists, which exposes itself in the X-ray as a powerlaw. However, one should not be overconfident due to our ability to model the emission of HL-AGN. Although this radiation may drive feedback, illuminating the importance of this feedback further requires an understanding of the dynamics involved. In the case of SMBH feedback, processes important for shaping the dynamics span a incomprehensible range in spatial scale.

The most obvious source of feedback from HL-AGN is radiation. Radiation will do two things to the surrounding gas: ionize it and, if the optical depth is great enough, drive an outflow. The ionization can persist in the form of an AGN relic, which has recently been proposed to be responsible for the diffuse X-ray excesses observed in galactic nuclear regions (e.g., [130, 110]), as well as the ionization of cool gas far away from post-active galaxies (e.g., [103, 59]). Secondly, if the surrounding gas and dust are optically thick to the accretion disk's radiation field, most of the radiation will be absorbed and re-radiated in the IR. A large dust presence will result

in multiple scatterings in the IR, further boosting the momentum deposition. The typical scaling employed in simulations is $\dot{p}_{rad} \propto (1 + \tau_{IR}) L_{incident}$, where τ_{IR} is the optical depth in the IR and $L_{incident}$ is the luminosity incident on the gas/dust [52]. The combined pressure from a strong radiation field and multiple scatterings can then serve to overcome the gravitational potentail of the galaxy. Given the luminosity of HL-AGN and the typical dust content of their surroundings, [38] estimates that radiation pressure from SMBH feedback could effectively overcome the gravity from a galaxy one thousand times more massive than the host galaxy. Therefore, radiation pressure likely provides more than enough energy to eject gas from the galaxy.

Radiation is not the only possible driver of galactic winds. For both HL-AGN and LL-AGN there is an uncertain contribution from magnetically driven winds to feedback. This wind has not been observed directly for LL-AGN because it is so tenuous. Simulations, however, suggest that it exists, albeit with an unclear connection to the surrounding gas. For some HL-AGN, winds are observed in the X-ray and UV through absorption lines that show velocities of 1×10^4 km/s [97, 125, 44]. However, it has proven difficult to determine the total covering fraction as well as the radial location of the wind, obscuring estimates of the total kinetic power of the wind. Yet, current best estimates place it at $\sim 5 - 10\%$ of the accretion power [34].

The emission from LL-AGN is distinctly enigmatic, largely due to the inherent difficulty of separating the various emission components. This puts researchers in a difficult position. While HL-AGN emission is well modelled, allowing us to set boundary conditions for that mode of AGN feedback, LL-AGN have no such luxury, at least for the winds. Since the outflowing gas is unobservably tenuous it becomes impossible to estimate the outflow's effects on its surroundings without understanding the nature of the accretion that drives it. The compelete lack of a sufficiently constrained model of the accretion flow prevents any realistic inquiry into the feedback, which is highly dependent on the nuances of the accretion flow, such as angular mo-

mentum. These circumstances have given rise to a plethora of radiatively inefficient (RIAF) and advection dominated accretion flow models, which are characterized by accretion-comparable outflows and the advection of energy into the SMBH. While these models broadly explain the gross features of the quiescent emission from the nearest LL-AGN, Sgr A*, including radiative efficiency and low resolution spectrum [90], we will see later that this is largely due to a lack of self-consistent modelling of the spatial and spectral information provided by the data.

Jets and bubbles are the most commonly observed manifestation of feedback from LL-AGN in galaxy clusters and massive galaxies (e.g., [87, 75]). Relativistic jets, typically bipolar, supersonically drill through their immediate surroundings. In doing so, they shock gas and inflate bubbles of relativistic, non-thermal plasma. Bubbles then bouyantly rise in the hot cluster atomosphere, transporting energy with them. Based on the strong anti-correlation between cooling time and observed bubble presence, we expect bubbling to be a relatively continuous process [35]. Further, since turbulent energy is only $\sim 10\%$ of thermal energy within the bubble, we believe the bubbling process is also fairly gentle [40, 41].

Through bubbles, jets appear to provide the means for efficient preventative feedback in large-mass halos. Given the bubble volume, surrounding pressure, and bouyancy time, one can estimate the total kinetic power in the jets. This, of course, assumes one can reliably estimate the surrounding pressure by estimating the temperature and density with X-ray observations, which, as we will see throughout much of this work, is less straightforward than we might presume. Nevertheless, estimates of this power are typically in good agreement with the energy loss estimated from radiative cooling in the surrounding gas [102, 101, 85]. However, the location of energy deposition from bouyant bubbles is extremely uncertain as X-rays cannot be used to observe the hot gas to large radii.

1.2 Stellar Feedback

Stellar feedback can also be split into two regimes, feedback related to star formation and late-time stellar feedback. Feedback from star formation directly regulates star formation in galaxies that are actively forming stars by expelling gas from the galactic reservoir. Such feedback prevents extended periods of heavy star formation. Late-time stellar feedback, on the other hand, may be significant in galaxies with a large aged population and very little star formation. In these galaxies, it may input enough energy into the surrounding gas to prevent star formation from initiating.

Late-time stellar feedback is the least understood of the two stellar feedback regimes. In galactic spheroids, Type Ia supernovae (SNe) deposit energy and momentum into the local interstellar medium (ISM). Simulations suggest these SNe may create hot, bouyant bubbles that transport energy out of the deep galactic potential [123]. There is some anecdotal observational support for this interpretation (e.g., [45, 21, 22, 55, 49, 80]). Unfortunately, due to non-thermal emission contamination, this evidence is highly suspect (e.g., [77]). There is also the additional complication of AGN feedback in these same galaxies. Deconvolving the relative contribution between AGN and late-time stellar feedback in galactic spheroids is non-trivial, as both can potentially serve to fuel galatic outflows.

Star formation feedback is in a similar regime of understanding as SMBH feedback. We have a fair understanding of the energetics and rate of Type II SNe [69]. We also have a solid framework for the feedback from high mass stars in the form of stellar winds and radiation [69]. However, we don't understand how these different forms of feedback combine and couple with the surrounding medium to collectively drive galactic scale outflows. The change of scale from individual stars through galaxies and beyond to the intergalactic medium (IGM) prevents us from simulating this evolution directly from first principles (e.g., [26, 129, 51]). Further, the multiphase nature of star formation driven galactic outflows leads to complex emission structure

that quickly becomes too diffuse to reasonably observe as this outflow expands from the galactic plane. This leaves us with little understanding as to the true energetics and ultimate fate of these outflows.

There are three primary mechanisms by which stars expel matter and energy into their surroundings: stellar winds, radiation pressure, and SNe. All three of these directly inject momentum into the local ISM. Additionally, stellar winds and SNe both add heat by shocking surrounding gas. The primary source of constraint on the power of different stellar feedback mechanisms is through simulations. This is typically done through ad-hoc sub-grid implementations, required by the extreme dynamic range in spatial and mass resolution. In general, it is believed that all of these feedback processes are important for generating galactic winds [52, 71]. However, the relative contribution of each is highly dependent upon the physical circumstances.

At high redshift, where galactic density was much higher, energy input from SNe and stellar winds is quickly radiated away. Therefore, the primary mechanism of feedback is through radiation pressure from massive stars, in a similar manner as discussed above for SMBH feedback. Radiation pressure in the high redshift universe was not terribly efficient, due to a low metallicity and thus low dust content. However, it still managed to drive gas out of galaxies with a mass loading (the ratio of the mass outflow rate to the star formation rate) of approximately unity [52].

In the local universe, stellar feedback is much more efficient. Stellar winds, SNe, and radiation pressure combine non-linearly to drive out ~ 10 times as much gas as forms stars for a Milky Way like galaxy[52]. For lower mass galaxies this efficiency increases, as the density decreases. For a Small Magellenic Cloud size galaxy ($n \leq 0.1$ cm^{-3}), the density is so low that the cooling time is greater than the dynamical time. This leads to a highly efficient coupling of energy inputs from stellar winds and SNe that can drive gas out of the relatively shallow gravitational potential with ease.

1.3 Of X-ray Observations

X-ray observations trace plasma at temperatures of $\sim 1 \times 10^{6-8}$K. As such, they give us a way to directly observe many of the feedback processes discussed above. Further, understanding the hot phase of feedback is extremely important. For example, it is believed that the majority of energy and metals in star formation driven outflows are carried by the hot phase [71]. Diffuse soft X-ray emission has commonly been used to trace various types of galactic feedback. Assuming an origin of this emission in optically-thin thermal (collisionally-excited) hot plasma, one may estimate its mass, energy, and chemical contents and even its outflow rate from a galaxy.

Charge coupled devices (CCDs) are the standard technology for X-ray detectors. CCDs utilize the photoelectric effect to detect photons. As photons strike a semiconductor, they eject electrons. X-ray photons are of sufficient energy that a single photon liberates many electrons, tens to thousands. Further, the number of ejected electrons is approximately linearly proportional to photon energy. For example, for silicon the number of electrons ejected is equal to $E/3.7$, where E is the photon energy in eV. This porperty of CCDs has a unique and useful side effect for X-ray astronomy. Since the flux of X-ray photons is very low, we can read out and detect individual photons. And since the number of photoelectrically ejected electrons is proportional to photon energy, we are able to obtain spectral information in addition to imaging information in *every* observervation.

There are three X-ray telescopes that bare mentioning: *Suzaku*, *XMM-Newton*, and *Chandra*. Each provides it's own niche in terms of capabilities. *Suzaku* has the best effective area at low energies and lowest background of any imaging CCD due to it's low Earth orbit. Utilizing all of its CCDs in tandem makes it the telescope with the greatest effective area. It also has comparable spectral resolution to the *Chandra* ACIS systems. Unfortunately, its spatial resolution is limiting with a point spread function (PSF) full width half maximum (FWHM) of 1.8 arcmin. Therefore, the

Table 1.1. Basic properties of the *Chandra* ACIS-I and *XMM-Newton* RGS systems.

	Chandra ACIS-I	XMM-Newton RGS
Bandpass (keV)	0.3-10	0.35-2.5
Effective Area (cm^2 at peak)	580	120
Field of View	17 x 17 amin	N/A x 4.4 amin
PSF FWHM (arcsec)	0.5	15
Spectral Resolution (eV)	140	1.2

two instruments chosen for the analyses herein are the *Chandra* ACIS-I and *XMM-Newton* RGS. These were chosen because of the superior spatial resolution of *Chandra* ACIS-I and the unprecedented spectral resolution of the *XMM-Newton* RGS. A basic summary of their properties are shown in Table 1.1.

The *XMM-Newton* RGS system takes advantage of reflection to create a very high resolution spectrum, FWHM $\sim$ 1.2 eV. This is done by creating a mirror etched with very fine grooves. The grooves create a distance differential to an illuminating surface between the peaks and troughs of the mirror. Due to the differential in time required to reach an illuminated surface, an interference pattern will arise. Where they constructively interfere, that is, strike the surface in phase, an intesity maximum occurs. By using many grooves, the intensity maxima are spatially concentrated. Further, the location of constructive inteference is wavelength dependent. Combining these properties allows for the extraction of a spectrum with the grating. To mitigate effective area losses, the entire FOV is dispersed by the X-ray grating. Therefore, if a source is extended, the observed spectrum will consist of overlapping images of the source at each wavelength, leading to a mixture of spatial and spectral information.

Chandra was launched by NASA in 1999 and is currently expected to last for at least another decade. It is unique in that the thickness and high quality polishing of its mirror assembly allows for extremely high spatial resolution, FWHM $\sim$ 0.5 arcsec. This resolution is more than an order of magnitude better than other current X-ray telescopes. As such, Chandra is primarily used for imaging analyses. Although, it

should be noted that Chandra is also equipped with two grating spectrometers. They have a comparable effective area (in general) and spectral resolution to the RGS, but have different energy coverage. RGS does have a significantly higher effective area for soft X-rays in the range of 0.5-1 keV. However, the primary issue with the Chandra grating systems is that their dispersion is considerably smaller than the RGS, leading to spatial/spectral confusion for even mildly extended sources.

Recall, the X-ray regime is photon starved. Thus, we are able to count individual photons. In addition to providing a moderate resolution spectrum with every observation, this puts X-ray astrophysics in the realm of Poisson statistics. X-ray pixel counts are drawn from a Poisson distribution, a discrete distribution that corresponds to the number of events expected in a given time frame. The likelihood function has the following form:

$$P(N) = \frac{\lambda^N e^{-\lambda}}{N!} \tag{1.1}$$

where N is the observed counts and λ is the expected number of counts. For a source with some flux, F:

$$\lambda = F \times A \times t \tag{1.2}$$

where A is the effective area of the instrument and t is the exposure time of an observation. This functional form is assumed for the likelihood throughout this work.

1.4 He-Like Line Diagnostics

Above we noted the potential to estimate the chemical composition, outflow velocity, and outflow mass, assuming the emission is optically-thin and thermal. However, X-ray emission can be seriously contaminated, if not dominated, by non-collisional equilibrium (non-CIE) processes or optical depth effects[1] [104, 77, 146]. This is par-

[1]For brevity sake, we will discuss both of these under the umbrella of non-CIE, as the standard assumption is that the plasma is optically-thin and in CIE.

ticularly true when feedback is involved, due to its violent nature. These non-CIE contributions must be quantified before we can reliably use the diffuse soft X-ray emission to trace galactic feedback and its impact on the galactic ecosystem. Within the X-ray domain, the most powerful probes of the presence of galactic feedback and its effects on hot gas through non-CIE emission are Helium-like Kα line diagnostics. Not only are they useful diagnostics, but they are also some of the most prominent features in an X-ray spectrum.

Unfortunately, the modelling of most non-CIE emission processes can be considered in infancy, making it very difficult to measure the physical conditions in the plasma. As such, current attempts focus on using this line diagnostic to identify when non-CIE emission is important and what type of emission it is, if possible. For a grating spectrum, such as RGS, the identification of non-CIE emission is somewhat trivial (e.g., [77]). For a moderate resolution CCD spectrum, where individual diagnostic lines are completely unresolved, identification is less straightforward. However, it can be done with significant calibration [107]. The larger challenge is determining the physical cause of the non-CIE emission. However, as discussed below, each form of non-CIE emission produces its own spatial pattern. Therefore, a combined spatial and spectral analysis may be needed to illuminate physical mechanisms and disentangle the true plasma conditions.

The He-like Kα transition corresponds to a transition from the first excited state to the ground state (Figure 1.1). It consists of four lines, however two of them are so close in energy that the transition is routinely called a triplet, consisting of the resonance, inter-combination, and forbidden lines. The resonance line (R) is an allowed transition and is the strongest line for thermal emission, where electron populations are controlled by collisions. The semi-forbidden transitions are collectively called the inter-combination line (I). They are the weakest with a combined flux of about a tenth of the resonance line for thermal emission at the relevant densities. Lastly, the

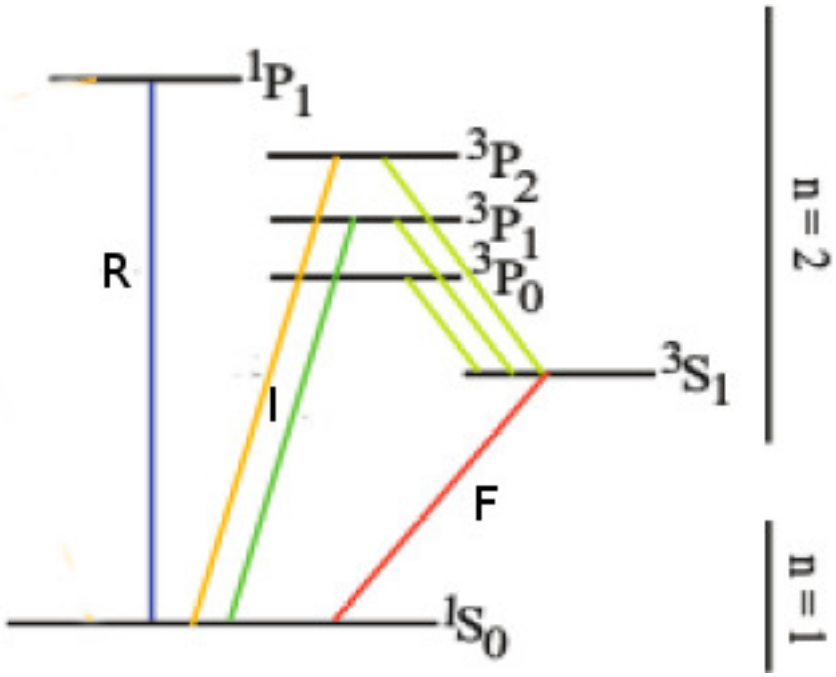

Figure 1.1. Simplified Grotian Diagram for a He-like ion. Original image in [120].

forbidden line (F) is stronger than the intercombination line for the herein relevant densities, it's flux being approximately half that of the resonance line. This forbidden line is extremely sensitive to feedback through non-CIE processes. It's flux relative to the resonance line can be enhanced by more than an order of magnitude due to a slew of processes, most notably charge exchange (CX) and non-equilibrium ionization. We encapsulate the Kα diagnostic power in the G-ratio = $\frac{F+I}{R}$ [95].

A recombination-dominated plasma, or an over-ionized plasma, occurs when electron levels are governed by the radiation field or for some finite time after the removal of a strong radiation field, respectively. Such may be the case when an AGN goes into quasar mode (an HL-AGN) [23, 84, 113]. In this case, the electron temperature is much lower than the ionic temperature. As such, electron levels are populated primarily through recombination, which favors the forbidden line. Similarly, for some time after the AGN transitions to an LL-AGN, the electron populations will continue to be populated by recombinations (a relic AGN). The duration of this effect is dependent upon the local density. As such, it will produce a characteristic spatio-spectral

imprint. For a spheroidal galaxy, where the density is a maximum at low radii and continuously decreases as we move to larger radii, we can expect the G-ratio to be its lowest in the center of the galaxy and asymptotically approach the fiducial value of a recombination-dominated plasma at large radii.

CX is a special case of inelastic collision in which one or more electrons is exchanged between an ion and most likely neutral hydrogen. As the colliding particles approach each other, their potentials overlap, allowing the photonless exchange and subsequent cascade of the captured electron. This is an extremely efficient process with a relatively large reaction cross section (about 5 orders of magnitude greater than for electron collisional excitation). If the capturing ion is sufficiently ionized (e.g. OVIII) then the cascading is expected to result in X-ray emission. Thus, in principle, X-ray emitting CX can be an important process at any astrophysical site where heavily ionized species interact with neutrals. It has been proposed and studied in a wide range of X-ray sources, from planetary atmospheres [29, 30, 63] through supernova remnants (SNR) [57, 107], individual star-forming complexes [126] and star-forming galaxies [127, 76, 78] to the cores of clusters [42].

For the sake of understanding feedback, particularly that of star formation driven, we need to have a full accounting of the effects of CX to the emission of galactic winds. We know from infrared observations that a significant amount lowly ionized species and molecules exists entrained within galactic outflows (e.g., [7]). Further, we know that the G-ratio is elevated relative to thermal for observations of starbursting galaxies, such as M82 (e..g, [77]). Both of these facts suggest CX is likely important for the modelling of X-ray emission concerned with galactic outflows associated with strong stellar feedback. Therefore, without including CX in our modelling, we are likely to arrive at grotesquely incorrect estimates of outflow mass and metal content (e.g., [57]). Due to the multiphase mixing required for CX, it can be diagnosed via the G-ratio's spatial correlation with emission at longer wavelengths, such as Hα [107].

A final process that should be kept in mind is that of resonance scattering. When the line-of-sight integrated density becomes large enough that the plasma is no longer optically thin, the resonance line, which has a much higher oscillator strength than the inter-combination and forbidden lines, may be scattered out of the line-of-sight [96]. Fortunately, this process can also be spatio-spectrally identified, depending on source geometry. For example, assuming spherical symmetry, as resonance photons are scattered out of the line-of-sight where the optical depth is greatest, they must emerge on the source edges, where the optical depth is minimal. Therefore, the object integrated G-ratio will remain that of thermal. However, the G-ratio will be elevated at source center and depressed on the edges.

Currently, the bulk of feedback understanding is built upon theoretical studies. Observationally, these effects have been much harder to pin down. However, it is very important that we are able to place observational constraints. Computational studies lack the power to simulate feedback from first principles through the necessary dynamic spatial range. Instead, they resort to ad-hoc prescriptions that can vary drastically in their nuances while still broadly matching large-scale statistical properties. Therefore, observationally tethering these simulations is one of the most difficult challenges in astronomy at this time.

There are many reasons why observational progress has not been forthcoming in this respect. The one clarity, between the three emission mechanisms discussed above, is just how poor the thermal assumption is when trying to estimate the effects of feedback. First, it is extremely difficult to ascertain the important emission mechanisms without high spectral resolution. Second, the current fleet of high spectral resolution instruments are designed in such a way that one has to compromise on effective area. Third, the instruments with high spectral resolution are designed in a way that serves to confuse spatial and spectral information. While this may not be an issue for very mildly diffuse sources, for at least moderately diffuse sources this

leads to a blending of important diagnostic lines, making it difficult to disentangle the spatial and spectral information. Lastly, modelling capabilities of non-CIE processes have been slow in coming, with most currently in an alpha stage. These challenges underscore the need for novel data analysis and modelling approaches.

1.5 Bayesian Inference

The unique quality of Bayesian inference is its treatment of model parameters. As opposed to treating parameters as fixed but unknown quantities, they are themselves treated as random variables. As we will see, this has two consequences that are of practical use. For one, this provides a framework for the straightforward incorporation of information from past experiments. Secondly, in a Bayesian framework we directly compute the conditional distribution of model parameters given the observed data and any prior information we choose to include. From a pragmatic point of view, this provides a simple and flexible framework for all statistical needs as a scientist, where parameter uncertainty is equally as important as best fit values.

Bayesian inference is formalized, somewhat simplistically, in Bayes' Theorem [5]:

$$P(\vec{\theta}|\vec{D}) = \frac{P(\vec{D}|\vec{\theta})P(\vec{\theta})}{P(\vec{D})} \tag{1.3}$$

where $P(\vec{\theta}|\vec{D})$ is the probability of the parameters given the data (or posterior predictive probability), $P(\vec{D}|\vec{\theta})$ is the probability of the data given the model parameters (the likelihood), $P(\vec{\theta})$ encapsulates any prior knowledge about the model parameters before the current experiment (the prior), and $P(\vec{D})$ is the probability of the data (the evidence). This framework provides a natural way to derive a best fit model and parameter credibility. The unfortunate feature of this equation, prior to modern computing power and techniques, is the evidence. The evidence can be written more explicitly as:

$$P(\vec{D}) = \int P(\vec{D}|\vec{\theta})P(\vec{\theta})\mathrm{d}\vec{\theta} \tag{1.4}$$

In this form, it becomes much more clear why direct analytical calculation of Bayes' Theorem is problematic. Calculating the evidence requires integrating the likelihood and prior over all parameters, something that is intractable for all but the most basic models.

In order to get around the intractability of the evidence, Markov Chain Monte Carlo (MCMC) techniques have been used to estimate the posterior distribution of parameters. This class of methods produce as their output a correlated sample from the joint posterior distribution. In this work, we will exclusively use the *Metropolis-Hastings* (MH) algorithm due to its simplicity and generality. However, it should be noted that recent developments have led to much more efficient sampling algorithms, such as the No U-Turn Sampler (NUTS) [50].

Since the evidence is not a function of the model parameters, the MH algorithm circumvents the evidence entirely as it only requires a function proportional to the function being sampled. This necessitates that the MH algorithm is a rejection sampler. For some number of samples, N, we randomly draw a new parameter set $\vec{\theta}^*$ from a user defined probability distribution $P(\vec{\theta}|\vec{\theta}^{t-1})$. [2] We further take a random uniform draw from 0 to 1, u. If u is then less than the ratio of the posterior probability of the new parameter set to the posterior odds of the old parameter set, then we accept the step, that is, update the parameters. The *Metropolis-Hastings* algorithm is formalized in Algorithm 1. By opening up Bayesian inference to a much broader class of model and prior formulation, this simple algorithm encapsulates immense power.

[2] For the case of the MH algorithm, the proposal distribution must be tuned. As one can imagine, in high dimensions this tuning is impractical. Therefore, in practice, we implement the algorithm in a component-wise fashion, which simplifies proposal tuning.

Algorithm 1 Component-wise Metroplis Hastings MCMC Sampling

procedure MH_SAMPLE
  for t **in** N **do**
    for θ_i **in** $\vec{\theta}$ **do** ▷ Sample parameters individually
      Draw θ_i^* from $P(\theta_i|\theta_i^{t-1})$
      $u \leftarrow$ uniform_random$[0, 1]$
      if $u \leq \frac{P(\vec{D}|\vec{\theta}^*)P(\vec{\theta}^*)}{P(\vec{D}|\vec{\theta}^{t-1})P(\vec{\theta}^{t-1})}$ **then** ▷ Accept the step
        $\theta_i^t \leftarrow \theta_i^*$
      else
        $\theta_i^t \leftarrow \theta_i^{t-1}$
      end if
    end for
  end for
end procedure

1.6 Thesis Overview

The goal of this work is to explore novel ways to extract information from X-ray data and in doing so push the boundaries of current observational constraints on galactic feedback. In Chapter 2, we take advantage of the high angular resolution of Chandra to resolve and develop a self-consistent spatiospectral model of our Galaxy's central accretion flow, the primary target of opportunity for studying feedback from LL-AGN. In Chapter 3, we present a new method for analysing the dispersed XMM-Newton RGS data, with implications for both SMBH and star formation feedback. We demonstrate this method on the galactic bulge of the nearest spiral galaxy, M31 (Andromeda). We further discuss the possiblities of adding observational constraints to nearly each form of feedback using this method. In Chapter 4 we discuss the limitations of current X-ray imaging and spectral analyses, the pragmatism of the Bayesian framework, and a possible path forward for illuminating the hot component of galactic feedback.

CHAPTER 2

THE SGR A* ACCRETION FLOW

2.1 Introduction

Supermassive black holes (SMBHs) spend the majority of their lives in a low-luminosity/accretion phase ($\sim$90%; [140]). A common way to refer to these objects is as low-luminosity active galactic nuclei, or LL-AGN. The emission from these LL-AGN is very much enigmatic, largely due to the inherent difficulty of separating the various entangled emission components [131, 72]. Predominantly, there are two unique radiative X-ray phenomena that characterize the emission from LL-AGN; their extremely low, spatially extended quiescent luminosity, and flares that can briefly increase their luminosity by up to a factor of 100 approximately bidaily [1, 143]. Physically, even though these BHs are associated with much lower net accretion rates, they may also be associated with strong mechanical feedback phenomena such as giant radio bubbles [86] and collimated outflowing winds. However, connecting the physical processes around BHs to the observed feedback effects in a self-consistent manner remains a challenge.

As all accreting and outflowing material must flow through the quiescent, spatially extended accretion flow, its emission will be the focus of this study. For the sake of observational capabilities, this includes both the spatially extended accretion flow as well as the unresolved point-like emission processes (minus the detected flares) immediately surrounding the SMBH. Further, we have a perfect candidate to study LL-AGN emission in our own galaxy, Sgr A*, which already has a wealth of data

available through a wide range of wavelength bands [115, 43, 1, 2, 53, 147, 81, 36, 131, 17].

In X-rays, the Sgr A* quiescent accretion flow is spatially resolved to $\sim$ 1.4" [2]. This radius, estimated from the analysis of projected X-ray emission in the surrounding field, is roughly consistent with the classical Bondi radius, r_b, enabling the estimate of the rate at which gas is captured by the BH ($\dot{M}_b \sim 10^{-5}$ $M_\odot$ year^{-1})[1]. The Bondi radius is an atavism to the original way these objects were studied. Bondi accretion, from which it derives its name, assumes the accretion flow to be spherically symmetric, with approximately zero angular momentum [12]. In this scenario, any ambient material that enters the Bondi radius, the radius at which the gas thermal energy is equivalent to the gravitational potential energy, is doomed to fall into the BH. Unless the angular momentum of the gas is very large, the centrifugal radius (classically speaking, the radius at which the gas must transfer angular momentum in order to continue its inward spiral) of the accreting gas will be well within the Bondi radius, making this estimate of gas capture rate a reasonable characteristic value for the inflow of gas. It would be prudent to note that for steady-state accretion, as assumed in this paper, the canonical picture of the centrifugal radius may break down. As detailed in [19], transfer of angular momentum leads to the depression and steepening of the angular momentum profile. However, regardless of the dynamical nuances within the accretion flow, this value can still be used to characterize the angular momentum at flow onset, that is, the magnitude of angular momentum in captured gas.

Yet, there are several reasons we should tread lightly when considering the angular momentum of the accretion flow. From a qualitative point of view, the flow does have some apparent flattening [131], which in and of itself is suggestive against using Bondi

[1]Throughout this paper, the b subscript denotes at the Bondi radius.

accretion to explain the flow's emission in its entirety. Indeed, it is quite natural that the accreting gas would have coherent angular momentum, given its apparent origin. Spectral evidence suggests that the matter accreting onto Sgr A* is shocked stellar wind material emanating from a cluster of O and Wolf-Rayet stars [131], a significant fraction of which orbit Sgr A* in a well constructed stellar disk around the BH [8], oriented with an inclination of $127°(\pm 2)$ and a line-of-nodes position angle of $99°(\pm 2$; East from North). There is also very recent evidence from the Event Horizon Telescope supporting the same orientation for the black hole spin axis [17]. However, simulations of the stellar wind dynamics suggest the centrifugal radius occurs well within the Bondi radius [25], indicating we can still trust, at the very least, this gross estimate of the gas capture rate.

Given the extremely low luminosity of the flow, this capture rate points to the intriguing fact that the radiative efficiency must be extremely low, $\ll 0.01$, loosely dubbing the mélange of remedying models radiatively inefficient accretion flows (RIAF). While the detailed properties of these flows may differ significantly, in order to be considered a RIAF flow, the model of BH accretion must merely satisfy the faint requirement. The most common models under this umbrella are characterized by accretion-comparable outflows and/or the advection of energy into the BH (for a recent review, see [140]). By advecting energy into the BH, or driving it away via an outflow, the luminosity of the accretion flow itself is naturally lessened immensely. Further, these models have been shown to explain the basic features of the quiescent emission from Sgr A*, including radiative efficiency, low resolution spectrum [140], and multiwavelength spectral energy distribution [141].

The physical reality of the Galactic Center makes one model in particular quite attractive, the rotating, radiating inflow-outflow solution, or RRIOS [89, 138, 70, 139, 93]. This is primarily for two reasons. First, the apparent origin of the gas is suggestive that angular momentum is important. Second, as found with Faraday Rotation

measurements, the amount of gas that accretes onto the black hole, $\dot{M}_{BH}$, is ≤ 0.01 $\dot{M}_b$ [81]. This is also the conclusion reached by [88], who calculated the total inverse-Compton emission of the inner disk assuming a Bondi accretion profile and found that it significantly overpredicted the observed X-ray emission. [70] demonstrated that for RRIOS-like flows the bulk of the inflowing gas flows out again after reaching roughly the centrifugal radius, resulting in a small rate of net accretion on to the BH. These models can take a range of angular momenta, spanning from pure Bondi accretion to anything that leaves the centrifugal radius reasonably within the Bondi radius, with no direct observational constraint as of yet. The determining of this angular momentum, however, has dire implications for the strength and distribution of any outflowing mechanical feedback [93].

Perhaps the most in-depth X-ray observational study of the quiescent emission from Sgr A* thus far has been done by [131]. This is thanks to a recent wealth of data from the Chandra X-ray Visionaries program, which provides over 3 Megaseconds of Sgr A* observations. In that paper, the authors study the BH from a purely spectral perspective and are able to place some constraint on the X-ray emission. Unfortunately, that work was unable to place any constraints on the angular momentum of the gas. However, they show that the spectrum suggests a fitted radial density profile that is consistent with a strong outflow, nearly balancing the inflow, using an approximate 1-D analytical RIAF model. The authors were even able to place limits on the deconvolution between quiescent point-like and extended emission, showing that unresolved residual point-like emission (with detected flares removed) can only account for ≤ 20 % of the quiescent emission. While we expect undetected flares to contribute relatively little to this point-like quiescent emission from an extrapolation of flare fluences, emission processes very near the event horizon are the most uncertain, and therefore need not be the case.

Thus, in order to understand some of these very local processes near the SMBH, we should keep in mind the flares, since a truly unified model would be able to explain both the flare emission and the quiescent point-like emission. Further, understanding of one may help to illuminate the conditions of the other. In the study discussed above, the authors also show that the cumulative spectrum of the flare emission is observed to be a powerlaw with index ~ 2.6 [131]. While the production mechanism of flare emission is still poorly understood (e.g., [143]), the variability timescale makes it clear that they originate in localized regions very near the SMBH. This creates many challenges from a theoretical standpoint, as the physics near a SMBH are an extreme in the universe, leaving their physical origin up for debate.

However, some compelling work has recently been done by [3] to understand the flare emission. After previous studies have suggested the importance of thermodynamically decoupling electrons from ions at low radii [141], these authors created the first relatively large scale general relativistic magnetohydrodynamic (GRMHD) simulations to include a sub-grid prescription for modelling the non-thermal electrons. Operating under the assumption that the accretion flow is rotationally supported within their simulation boundaries has allowed them to simulate, and generally match, the detected multi-wavelength flaring properties of Sgr A*. They show that the flares can be explained by particle acceleration in highly magnetized regions through magnetic reconnection. Further, they provide the first roughly unified model of an LL-AGN at low radii. Thus, by extension, they also provide a general framework for understanding the quiescent point-like emission. In general, as we move to lower radii, the magnetic field becomes increasingly important. When considering models, we should allow for the two different populations of electrons: a larger thermal population and a much smaller non-thermal population in a highly turbulent environment. Thus, possibly important emission mechanisms include the full spectrum: Bremsstrahlung [131], inverse-Compton [79, 141], and synchrotron emission [79, 141].

Clearly, despite all of the observations, the details of the dynamical dance of the shocked stellar wind gas with the BH is still held under relatively few constraints, leaving alternative models to continue marauding the theoretical landscape (e.g., [144]). This means we need to undertake serious effort to observationally fetter the flow properties. However, genuine observational constraint cannot be obtained in this case without legitimate modelling, both spatial and spectral. Since this means highly nonlinear dynamical modelling, it requires stepping out of the analytical realm and into simulation. This is needed not only to understand the multidimensional flow structure required to self-consistently model the inflow and outflow simultaneously, but also the magnetic field structure, which is likely to be an important factor for understanding the emission that originates very near the BH. Simulations of these kinds of accretion flows have been done in at least some capacity for several years now [142, 89, 70], but taking these simulations and connecting them to observation in a self consistent manner is a challenge and has yet to be done.

By doing just that, albeit with slightly simplified 2-D hydrodynamic simulations, we herein attempt to remedy as many of the uncertainties as reasonably possible and provide a path forward for deepening our understanding of the Galactic Center. We compare images of the combined quiescent *Chandra* data (the same data set as analyzed in [131]) directly to simulations of black hole accretion via the development of a suite of Markov Chain Monte Carlo (MCMC) tools designed for this purpose. By breaking the quiescent emission into several bands, we can use as much information in the data as possible, utilizing both spectral and spatial power simultaneously. This serves to break degeneracy between key interesting flow parameters such as temperature, density, angular momentum, and inclination angle, providing some of the first self-consistent constraints on not only the accretion flow structure, but also the decomposition of spatially extended accretion structure from point-like emission. Such an analysis will provide a more legitimate test of the RRIOS solution, as well

as the broader class of RIAF models, and lend significant guidance to the way that we model the processes surrounding LL-AGN in the center of galaxies.

2.2 Methods

The Chandra X-ray Visionary Project (XVP) to observe the Milky Way's SMBH, Sgr A* from February 6 to October 29, 2012 resulted in approximately 3 Ms of exquisite data, opening up a completely new regime of insight into BH accretion. Chandra and the XVP program have offered us an excellent opportunity to observe directly the dynamics of hot gas around a black hole, and, with proper modelling, hopefully elucidate the inner workings of the enigmatic class of objects known as LL-AGN. Combining this observational data with 2-D RRIOS simulations [93], we attempt to constrain directly the accretion structure via the power of Bayesian MCMC fitting.

2.2.1 Data Preparation

For a more detailed description of the data reduction and quiescent X-ray image generation, we recommend the reader to [131]. However, in short, the data are reduced via standard CIAO processing routines (version 4.5; Calibration Database version 4.5.6). Since the differences between individual obsevation pointings are all within 14", the merged data is treated as a single observation. [131] found no apparent calibration issues. Flares are removed from the quiescent data through detection with the "Bayesian Blocks" routine [92], leading to a total quiescent exposure time of 2.78 Ms. The observed quiescent image over the entire spectral band (1-9 keV) can be seen in Figure 2.1. The southeast corner of the image is excluded in the fit due to significant emission from an unmodelled feature in the region (highlighted by red lines in Figure 1; see also [131]). The region used for fitting extends to a radius of approximately 0.5 r_b. Since the source is on-axis, the FWHM of the instrument

is comparable to the pixel size. To utilize additional spatial information from the dithering of observations, we construct the so-called "super-resolution" image with a pixel size of 0.123" on a side [131]. The full band image is then split into three bands, to place some spectral constraints on the fit and reduce degeneracy. The bands (1-4 keV,4-5.5 keV, and 5.5-9 keV), were chosen such that the counting statistics are roughly similar in each image.

2.2.2 Hydrodynamic Simulations

We solve the same set of hydrodynamic equations in 2-D spherical polar coordinate as in [70] using the new radiation MHD code Athena++ [133]. Athena++ is an extension of the multi-dimensional MHD code Athena with the new capability of curvilinear coordinates and logarithmic grid. This allows us to cover a large dynamic range, as was possible with the older ZEUS code used in [70], but still solve the hydrodynamic equations with the higher order Godunov method. Since we are only simulating in 2-D, explicit kinetic viscosity (fixed to be $10^{-3}\mathrm{c}_{s,\infty}\mathrm{r}_b$, where r_b is the Bondi radius and $\mathrm{c}_{s,\infty}$ is the ambient sound speed as in [70]) is used to mimic the angular momentum transfer caused by magneto-rotational instability. This viscosity corresponds to a dimensionless angular momentum transport efficiency, α, ~ 0.01 near the centrifugal radius. The simulation setup is also similar to [70] with radial range covering 10^{-3} Bondi radii (r_b), approx. 400 Schwarzschild radii, to 10 r_b with 1024 logarithmicly spaced grid cells. In the polar coordinate, ϕ varies from 0.6° to 179.4° to avoid singularity along the pole and it is divided into 256 uniform grid cells. A reflecting boundary condition is used along the poles. This polar grid is the primary difference from the simulations done by [70], where symmetry was also imposed with respect to the equatorial plane.

The temperature, density, and radial velocity of the simulation domain is initialized to the Bondi profile with an ambient temperature set to be 1.16×10^7 K.

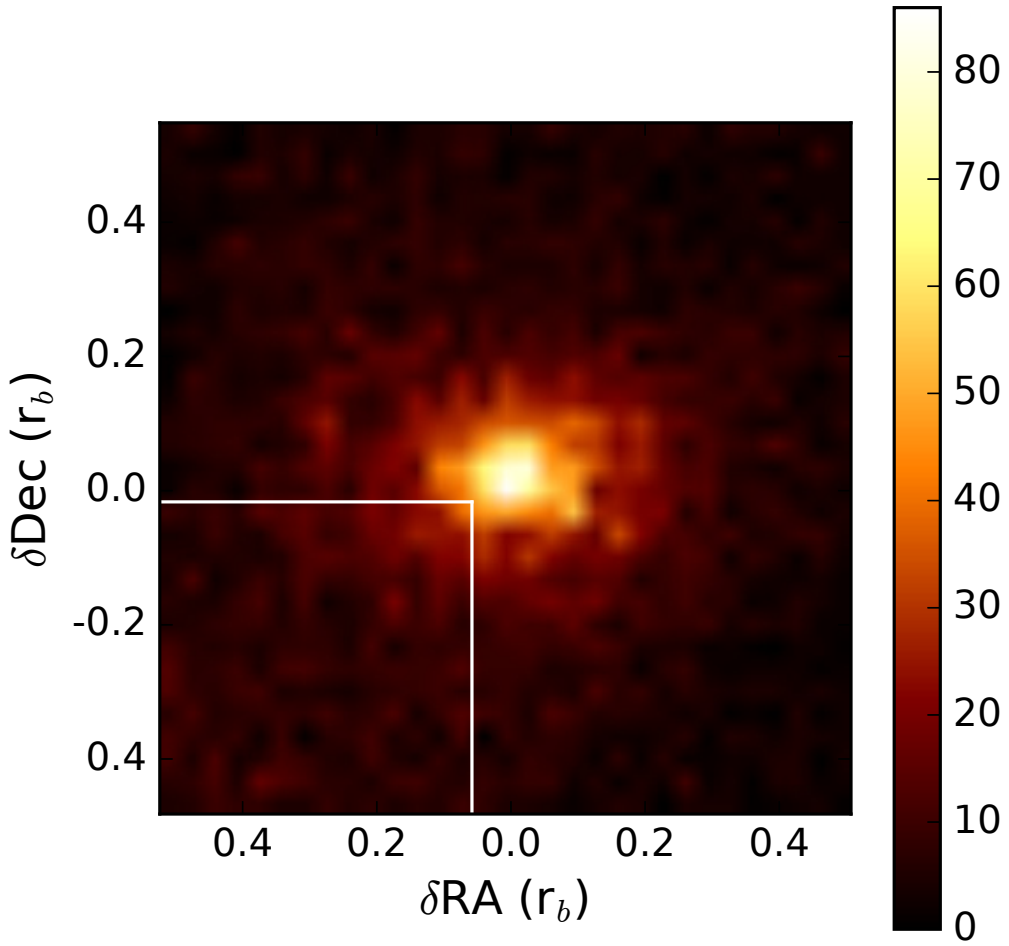

Figure 2.1. Counts image of Sgr A* in the 1.-9. keV band taken with a 2775578 second exposure using Chandra. Colorbar represents total counts in a pixel.

The central black hole mass is assumed to be $4.1 \times 10^6 M_\odot$. These parameters imply $r_b \approx 3.7$", which we will assume to be fixed as in [131]. Bremsstrahlung cooling is included as in [70]. There are two free parameters to consider when setting up the simulation: the density at r_b and the centrifugal radius, r_c. The density at r_b determines the Bondi accretion rate and the cooling time scale compared with the local dynamic time scale while r_c sets the angular momentum of the inflowing gas, as well as the initial angualr momentum of gas in the simulation domain (excluding the poles). Our simulations confirm the basic conclusion of [70]. When the Bondi accretion rate is below ~ 0.01 Eddington accretion rate, we obtain the hot solution with net accretion rate at the center of the simulation domain smaller than 1% of the Bondi accretion rate. We also find significant outflow along the polar direction. However, the main difference between our simulations and results shown in [70] is that we do not find any outflow along the equatorial plane. We confirm that if we impose symmetry along the equatorial plane, the equatorial outflow shows up, which suggests that this is an artifact of the imposed symmetry. In the hot solution regime, properties of the solution, such as total emission, density and temperature profiles, scale with the density at r_b for a fixed r_c, which is proportional to the Bondi accretion rate. When running the simulations, we choose a density scaling at r_b such that Bondi accretion rate is 10^{-3} of the Eddington accretion rate. This ensures that we are in the hot solution domain, which makes the solutions scalable in density due to self-similarity. We have run simulations spanning a range of centrifugal radii to explore how the solution changes with r_c, from 0.01 r_b to 0.2 r_b. It is from these simulations that all models of the accretion flow are derived. A more complete description of the 2-D RRIOS hydrodynamic solutions will be presented in another paper [93].

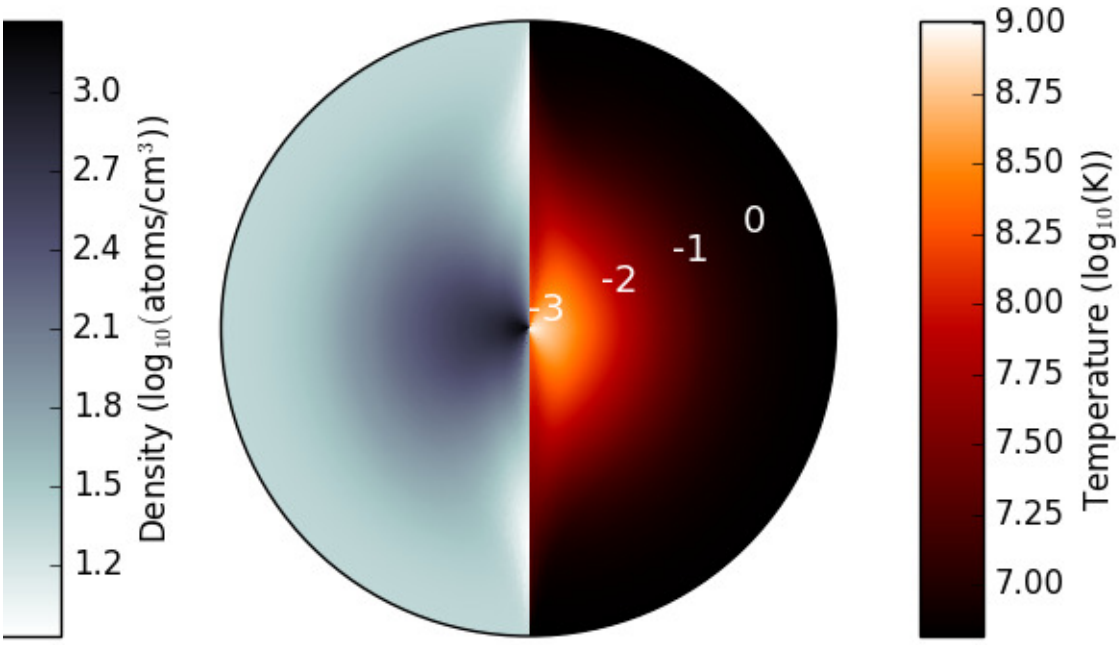

Figure 2.2. Time averaged density (left) and temperature (right) distributions for the best fit solution.

2.2.3 Fitting Procedure

We use the power of Bayesian inference through Markov Chain Monte Carlo sampling to fit the simulated accretion flows detailed above to the Chandra observations. One of the beauties of Bayesian inference is that by introducing the idea of subjective probability, it provides a framework to incorporate prior information. In the case of the physical sciences, this prior information often represents things such as boundary conditions, or past fitting results. Further, by treating parameters themselves as random variables, we directly sample a model's reality given the data, or the posterior, providing us with fully described confidence boundaries for each model parameter. This is an important point, because rather than traditional approaches which can only seek to exclude, we are testing the affirmation of a model and its parameters.

In its most simplistic terms, Bayesian inference can be formalised as:

$$P(\vec{\theta}|\vec{D}) = \frac{P(\vec{D}|\vec{\theta})P(\vec{\theta})}{P(\vec{D})} \propto P(\vec{D}|\vec{\theta})P(\vec{\theta}) \tag{2.1}$$

where $\vec{\theta}$ represents our model parameters, $P(\vec{\theta})$ represents our prior belief in the model components, $P(\vec{D}|\vec{\theta})$ is the probability of the data given the model (or the likelihood function), $P(\vec{D})$ is the probability of the data (also called the evidence), and $P(\vec{\theta}|\vec{D})$ is the probability of the model given the data (the posterior). The evidence term, which requires integrating out the model over all parameter space, places significant constraint on what can be done analytically. Thankfully, it can be neglected when discussing computational approximation, such as that calculated with Markov Chain Monte Carlo techniques.

In this paper we assume all the data is generated from the underlying model with Poisson probability:

$$P(D_k|\vec{\theta}) = \frac{\lambda(\vec{\theta})^{D_k} e^{-\lambda(\vec{\theta})}}{D_k!} \tag{2.2}$$

where k is the kth pixel, D_k is the photon count in pixel k, and λ is the expected number of counts for a given pixel, which is calculated as the exposure multiplied by the flux as determined below. By sampling directly from the posterior we are able to then obtain confidence intervals for our parameters. In this analysis, we use the Metropolis-Hastings algorithm to sample the posterior probability distribution for the parameter set. This is a Markov Chain Monte Carlo method that relies on rejection sampling to obtain a sequence of random samples drawn from the posterior, and can thus be used to approximate the posterior probability distribution.

2.2.4 Modelling

The full list of fitted parameters and their relationship to each other is pictorially described in Figure 2.3 and a summary of all the models to be compared is shown in Table 2.1. The full list of priors used in this paper can be found in Table 2.2.[2] In order to fit the simulated accretion flows to the Chandra data, we generate synthetic images from an interpolation of the hydrodynamic simulations and employ a heirarchical Bayesian fit, with three levels of parameters. Assuming a metallicity as that of the local Sgr A* complex, $\mu \sim 0.76$, we only require three parameters to fully characterize the accretion flow's emission since they are approximately self similar: temperature scaling - T_b, density scaling - n_b, and centrifugal radius - r_c/r_b[3]. In this context, r_c represents the magnitude of the gas angular momentum at capture. The spatial density and temperature distribution of the accretion flow is generated by interpolating time averaged hydrodynamic simulation data (see Figure 2.2) at different r_c/r_b, in this case, through 0.04, 0.08, and 0.2, allowing us to sample a continuous

[2]In the following notation, i and j represent the pixel coordinates and k represents the kth band image.

[3]For these simulations, parameterizing values in terms of the Bondi radius is simply used for convenience.

distribution in r_c.[4] It should be noted that while this is the case for almost all accretion flow models in this paper, we will have a separate model (model *pBondi*, for pseudo-Bondi) where the angular momentum is fixed to the lowest of our simulations in order to directly test the realism of the Bondi solution for Sgr A*. Then, to build a 3-D model of the flow, we need only introduce its positioning and orientation information. This includes the Right Ascension (R.A.), Declination (Dec.), inclination angle (θ_I), and position angle (θ_P, East from North).

Once we have a 3-D model, we need to calculate its emission in order to compare to an observed image. Volume normalized emission measure as a function of temperature is calculated within *xspec* using the model $tbabs * vapec * dustscat$, as used in the spectral fit to the integrated quiescent emission [131]. Both absorption and dust scattering effects are taken into account. In all of the modelling, we assume the absorption column, as estimated from the powerlaw model fitting to the accumulated flare spectrum, is 13.76×10^{22} cm^{-2} [131]. After mapping the *xspec* calculations to the simulation temperature table, and scaling it with the density table, we have the volume-normalized counts for each radius and ϕ. Finally, to generating a synthetic image of the accretion flow we integrate along the line of sight at the center of each pixel out to r_b, unless the pixel contains the origin. If the pixel contains the origin, we integrate from the inner boundary of the simulation out to r_b.

While the accretion flow accounts for the bulk of the emission in the Chandra images, we still need to account for other sources as best we can. This includes both a spatially smooth background component(BKG$_k$) and a point-like component centered on the BH (P.S.$_k$). This background accounts for all foreground and background contributions (e.g., including faint stellar and extragalactic sources, as well as diffuse hot gas), which are assumed to be smoothly distributed on scales of a few arcseconds.

[4]We have also fit the images interpolating through $r_c/r_b = 0.02$, 0.04, and 0.08 with no change in results.

Since this smooth background contributes relatively little to the overall flux in the images, a spectral decomposition and modelling of these two is beyond the scope of this paper. Therefore, each kth band background component is allowed to roam free with respect to the others. A characterization of the quiescent P.S.$_k$, however, is of great interest. Recall, this includes anything within the inner boundary of our simulation, $\sim 400\mathrm{r}_s$. Thus, a model test, comparing several parameterizations of this enigmatic component is required. In general, with the exception of the *pBondi* model, different model names refer to a different parameterization of this point-like component.

Since the X-ray emission most proximal the BH remains very uncertain, there are many ways in which we could consider parameterizing the point source contribution. To get a baseline of what might be the best possible fit, particularly for other parameters, model *free* places no constraint on the relationship between individual P.S.$_k$ components, allowing them to roam free, similar to BKG$_k$. However, we would like to physically model this point-like emission. To first order, we might expect this contribution to just be dominated by one component, e.g. unresolved flare emission, inverse Compton emission, or thermal Bremsstrahlung. Thus we could consider it to be well fit by a single powerlaw component (models *plaw* and *plaw-wp*). In this case, we have only two free parameters to characterize the P.S. emission: the photon index, α and a normalization, K. No prior constraint is placed on this powerlaw index.

Alternatively, we may consider a scenario where we have multiple competing emission components. In this case, we assume the flare emission in X-ray has an approximately fixed mean spectral shape, as obtained in [131]. Thus, the flare emission has a strong prior on the power law index, α equal to 2.6 ± 0.4 (90% confidence - [131]). We assume that any additional point source emission that cannot be attributed to the simulation can be approximately parameterized as a powerlaw. This potentially unknown powerlaw component is left with no prior constraint as to the index. In

Table 2.1. Summary of the models to be compared. Here *pBondi* stands for "pseudo-Bondi," *plaw* for a powerlaw P.S.$_k$ parameterization, and *wp* for "with prior," referring to the prior on the flow orientation.

Model Name	P.S.	Additional Comments
free	independent	
plaw	Single powerlaw	
plaw-wp	Single powerlaw	Prior on flow orientation set by stellar disk
dplaw	Double powerlaw	Prior on one powerlaw slope set by the flare emission slope
pBondi-wp	Single powerlaw	r_c is fixed at the lowest of our sims (0.02 r_b); Prior on flow orientation set by stellar disk

this scenario, these two powerlaw components then combine to form the point source normalization in each band, P.S.$_k$ (model *dplaw*).

The normalized powerlaw emission for a given powerlaw index, α, is calculated within *xspec* using the model $tbabs * pow * dustscat$. Again, both absorption and dust scattering effects are taken into account. Assuming no interloping point sources, P.S.$_k$ and BKG$_k$ combine with the projected, integrated accretion flow emission to create the total pixel counts, $C_{i,j,k}$. The final step in creating a synthetic image that can be compared to the observed image is to convolve $C_{i,j,k}$ with the Chandra ACIS PSF, which is assumed to be described by a Gaussian of FWHM=0.5". [5]

2.2.5 Numerical Caveats

The APEC implementation within *xspec* restricts the temperature of the plasma to $\leq$ 68 keV. Since the temperatures in the simulation tables span a large range,

[5]Since the effective frequencies of the bands are quite similar due to the spectral shape, this should be a sufficient approximation. Indeed, MARK simulations show only a few percent difference between the energy enclosed in the inner arcsec between the low and high band. See Figure 4.6 http://cxc.harvard.edu/proposer/POG/html/chap4.html. This does, however, neglect the Lorentz contribution to the PSF, which causes a significant spread for approximately 15% of collected photons at this energy. Thus, we do not expect it differentially affect the different bands appreciably, however, we may overestimate the background emission.

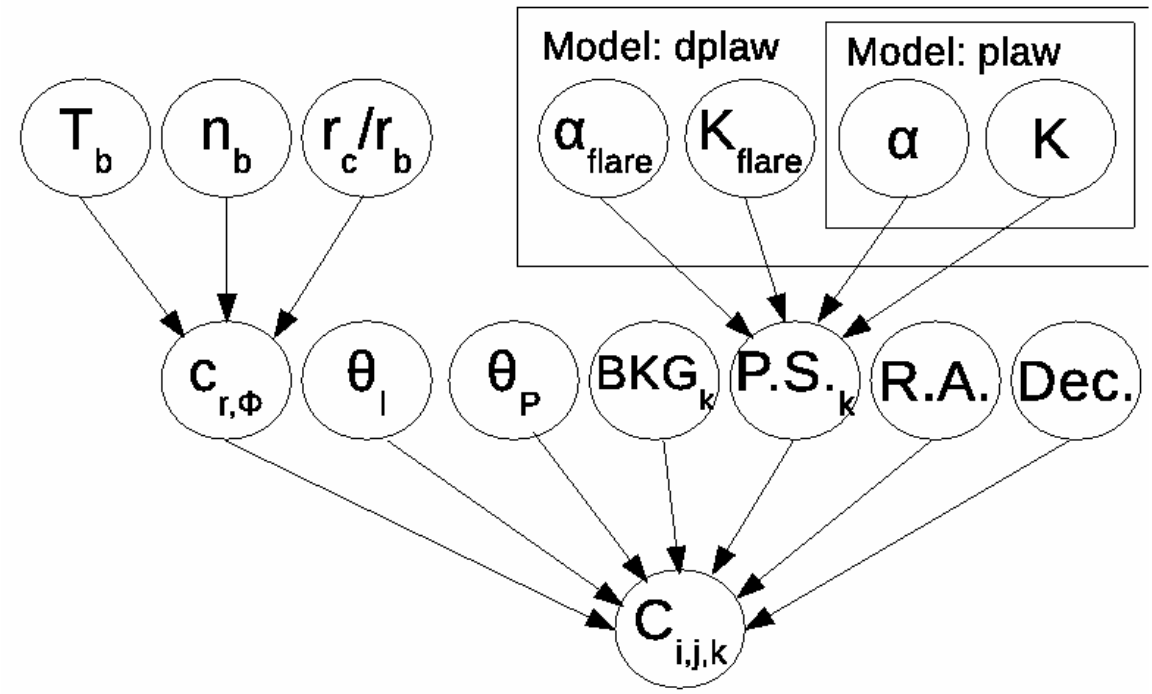

Figure 2.3. The Heirarchical Bayesian Network. Bondi temperature and density combine with the centrifugal radius to form a volume normalized count rate for each grid cell, $c_{r,\phi}$. Flare power law index and normalization combined with an unknown powerlaw index and normalization to form a point source emission in each band. These hyperparameters combine with the background (BKG_k) in each band, the positioning on the detector (R.A. and Dec.), the inclination angle (θ_I), and the projection angle (θ_P) to form total counts in each pixel, $C_{i,j}$.

Table 2.2. Summary of the priors. A uniform distribution is represented as U(lower,upper) and a normal distribution is represented as N(mean,sigma).

Parameter	Model	Prior
T_b	All	U(0,inf)
n_b	All	U(0,inf)
r_c/r_b	pBondi-*	0.02 fixed
	All others	U[0.04,0.2]
θ_I	*-wp	N(127,2)
	All others	U[90,180]
θ_P	*-wp	N(99,2)
	All others	U[0,180]
BKG_k	All	U[0,inf)
$P.S._k$	free	U[0,inf)
α	*plaw*, dplaw	U[1,10]
K	*plaw*, dplaw	U[0,inf)
α_{flare}	dplaw	N(2.6,0.12)
K_{flare}	dplaw	U[0,inf)

reaching temperatures significantly higher than this, we need to estimate beyond the allowed *xspec* temperature. As the emission from such a plasma is dominated by free-free emission, we can estimate its emissivity using the following equation:

$$\epsilon_{\nu}^{ff} \propto T^{-1/2} \exp\left(-\frac{h\nu}{kT}\right) \tag{2.3}$$

Further, since the spectral shape is approximately constant with increasing temperature in the energy range covered by *Chandra*, we can straightforwardly extrapolate the emission at temperatures 68 keV from the absorbed, volume-normalized emission at 68 keV. Lastly, it should be noted that any error introduced in this term will be absorbed into the central point source contribution, as these temperatures only occur very close to the black hole. However, the density does not increase quickly enough with decreasing radius and the volume occupied by this high temperature gas is relatively miniscule, making its overall contribution to the flux in the image quite small, $< 1\%$.

2.3 Results

First, we will determine the best model to scrutinize, as well as assess the goodness of fit. Ideally, this would be done by a full Bayes factor calculation, which is the ratio of the posterior odds of one model to another (or rather, which model better explains the data, D):

$$BF = \frac{P(M_1|\vec{D})}{P(M_2|\vec{D})} \tag{2.4}$$

This is the odds of one model versus the other given the data. If we don't consider any prior model favoritism, BF reduces to the ratio of model likelihood. Unfortunately, this ratio is actually quite difficult to calculate, as it requires integrating over all of parameter space for each model. Thus, since our model parameters are well behaved

Table 2.3. Numerical interpretation of ΔBIC.

ΔBIC	Strength of Evidence Against
0 to 2	Barely mentionable
2 to 6	Positive
6 to 10	Strong
>10	Very Strong

(more or less normally distributed), we will take advantage of an approximation, the Bayesian Information Criterion, between models:

$$\Delta BIC = -2\log\left[\frac{max_{M_1}P(\vec{D}|\vec{\theta}_1)}{max_{M_2}P(\vec{D}|\vec{\theta}_2)}\right] - (p_2 - p_1)\log(S) \tag{2.5}$$

where $\vec{\theta}$ is the maximum likelihood parameter vector for the respective model, p is the number of parameters for the model, and S is the number of data points. This statistic is shown to approach the Bayes Factor for large sample size [114], before including model priors. A guide to numerical interpretation of this statistic is shown in Table 2.3 [56].

A comparison of models through ΔBIC is shown in Table 2.4. We see that the *plaw* model optimizes the amount of information gained. Unfortunately, for this model the inclination angle is not strongly constrained, as long as the flow is at least moderately edge-on. Although the goodness of fit is slightly worse when we add a prior on the flow's inclination and projection angle ($plaw - wp$), the ΔBIC is so small (~ 1.7) as to not even be mentionable. Therefore, since we cannot realistically discriminate between these two models, and we heavily favor the $plaw - wp$ model *a priori*, due to our favorability of the stellar wind gas origin, we will consider this model the best model. This allows us to somewhat more tightly constrain other parameters. Other models, including the *dplaw* and *pBondi* are heavily disfavored. The *dplaw* model is disfavored because adding extra degrees of freedom doesn't result in an appreciably better fit, suggesting the point source can be reasonably characterized by a single powerlaw within the limits of the data, and the *pBondi* model because

Table 2.4. ΔBIC between models, relative to the best fit model.

Base Model	With Prior	Without Prior
free	6.4	4.7
pBondi	46.4	N/A
plaw	1.7	0.0
dplaw	N/A	12

fixing the angular momentum to our lowest allowed value leads to a much poorer fit in general. We discuss the causes and implications of the poor fit of the *pBondi* model in Section 2.4.2.

The results of the fitting process for our best fit model, $plaw - wp$, are listed in Table 2.5 along with the 90% confidence bounds. The flow enters the Bondi radius at a temperature ($\sim$ 1.3e7 K) and density ($\sim$ 100 cm^{-3}), great enough to be detectable in the X-ray band with such a long exposure provided by the XVP program with Chandra. The gas also has considerable angular momentum, leaving $r_s \ll r_c \sim 0.056 r_b \approx 8 \times 10^{-3}$ pc. This density and angular momentum implies a mass inflow rate at r$_b$, $\dot{M}_{in,b}$ of 2.4×10^{-3} $\dot{M}_{Ed}$ and a mass accretion rate, $\dot{M}_{acc}$, of $\leq 10^{-2} \dot{M}_{in,b}$ There is a non-negligible, steep residual point-like component to the emission. This point-like component has a specific luminosity of $\log_{10}(\nu \mathrm{L}_\nu) \sim 31.96$ ergs/s at 5 keV, and is responsible for 4.2 (2.3,7.0)% of the observed emission within 1.5" in the 1-9 keV band with Chandra.

Looking at the full distribution of each parameter and the parameter-parameter confidence bounds (Appendix C), suggests very little degeneracy, except for those which are quite natural; for example, the anti-correlation between temperature and density. This anti-correlation is very much expected, due to their emissivity proportionality, $\propto$ n^2 T$^{1/2}$ in the relevant temperature range. Further, the two parameters are well constrained for the first time in a self-consistent fashion, with fairly narrow uncertainty ranges. With the exception of the powerlaw index and normalization, all of the parameter PDFs are more or less normally distributed. This suggests the

Table 2.5. Best fit and 90% confidence intervals of free parameters marginalized over all others for the model *plaw-wp*. Model implied quantities are distinguished by the gray rows.

θ_I (deg.)	126.4 (122.6,130.4)
θ_P (deg.)	99.1 (96.3,101.8)
r_c/r_b	0.056 (0.048,0.066)
T_b (K)	1.28e7 (1.19e7,1.42e7)
n_b (cm^{-3})	101.6 (91.4,111.1)
BKG1 (counts/pix)	0.21 (0.01,0.45)
BKG2 (counts/pix)	0.41 (0.17,0.65)
BKG3 (counts/pix)	0.48 (0.30,0.69)
α	4.8 (3.5,7.5)
$\log_{10}$(K) (ergs/s at 5 keV)	31.96 (31.32,32.18)
$\Rightarrow \dot{M}_{in,b}/\dot{M}_{Ed}$	$\sim 2.4 \times 10^{-3}$
$\Rightarrow \dot{M}_{acc}/\dot{M}_b$	$\leq 10^{-2}$

information provided by the observations herein is sufficient to fully characterize the quiescent accretion flow.

The theoretical images generated from these best fit values are shown in Figure 2.5 and compared to observed images. As previously noted, but never quantified, the emission is considerably flattened. We plot the eccentricity in each observation band as a function of major axis radius in Figure 2.4. At low radii, where the emission is dominated by the point-like emission, the eccentricity is very low. The eccentricity increases steeply up to ~ 0.56, 0.53, and 0.49 at 0.2 r_b for the 1-4 keV, 4-5.5 keV, and 5.5-9 keV band, respectively, where the emission is predominantly from the extended accretion flow. As we then move to larger radii, the eccentricity begins to decrease as the background emission becomes increasing important.

We see that there are no apparent residual effects, particularly at lower radii. However, there can be contributions from unmodelled structure at large radii (≥ 1"). For example, the spur of emission to the northeast of Sgr A*. This is echoed in the goodness of fit estimate (Appendix A). In the inner arcsecond, where the predominant source of error results from time averaging the simulations and not modelling the turbulent structure, the statistical consistency is at a level of 2.6%. When including

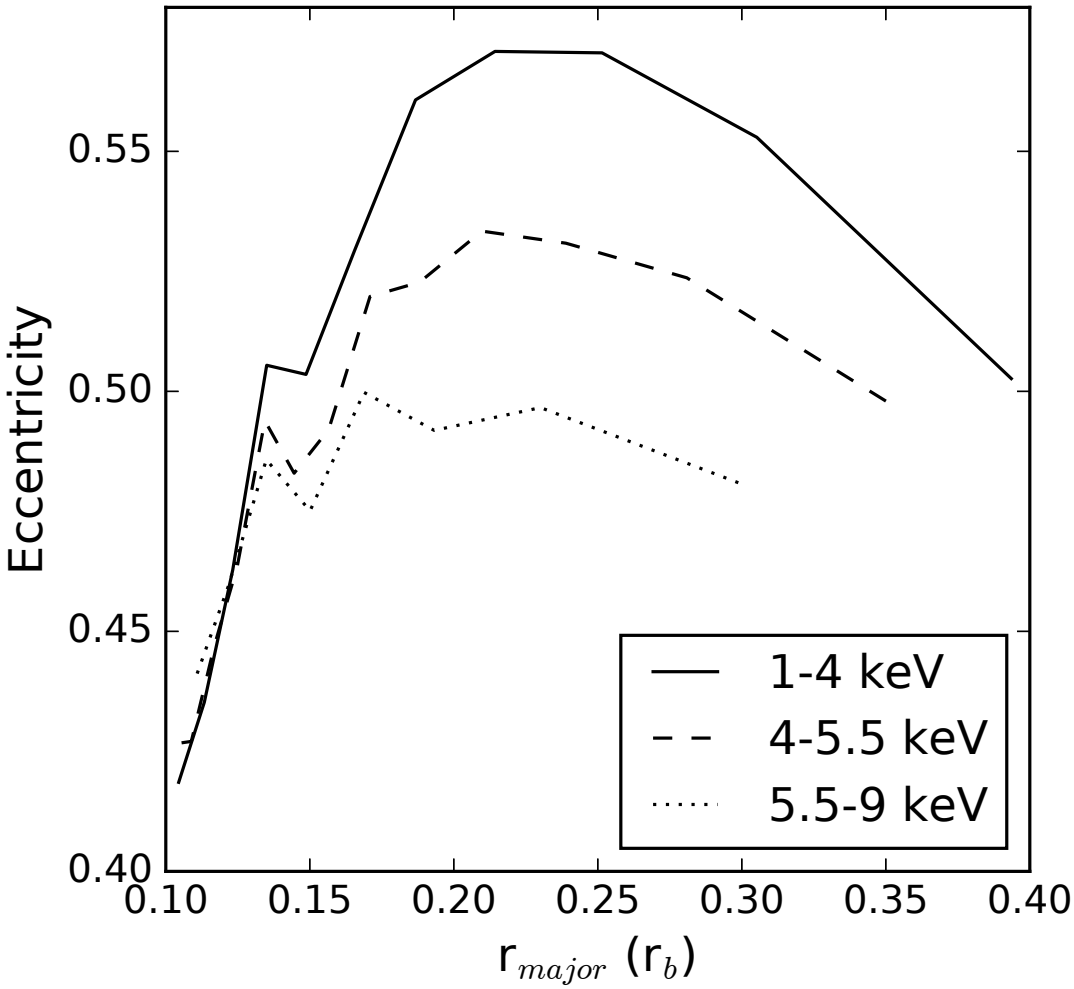

Figure 2.4. Emission eccentricity as a function of major axis radius. These profiles correspond to the top panel of images in Figure 2.5, the theoretical emission smoothed by the Chandra PSF.

radii out to $\sim$ 2.8", where there are many more error terms to consider, such as unmodelled extended structure and discrete X-ray sources, the statistical consistency drops. However, we have found the fitted parameters insensitive to the radius of the fitted region within the observational images shown in Figure 2.5. Thus, all uncertainties considered, we consider this fit to be not only reasonable, but quite good.

2.4 Comparison with Previous Works and Implications

Now, we need to discuss these numerical results in the context of previous modelling and observational efforts. While prior observations have not lent us a great deal of constraint, they have provided some important information for modelling of the quiescent accretion flow. This includes constraints on the mass inflow at different radii, the radiative efficiency of the accretion flow, and some 1-d considerations about the structure of that accretion flow. From a theoretical perspective, simulations have separately made significant strides in attempting to model the physics very near the SMBH, as well from its apparent origin in stellar winds. With our results here, we are able to significantly build upon these past observational constraints and help to lend guidance to future modelling efforts.

2.4.1 Temperature/Density and the Gas Origin

At flow onset, i.e., r_b, the best fit temperature and density are consistent with previous estimates based on spectral analysis of the *projected* X-ray emission as observed by Chandra [2]. They are also consistent with the simulation results of [25]. These authors attempt to model the flow onset by simulating the stellar wind dynamics of the surrounding stellar cluster. By estimating stellar mass loss, they show that the density at r_b is $\sim$100 cm^{-3}. Similarly, their predicted temperature is $\sim 1\times 10^7$ K at r_b. This can easily be understood in the context of shocked stellar winds. Our best

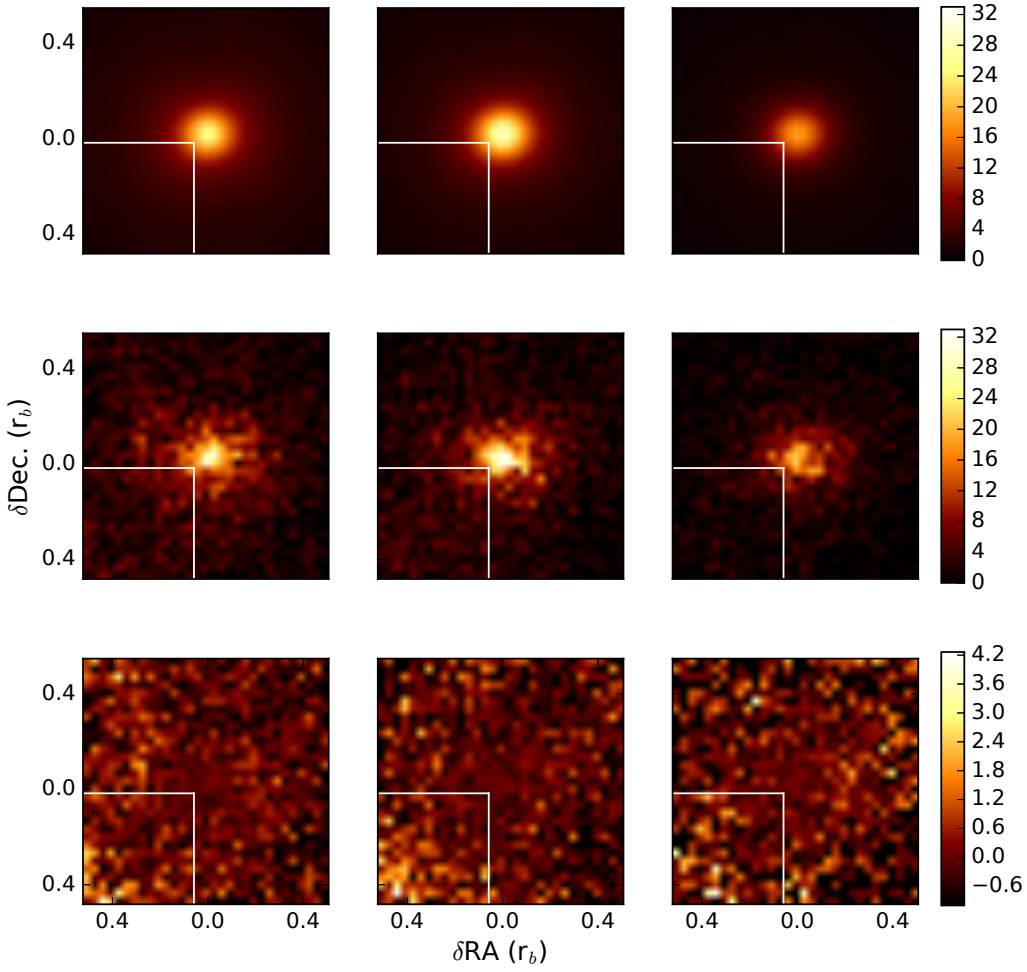

Figure 2.5. From top to bottom: the theoretical image, observed image, and residual image ((observed-theoretical)/theoretical). These are shown for all three bands, which are from left to right: 1-4 keV, 4-5.5 keV, and 5.5-9 keV.

fit temperature implies a shock velocity of ∼1000 km/s, which is reasonably characteristic of stellar winds. For example, the wind velocities range from approximately 600 km/s to 2500 km/s in the simulations of [25]. Thus, our result is consistent with an origin of the mass flow in shocked stellar winds.

The temperature and density radial profiles of the accretion flow inferred from our best-fit simulation are also consistent with previous X-ray spectroscopic estimates. [131] approximated the profiles in a RIAF model as powerlaws ($n \propto r^{-3/2+s}$ and T$\propto r^{-\theta}$). Their spectral analysis gives the best-fit $\gamma = 2s/\theta = 1.9(1.4, 2.4)$. If $\theta = 1$, via the virial theorem, then $s \sim 1$, indicating a very flat density profile of the flow, or an outflow mass-loss rate that nearly balances the inflow [131]. They assumed this parameterization characterizes the flow over a wide range of radii, between r_{in} and r_{out} of $\sim 10^2$ r_s and $\sim 10^5$ $r_s \approx 0.25 r_b$, respectively. Even though the simulated profiles we used are not strictly powerlaws (e.g., Figure 2.6), they are roughly in agreement with their conclusion. We find that the density profile is ever so slightly steeper ($s \sim 0.93$), and temperature profile is mildly flatter ($\theta \sim 0.77$). Together, these are consistent with the relation above, within uncertainty.

2.4.2 The Need for Angular Momentum and r_c

Since spherical Bondi accretion is still occasionally invoked when trying to understand the accretion flow onto Sgr A* (e.g., [108]), or LL-AGN in general, we need to test and understand exactly why this is a poor assumption. Compared to our best fit, a lower angular momentum accretion flow leads to a steeper density profile. This can easily be seen in Figure 2.6, which shows the azimuthally averaged density profile for two different angular momentum solutions, and is in agreement with previous results [20]. There are two primary forces that support gravity in an accretion flow, the gas pressure gradient and the centrifugal force. As the centrifugal force decreases, this necessitates a larger gas pressure gradient, and thus a steeper density profile.

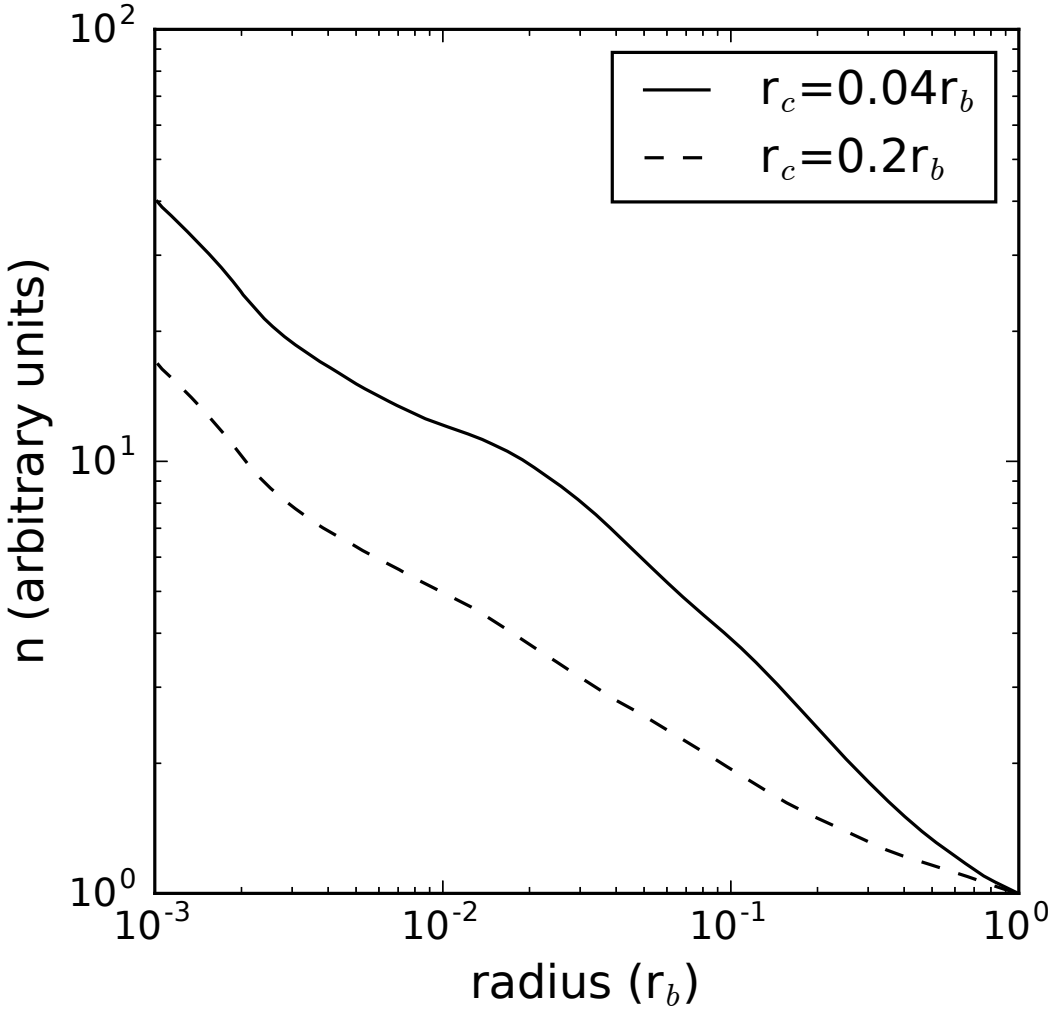

Figure 2.6. Azimuthally averaged density profile for two different simulations, normalized to 1 at the simulation outer boundary. A lower angular momentum leads to a steeper density profile.

This density profile change manifests itself in the best fit solution to other parameters. In order to compensate, the *pBondi* model has a decreased Bondi capture density of $\sim$40 cm^{-3}, approximately a factor of two below the best fit model. The density change largely comes from the central pixels in the medium and high energy bands. For fixed Bondi density, the steep rise of density with radius leads to too much emission very near the BH. In an attempt to offset the decrease in density, the temperature is increased slightly to $1.6\times$ 10^7 K to help model the flux at larger radii. This in turn makes the emission of the accretion flow harder, which pushes the PS powerlaw to a spectral index of $\sim$9($\pm$0.5). However, these changes fail to fully compensate for the low angular momentum; the rapid increase in density of this simulation can not realistically model the emission at both small and large radii simultaneously. This is most prominently seen in Figure 2.7, which shows the mean residual as a function of radius, comparing the *pBondi* model and the *plaw* model. We can see that there is strong residual structure at intermediate to large radii. Further, these best fit temperature and density values are near, if not beyond in the case of temperature, the limits of what is possible given the previous simulations of [25]. As the angular momentum decreases further, it is likely that these values would become irreconcilable with other results.

At a best fit r_c=0.056 r_b, the centrifugal radius sits at $\approx$ 20000 r_s. This value has hitherto only been estimated once theoretically, but never observationally. Simulating the onset of the accretion flow by modelling the stellar wind dynamics around Sgr A*, [24] predicted r_c=5000r_s. This seeming discrepancy is likely a numerical result, for multiple reasons, all stemming from the fact that they made this estimate using the very inner region of the flow. First, their simulations were evolved with the SPH code, Gadget-2, which has known issues modelling angular momentum in the depths of a potential well [61]. Further, by the author's own admission, they suspect the number of SPH particles could be too small to realistically estimate the angular momentum

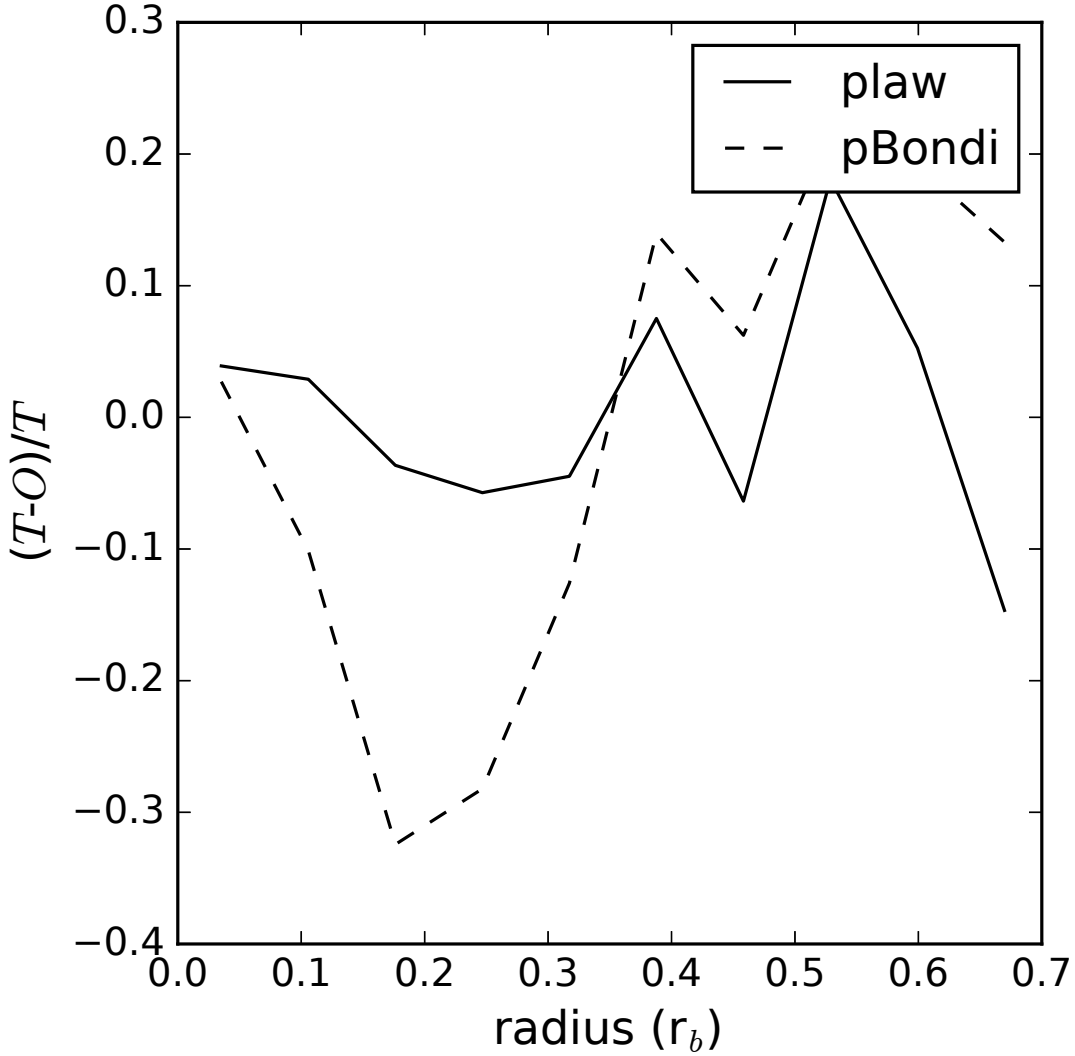

Figure 2.7. Mean residual ((observed-theoretical)/theoretical) plotted as a function of radius for two models in the 1-4 keV energy band. The *pBondi* model has difficulty modelling the emission at intermediate and large radii simultaneously.

in the inner region of the flow that was used to do so. Lastly, as we know from [19], for a steady accretion scenario the centrifugal radius does not exist in any material sense, but merely represents a characteristic radius for the magnitude of the gas angular momentum at the *outer* boundary. In reality, the angular momentum profile depresses and steepens relative to the classical picture due to the transfer of angular momentum. As such, any estimate of r_c made with the inner flow will naturally underestimate r_c. This can be seen in [24], where they show that after initializing the simulation, their average angular momentum of the inner region spikes to a level that is loosely consistent with our determination of r_c, but then dwindles to one fourth of that value as simulation time progresses. We will also point out that the density profile of a flow with such a low angular momentum is unable to model the spatial distribution of emission. The centrifugal radius of the *pBondi* model is slightly larger than the result predicted by [24], and as we show above, even a flow with this value is well outside the bounds of reality.

Since the multi-dimensional structure of the flow is largely encapsulated by the determination of the gas angular momentum, as parameterized by r_c, the results detailed here are of prime importance. Being the first observational constraint on r_c, our result is an important one for simulations that wish to study the outflow but cannot realize the flow from its origins. Unfortunately, there is not yet a 3-D simulation large enough to model the flow through such a dynamical range, simultaneously self-consistently producing the flow and generating the outflow. Simulations that do realize the flow from its origins will be important for verifying our results, especially as they continue to become more realistic.

2.4.3 The Central Point Source

There have been many works that attempt to constrain the unresolved point-like residuals. Studying the surface brightness profile, [116] estimate that the a point-like

contribution of $\sim 10\%$. An extrapolation of flare fluences below the detection limit ([92]) and a statistical analysis of the X-ray flux distribution ([91]) also find a similar residual point-like contribution. [131] do two separate analyses trying to place constraints on the unresolved point source emission. By comparing the radial intensity profiles of a flare image with the quiescent image they place a limit on the PS emission to <20% of the total X-ray flux within $\leq$1.5" [131]. In a separate analysis, they spectrally decompose the point-like emission from the extended emission. That spectral decomposition suggests the unresolved point source emission, assumed to be due to Bremsstrahlung, contributes 16(5,23)% to the total flux. Our best fit model, placing the fraction of unresolved point-like emission in this region at 4.2(2.3,7.0)%, is well below the upper limit constraint from spatial decomposition and loosely consistent with the other results.

While the total flux is roughly in agreement, the spectral shape is quite the contrast. When assuming this unresolved emission is a powerlaw, we find that it is characterized by a spectral index, $\alpha = 4.8(3.5, 7.5)$, grossly steeper than the assumed Bremsstrahlung spectrum in the spectral decomposition of [131]. Thus, we are able to rule out Bremsstrahlung as an important emission mechanism in the inner 100 r_s. Recall, we noted that <1% of the emission in the images originated between radii of 100-1000 r_s since the density does not rise quickly enough to compensate for the low volume and rising temperature, further suggesting that Bremsstrahlung should not be important for the emission so near the SMBH.

The discrepancy between our findings and those of [131] can be understood quite naturally when looking across all of the differences. Not only is their PS spectrum significantly harder than the PS deconvolution in our analysis, but it is also a much more significant contributor to their flux. This results in the PS emission pushing their flow emission to a softer spectrum. It does so by flattening the density profile and steepening the temperature profile, both of which put more emission in a cooler

flow component than the analysis presented here. This discrepancy illustrates the problem with modelling spectrally alone, which entangles emission components with too many degrees of freedom, where we have to make too many assumptions to make progress. To break the degeneracy, we need to have some constraint on at least one component solely, point-like or extended flow, as is done here with the outskirts of the flow.

Another possibility is that the point-like emission is unresolved flare emission. Yet, here too, lies a discrepancy. The cumulative flare spectrum exhibits a spectral index of $\alpha = 2.6 \pm 0.2$, as seen in [131]. They also show that there is no evidence of a significantly changing spectral index with flare strength. Therefore, unless the properties of unresolved flares are substantially different from resolved ones, this spectral index is well beyond the bounds of certainty placed by our analysis here. We deem this unlikely, due to the apparent universal nature of X-ray flare emission around a black hole, not just for Sgr A*, but for the general population of LL-AGN [72].

In reality, there are likely two primary contributors to the quiescent X-ray point-like emission, synchrotron and inverse-Compton scattering, which can be understood in the context of both [3] and [141]. These theoretical works set the stage for completing the picture of quiescent emission near Sgr A*. By decoupling electrons and allowing them to become non-thermal, [3] show that the flares could naturally be due to trapped particles in magnetic flux tubes, which are accelerated through reconnection. But we can also see from that work that these particles are only a small fraction of the overall electron population. The rest of the electrons exist in a very hot, either thermal or quasi-thermal, turbulent evironment.

This intepretation is qualitatively in agreement with the calculations of [141]. They show that the multi-wavelength quiescent spectral energy distribution can be explained by electrons in a quasi-thermal distribution. The bulk of the electrons are

thermal, emitting strong synchrotron emission in the radio bands. Some of this thermal synchrotron emission is inverse-Compton upscattered into the UV, with a high energy exponential tail extending into the X-rays. Also, in their model, approximately $\leq 1.5\%$ of the electrons must be accelerated into a synchrotron powerlaw tail in order to match the quiescent IR emission. These electrons, which exist outside of the strong magnetic flux tubes associated with the flares, are in an approximate steady state, with synchrotron cooling times typically greater than the advection timescale. Further, [141] show that the powerlaw index of the synchrotron emission must be greater than or equal to 3.5. This scenario is consistent with the multiwavelength spectral energy distribution spanning from radio through IR and to X-ray, including more recent estimates of the mean IR flux [112].

The powerlaw slope found in our work, at 4.8 (3.5,7.5), is in agreement with this predicted upper limit of 3.5 from [141], if only slightly more steepened. Since we would expect the very steep thermal inverse-Compton emission to be detected predominantly in our 1-4 keV band, it is reasonable that our powerlaw would be steepened slightly. However, since the residuals in Figure 2.5 do not show any drastic residuals at the origin that would result from a significant deviation of the point-like emission from a powerlaw, we believe it is reasonable to conclude the emission is primarily due to synchrotron and the inverse-Compton upscattering of this non-thermal emission, with slight contamination from thermal inverse-Compton emission in the 1-4 keV band.

However, their predicted flux is in direct conflict with the results detailed herein. Based on their calculations, we expect the thermal inverse-Compton emission to contribute anywhere from a few tenths of a percent to a percent of the X-ray emission, and, is naturally quite steep due to its thermal origin. A powerlaw index of 3.5 places the synchrotron contribution to X-ray emission at roughly a few percent. Some of this non-thermal synchrotron emission is also inverse-Compton scattered to X-ray

energies, contributing $\sim 10\%$ to the quiescent emission with approximately the same slope as the synchrotron emission. Thus, we expect the total combined synchrotron and inverse-Compton emission to contribute approximately 10-20 percent to the quiescent Sgr A* emission from the model of [141], approximately four times greater than what we observe.

But, there are several model differences that we believe would serve to negate this issue. Most notably is the density profile, $\rho \propto r^{-3/2+s}$, assumed in [141] for their 1-D analytical RIAF solution is much steeper, $s \sim 0.27$, than we find in X-ray studies, $s \sim 1$, from this work and that of [131]. The change in density slope requires the population of ultra-relativistic particles to lessen significantly, decreasing both the synchrotron emission and the inverse-Compton flux. However, making this change in their model creates some other outstanding issues. Specifically, it would lead to an underprediction of the observed sub-mm emission. Yet, these issues we believe to be amenable, given a treatment of the multidimensional structure of the accretion flow. For one, we know from [3] that the magnetic field strength is much greater in the polar outflow region than assumed to be throughout the flow in [141]. Secondly, the assumption of a Maxwellian distribution of electrons at each radius likely leads to further mistreatment of the outflow region. We will explore the full implications of these model differences via an update to the SED model of [141] in Appendix B, as well as explore the physical nature of the steep synchrotron.

2.5 Model Predictions and Future Work

Understanding the low radiative efficiency of Sgr A* is of central importance to learning about the processes surrounding LL-AGN and how their feedback affects the circumnuclear environment. In recent years, the general picture of how the accretion flow evolves has begun to emerge. As gas spews forth from Sgr A*'s large, circumnavigating O and Wolf-Rayet stars in the form of stellar winds, it collides with other

stellar winds, shocking to temperatures that greatly ionize the gas, causing it to emit in X-rays. Without the angular momentum to resist the graviational lure of Sgr A*, it is captured by the BH, and begins falling deeper into the potential well. Whether that gas circularized or not was unclear. However, we show that it indeed does have (and requires) coherent angular momentum, circularizing well within the capture radius, but still quite distant from the BH. As angular momentum is transported, the gas turbulently dances closer to the BH. Some of this gas will accrete onto the BH. Yet, most of it will be driven away in a large collimated polar outflow, to what distance is unclear. With a general framework now in place, we can begin to look in more depth at the implications of this observationally constrained accretion flow and how we may further test the model.

2.5.1 Flow Dynamics

The azimuthally averaged gross mass inflow rate is shown in blue in Figure 2.8. The curve is nicely consistent with other estimates of the mass accretion at different radii, both theoretical and observational. The simulated estimate by [24] lies very near our curve, shown by the red circle. This curve is also roughly consistent with the results of [2], which is shown by the red dotted line. In that work, the authors assume accretion is Bondi-like, and estimate the rate based on the cumulative spectrum within 1.5". Compared to the RRIOS model, which has a relatively flat density profile and corresponding steep mass inflow profile, their Bondi assumption places much more gas at low radii and naturally must underestimate the accretion rate at r_b in order to compensate.

Another important constraint on the accretion flow is that placed on low radii by [81] based on radio data. They place an upper limit of $\sim 2 \times 10^{-7}$ $M_\odot$/yr at 100 r_s based on estimates from radio polarization. Unfortunately, this is inside the inner boundary of our simulations. We directly estimate the inflow rate to be $\sim 10^{-6}$

$M_\odot$/yr at $\sim 10^3$ r_s from the simulations. Extrapolating our curve to 100 r_s places the inflow rate at $\sim 1 - 2 \times 10^{-7}$ $M_\odot$/yr (with the inferred net accretion rate less than or equal to this value), just inside the limit placed by [81]. Note, the flattening of the inflow rate at low radii in the simulation is an artificial feature, due to its proximity to the inner boundary. Thus, we have neglected it in the extrapolation.

We predict a mass inflow rate of $\sim 10^{-4}$ $M_\odot$/yr $\approx 2.4 \times 10^{-3} \dot{M}_{Edd}$ at $r_b \approx 4 \times 10^5 r_s$. This rate is well within the limits placed by estimates of stellar mass loss in the vicinity of Sgr A*. There are ~ 30 stars that have important mass loss rates [94, 25], with individual mass-loss rates in the range $5 \times 10^{-6} - 10^{-4}$ $M_\odot$/yr [83, 24]. This inflow rate at r_b is also approximately an order of magnitude below that required for the hot accretion flow solution [70].

The mass outflow rate roughly follows the mass inflow rate as a function of radius, leaving the two in approximate balance, and creating an approximately constant net mass accretion rate. This means that at all radii, the *net* mass accretion is extremely low. Approximately 1% of the material that is accreted at r_b makes it to radii of 10^3 r_s, with the rest being driven out in the polar outflow. This outflow has a large opening angle, defined to be the angle in ϕ that has a positive time-averaged radial velocity, of $\sim 130 - 140°$. The density weighted velocity of the outflow is ~ 350 km/s. This velocity is undoubtedly an underestimate. With the inclusion of magnetic fields and the self consistent generation of feedback, we expect this velocity to increase. Thus, until this type of fit is done with a 3-D MHD simulation, it is unclear how much kinetic energy is stored in the polar outflow. Further, we are still unable to determine where this energy will be deposited and therefore exactly how much feedback it represents.

2.5.2 Observational Predictions

Hopefully, with the launch of Athena, made even more necessary after the breakup of Astro-H, we will have an immensely powerful new tool to probe the hot universe.

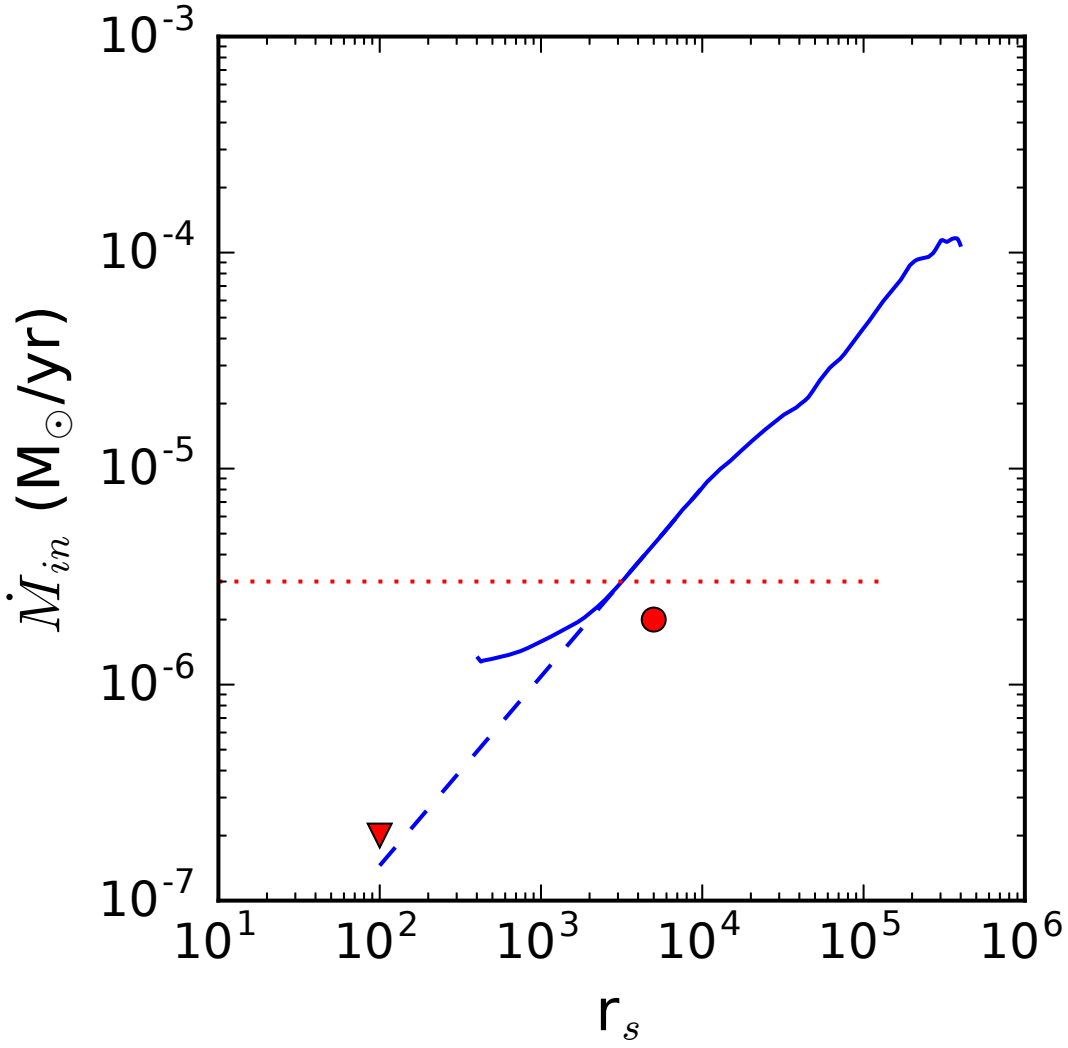

Figure 2.8. The solid line gives the inflow mass flux, temporally and azimuthally averaged, as a function of radius. The dashed line provides an extrapolation to lower radii. The red dotted line is the estimate made by [2], based on the cumulative emission within 2×10^5 r_s, assuming Bondi accretion. The circle is the estimate made with the simulations of [24]. The upper limit placed by [81] is the upside down triangle.

Unfortunately, the spatial resolution of the Athena instrument is only ~ 5", comparable to r_b for Sgr A*. However, the effective area and spectral resolution (2.5 eV; goal of 1.5 eV) are much improved. Thus, by analyzing line profiles, an observation of the Sgr A* complex with Athena will be able provide some very good dynamical information about the flow. Further, at this spectral resolution, different lines can be used to probe different regions of the flow. This is particularly true if the goal of 1.5 eV is met, which would give enough resolution to have diagnostic power for lines spanning from 2-7 keV.

For example, we consider the strong He-like Fe XXV Kα resonance line at 6.7 keV [131]. A spectral resolution of 2.5 eV is equivalent to ~ 100 km/s at 6.7 keV. This is incredibly good resolution, considering for our model, the gas that emits in the Fe XXV line has velocities up to $\sim 500 - 2000$ km/s. We have simulated this line's emission for a 500 ks observation of Sgr A* (Figure 2.9) for both the *plaw* and *plaw* $-$ *wp* models (ignoring bulk turbulent motions). Note, we have only displayed the high energy side of the line, as the low energy side will be contaminated by other Fe XXV transitions. However, since the plasma is optically thin, it will be symmetric about 6.7 keV. We see that the two models can easily be distinguished from each other using the line profile for this depth of observation. Thus, line profiles as observed with Athena can be used to independently constrain the inclination angle of the accretion flow. Not only does this illustrate a way to incorporate more information and greatly constrain the Sgr A* accretion flow, but also highlights the immense diagnostic power of Athena.

Even though Athena promises to be a great leap forward, it will still leave a fair amount to be desired for those who want to do spatially resolved spectroscopy. However, such an instrument is not outside the realm of reality. The proposed X-ray Surveyor would be the proverbial holy grail of X-ray astrophysics. With spectroscopic resolution comparable to that of Athena, spatial resolution similar to that of Chandra,

and $\sim$ 50x better effective area as that of Chandra, we would be able to map individual lines within r_b. Spatially modelling many of these lines simultaneously would provide incredible constraint on the structure of the accretion flow, potentially allowing us to reconstruct the 3-D inflow and outflow structure.

2.5.3 Faraday Rotation Measurements

If the type of fitting in this paper is done with a 3-D MHD simulation then we can utilize other observations to constrain the accretion flow, most notably, Faraday rotation measures. This measure is the integral of the product of the density and parallel magnetic field along the line of sight, $\propto \int n_e \vec{B} \cdot \mathrm{d}\vec{l}$. This measure has already been successfully used to place limits on the accretion rate very near the BH. Assuming some basic structure and energy equipartition, [81] place a lower and upper limit of 2e-9 $M_\odot$/yr and 2e-7 $M_\odot$/yr near the BH, respectively. Others, such as Li et al (2015), have attempted to make calculations based on some toy models, in an attempt to understand the accretion and outflow processes, but have met with contradiction between their estimate of the flow's inclination angle and that of the stellar disk.

With the new RRIOS simulations, we now have an understanding of the general distribution of material around the BH. In principle, we could use the rotation measure as a constraint with the current 2-D simulation that we have used, assuming some limiting cases of the magnetic field geometry. While we are not willing to make such assumptions at this time, these magnetic fields will be generated self-consistently in a 3-D MHD simulation, giving us more information to leverage in our quest to understand the low accretion phase and its mechanical feedback. However, at this time we leave such work for a future paper.

2.5.4 Further Numerical Considerations

We have discussed many reasons why it is important to do the type of fit presented here with a 3-D MHD simulation, including Faraday Rotation estimates and the self-

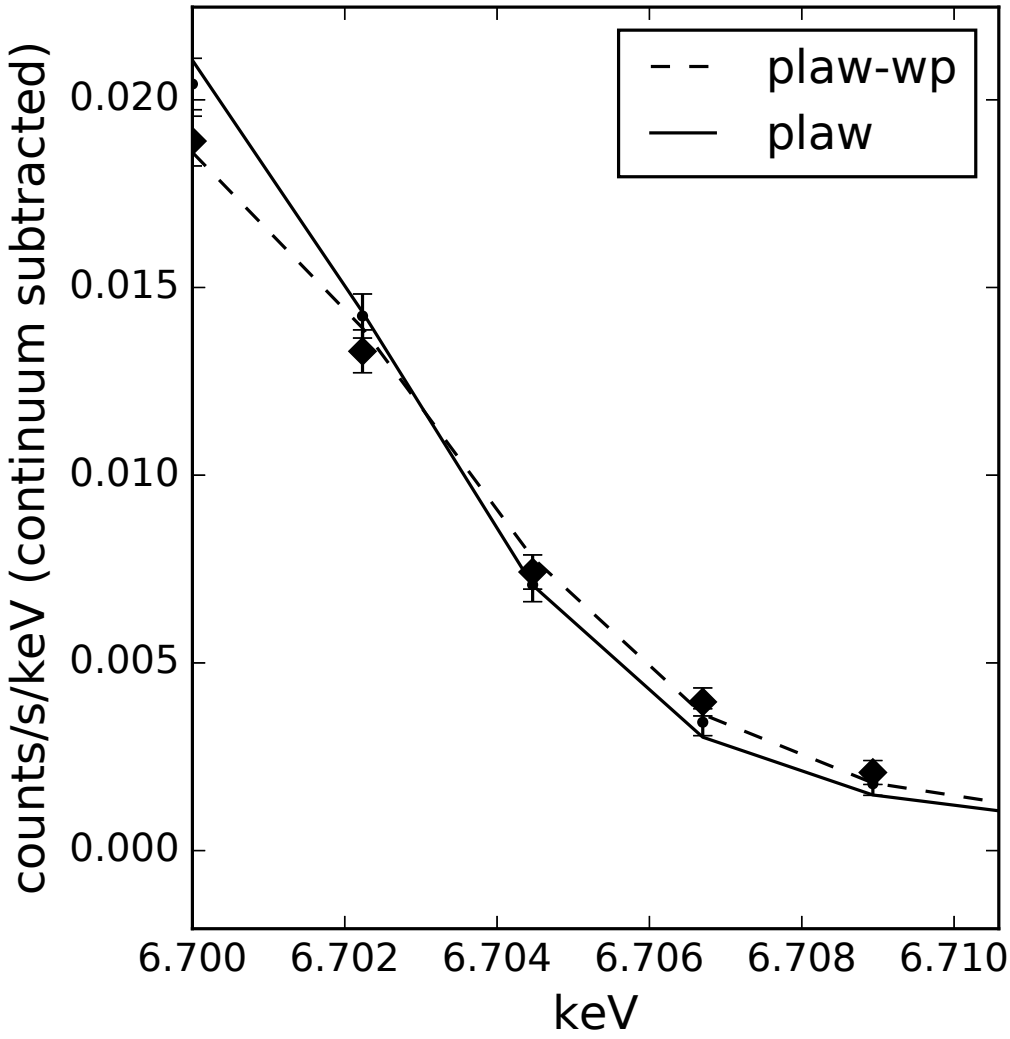

Figure 2.9. Simulated line emission (continuum subtracted) for the Fe XXV Kα resonance line at 6.7 keV observed with Athena for 500 ks. Bin size is $\sim$ 2.25 eV. Diamonds correspond to simulated bins for the $plaw - wp$ model, and dots to the $plaw$ model.

consistent generation of feedback and outflow velocity. We should, however, point out an additional numerical concern. Our current simulations, in using an artificial viscosity, may not be modelling the transfer of angular momentum as accurately as we would like. While previous work suggests the inclusion of magnetic field has little effect on global properties such as the density profile [6, 142], any change in the transfer of angular momentum would have strong consequences for the radial density profile, which is the primary constraint on the angular momentum through the centrifugal radius. Therefore, we believe that the global parameters, particularly the angular momentum of the flow, which is tightly constrained here, could change. However, care has been taken to make the simulated flows as realistic as possible. But, in any case, detailed 3-D MHD simulations should be carried out, starting with the best fit parameters, to check various consistencies and to address the role of magnetic fields.

2.6 Summary and Conclusions

While self-consistently connecting the outflowing gas to the surrounding circumnuclear area remains an outstanding challenge, significant strides have been made in recent years modelling the physics surrounding low luminosity BHs, in particular Sgr A*. Since it is numerically infeasible to simulate from very near the black hole through the accretion flow to the origin of the feeding material and its subsequent outflow deposition area, many orders of magnitude in resolution, the community has resorted to modelling in specific spatial domains. [139, 3] have made great strides recently in simulating the physics very close to the BH, and from the other end, [25] have done a great deal to simulate the accretion flow from its orgins. In between the two regimes, we are able to place significant constraint on the the structure of the accretion flow within the Bondi capture radius by linking observations to simulated 2-D RRIOS accretion flows with MCMC fitting, self-consistently modelling the inflow

and outflow regions simultaneously for the first time. This lends necessary boundary conditions for those that seek to understand the flow at its inner and outer limits. Specifically:

- The best fit temperature at the Bondi radius is 1.3e7(1.24e7,1.38e7) K and is consistent with an origin of shocked stellar wind material of velocity $\sim$ 1000 km/s.

- The best fit electron density at the Bondi radius is 101.6 (91.4,111.1) cm^{-3} and is consistent with estimates of stellar mass loss from stellar winds in the central cluster.

- The angular momentum of captured gas, as parameterized by the centrifugal radius, is best fit as $r_c = 0.058(\pm 0.006)\ r_b$. This is the first observational constraint on the centrifugal radius, and provides an important condition for modelling as we move forward.

- Low angular momentum accretion (Bondi-like) leads to too steep a density profile to spatially model the observed emission simultaneously at small and large radii.

- We find the unresolved point-like quiescent emission is too steep ($\alpha = 4.8(3.5,7.5)$) to be characterized by Bremmstrahlung emission or undetected flaring emission of the same spectral shape as those of detected flares. This emission is likely due to a combination of inverse-Compton scattering of low frequency synchrotron emission by thermal electrons and synchrotron emission from a small percentage of electrons that are accelerated into a powerlaw tail.

- The mass inflow rate at r_b is $\sim 10^{-4}\ M_\odot$/yr. This rate is well below the expected gas supply due to stellar wind mass loss in the vicinity of Sgr A*.

- The radial profile of mass inflow is incredibly steep due to the strong balancing outflow, resulting in a mass inflow rate $\sim 10^{-6}$ $M_\odot$/yr at $\sim 10^3 r_s$, consistent with simulations of stellar wind dynamics. This directly implies a net mass accretion rate of $\leq 10^{-6}$ $M_\odot$/yr onto Sgr A*. Extrapolating the mass inflow profile to lower radii results in an accretion rate at low radii that is consistent with estimates from Faraday rotation measures.

- The polar outflow has an opening angle of 130-140° and a velocity of ≈ 350 km/s. We expect this predicted velocity to increase with inclusion of magnetic fields. The effects of this polar outflow should be observable, either through its impact with the surrounding ISM or spatially-resolved X-ray spectroscopic studies of the accretion flow.

The work herein is comprehensive, giving the first globally consistent picture of the Sgr A* accretion flow. However, there is much that can be done to verify and push this study further as computational power grows and the next generation of X-ray telescopes are launched. From the computational side, we can begin by running these simulations in 3-D. This will allow us to include magnetic fields, thereby self-consistently modeling the viscosity and feedback in the accretion flow. The next step would be to realistically simulate the gas from its origin to within the centrifugal radius. Observationally, a better determination of the truly quiescent IR flux is of paramount importance, which provides the strongest constraint on the non-thermal electron population. In X-rays, with the release of Athena, and ideally the X-ray Surveyor, we may be able to more directly check our results by doing high-resolution spectroscopy with its non-dispersive spectrometer and far superior effective area ($\sim$ 100x Chandra). Leveraging such an instrument to extract the dynamics of individual lines will allow us to greatly constrain the flow structure, to the point of potentially mapping the inflow and outflow regions.

CHAPTER 3

EMISSION LINE MAPPING OF GRATING SPECTROMETER DATA

3.1 Introduction

Supermassive black hole (SMBH) and stellar feedback are important ingredients in the present theory of galaxy formation and evolution. Models without these feedback mechanisms produce far more stellar mass in the universe than is observed, overpredicting the number of galaxies at all mass scales (e.g., [134, 58, 60]). Thus, feedback is an important regulator of star formation in *all* galaxies, large and small, spiral and elliptical. Unfortunately, these feedback ingredients have hardly been tested and quantified observationally. Under what circumstances are individual, physically distinct modes of feedback important? To what extent does each mode regulate star formation via ejective and/or preventative feedback? These fundamental uncertainties betray the holes in our knowledge of galaxy evolution and highlight the dire need for observational illumination.

Spectroscopy is the lifeblood of observational astrophysics. Without spectroscopy, it becomes nearly impossible to ground astronomical observations in any sort of physical mechanistic sense. In order to understand the dynamic, and often violent, macrophysical processes that regulate the growth of galaxies, it is necessary to visualize the nuances of the microphysical processes through spectroscopy. However, for an object whose emission is even mildly complex, spectroscopy in and of itself is not immensely more useful than imaging when it is done in an object integrated fashion. For diffuse emission, the true holy grail lies in spatially-resolved spectroscopy.

Spatially resolved spectroscopy is extremely important for one simple reason. When viewing an object's integrated spectrum in a single waveband, many different physical conditions can mimic each other in a spectrum. Beyond our own physical intuition, it may be unclear which model is appropriate for the given situation. Further, the relevant non-CIE model may not exist. A statistical model comparison may not provide any illumination either, as there are many degenerate model parameters, particularly when fitting individual elemental abundances. This degeneracy paralyses the ability to numerically describe many effects of galactic feedback on the hot galactic and intergalactic plasma, a major component of the baryonic universe and one that is directly linked to the feedback processes themselves. However, each of the different emission mechanisms generates a distinct spatial pattern for different emission components, making spatially resolved spectroscopy a natural approach for elucidating this spectral obfuscation.

Spatially resolved spectroscopy of X-ray CCD data has been increasingly attempted (e.g., [31, 105, 18, 72]). The algorithm employed hitherto has been to perform separate spectral analyses on data from different tessellated regions of equivalent signal-to-noise. This procedure has been done for both the Chandra ACIS-I and XMM-Newton MOS instruments, both of which only provide moderate spectral resolution. While this form of spatially resolved spectroscopy may illuminate the presence of issues through odd temperature and abundance patterns (e.g., [57, 107]), it suffers from many of the same issues as object integrated spectroscopy. Specifically, the assumption that the gas is optically-thin and in collisional equilibrium (CIE) is often detrimental to the advancement of knowledge.

In X-rays, astrophysicists rely heavily on the assumption that the plasma is optically-thin and in CIE. Further, most spectral analyses are done on moderate resolution spectra, which are unable to truly test the appropriateness of this assumption. While it might be clear from fitting results that something peculiar is occurring

(e.g., [57, 107]), such need not be the case, leaving us with little to no understanding of the bias in our results.

Grating spectrometers, which do have the spectral resolution to extract the relevant diagnostics, have shown exactly how poor the assumptions of optically-thin and CIE typically are (e.g., [104, 77, 146]). However, these instruments have hitherto been of limited use for spatially resolved emission due to spatial and spectral confusion. Yet, X-rays are the prime window for directly observing much of the galactic feedback. Thus, the concerns raised above outline a serious observational hindrance to understanding much of galactic feedback.

To diagnose the appropriateness of the optically-thin and CIE assumptions, the so-called *G-ratio* of He-like Kα transitions is useful. He-like Kα transitions correspond to a triplet of lines from the first excited state to the ground state of Helium-like ions (those with two electrons): the resonance (R), inter-combination (I), and forbidden lines (F). The G-ratio is given as $\frac{F+I}{R}$. Non-CIE emission processes, such as charge exchange (CX) and overionization (recombining plasmas), preferentially populate the forbidden line relative to the resonance line, enhancing the G-ratio by up to a factor of more than ten. Another complication of the X-ray emission of spheroids that needs to be explored is the scattering of resonant emission lines by the X-ray-emitting plasma itself (e.g., [96]). Such scattering re-distributes optically-thick emission line photons to the outer regions of the source. Due to its large oscillator strength, the resonance line emission can be redistributed through this process while leaving the spatial distribution of the forbidden and intercombination lines intact.

It is the G-ratio diagnostic that is uniquely resolved with a grating spectrometer, making the grating a very powerful tool for understanding non-CIE emission processes, and by extension galactic feedback. However, grating spectrometers come with their own unique issues. By dispersing light into the spatial dimension, they are able to obtain very high resolution spectra. Unfortunately, this also means they

confuse spatial and spectral information for an extended source. This is the reason why the majority of analysis using X-ray grating spectrometers has been focused on point-like emission.

As we look to a future with Athena, where spatially resolved spectroscopy is by design, we need not sit on our hands. There is work that can be done now to take advantage of the current fleet of telescopes to spatially resolve the nuances of the X-ray universe. Specifically, with thoughtful analysis, the current set of grating spectrometers can be repurposed to illuminate a much deeper spatial understanding of the hot, diffuse universe. For isolated lines, this is relatively straightforward. Assuming the line energy of every photon (i.e., neglecting velocity dispersion; however, in principle, this can be modelled as well), a photon's detected dispersion coordinate can be translated into the spatial coordinate with a simple application of the grating equations. For He-like Kα triplets, however, the emission lines may significantly overlap due to the spatial extent of the source. In this case, the mapping becomes slightly more complicated. Yet, we can take advantage of multiple observations at different roll angles to overcome this challenge in a very general sense. This results from the fact that the wavelength dependence always follows the roll angle of the telescope while any spatial structure is fixed. A very crude form on this type of emission line mapping was previously performed by [128, 4], however, only for isolated lines.

XMM-Newton's RGS instrument, with a spectral resolution of $\sim$ 3 eV, will be the tool of choice for a demonstration of the power of grating line mapping. The reasons for using RGS are four-fold. First, XMM-Newton has a bandpass of 0.35-2 keV, making it optimal for studying both the OVIII Lyα transition and the OVII Kα transitions. Second, the RGS instrument was active for nearly every XMM-Newton observation. Therefore, it has a great deal of archival data to analyze. Third, XMM-Newton has the largest effective area of the grating instruments in the soft X-rays

($\sim$ 100 cm^2), making the possibility of spatially-resolved spectroscopy a much more tantalizing prospect. Most important, however, is the large dispersion angle that makes the line confusion relatively small, even for moderately extended sources of a few arminutes across. Therefore, while everything discussed herein is generalizable to the HETG and LETG instruments on Chandra, it is only useful for substantially more compact and intrinsically brighter sources. For analysis of more extended objects with HETG and LETG, all emission lines must be modelled simultaneously.

3.1.1 M31 as a Test Case

The central bulge of M31 provides a unique test environment for feedback in galactic spheroids. Beyond their physical morphology, spheroids are unique in that they are typically void of current star-formation, beyond a minute residual amount, and the gas that resides within them is typically hot, which is observed in the X-rays. They contain two classes of objects that may contribute siginificant to feedback and continuously heat the gas: a stellar population that is predominantly old, which contributes late-time stellar feedback, and a supermassive black hole (SMBH) at their heart. Disentangling the relative importance of the two for keeping the gas hot inside galactic spheroids through a range of masses will require analysis of a statistically representative sample of galaxies. However, this case study can certainly provide some new and unique insights.

Late-time stellar feedback, primarily in the form of mass loss from evolved stars and type Ia supernovae, may serve to keep the interstellar gas hot, as well as drive outflows in galaxies with a predominantly aged population [123]. The bulk of the mass, energy, and metal inputs is believed to be ejected with spheroid-wide winds or subsonic outflows (e.g., [15, 123, 124, 122]). Evidence for this is primarily based upon simulations [124, 123]. Observational evidence, built upon peculiarities of the iron abundance's radial profile (e.g., [123] and references therein) and X-ray morphology

(e.g., M31, [74]; M104 or Sombrero, [73]; [13, 64]), is circumstantial and not well reconciled with theoretical predictions. Further, there are prominent suggestions of non-standard emission processes (i.e., the emission is either not in CIE and/or optically-thick; hitherto referred to as non-CIE for brevity) seen in the He-like Kα triplets which cannot be explained with the current modelling [73]. Therefore, it is highly unlikely that current estimates of chemical composition are reliable.

SMBH feedback arises from energy released through the inflow of gas toward a SMBH at the center of a galaxy. If the accretion flow becomes dense enough, it will be able to cool and condense into a thin disk. This is referred to as the high-luminosity active galactic nuclei (HL-AGN) scenario. After the density is large enough for the flow to flatten out, viscous energy is readily transformed into radiative energy. The radiation field from the disk becomes so great that it controls the ionization state of the surrounding hot gas. Indeed, even after the accretion flow lessens and the radiation field subsides, the over-ionization state can persist in the form of an AGN relic. This scenario has recently been proposed to be responsible for the diffuse X-ray excesses observed in galactic nuclear regions (e.g., [130, 110]), as well as the ionization of cool gas far away from post-active galaxies (e.g., [103, 59]). This effect can be directly observed with X-ray observations of galactic spheriods and may be used to provide constraints on the the recent history of the AGN and SMBH feedback in general.

To study the effects of these two enigmatic feedback mechanisms, it would be useful to map the thermodynamic and chemical structure of the hot gas within the bulge. However, there is a wrinkle in the emission that prevents study with conventional methods and assumptions. The emission exhibits an elevated G-ratio of the OVII Kα triplet in the inner bulge (~ 1.5), indicating the present of some non-CIE emission or scattering process. This is what makes the prospect of studying the M31 bulge with innovative methodology particularly tantalizing. CX has previously been

suggested as a possible cause of the elevated G-ratio [77]. However, there is very little dust and neutral gas in the bulge [33, 32, 14], making CX unlikely. Alternatively, [145] have found that a relic AGN could also produce the elevated G-ratio, as well as generally match the RGS spectrum. Under this scenario, we expect the G-ratio to be largest at large radii and lowest at low radii, where the density is highest, allowing for a faster return to equilibrium.

Additionally, preliminary estimates of resonance scattering suggest that it may be important for key resonance lines. This effect on the spatial distribution of the Fe XVII $3d-2p$ transition has clearly been shown with RGS observations of a few giant elliptical galaxies [137, 132]. Resonance scattering works by redistributing optically thick resonance line photons to the outskirts of a galaxy. Thus, under this scenario, we expect the G-ratio to be largest near the center of the galaxy and to decrease at larger radii. While the effectiveness of the scattering is not clear in low L_X/L_K spheroids (such as the bulge of M31), which contain relatively low temperature and low column density hot plasma, preliminary estimates indicate that the scattering of the OVII Kα and OVIII Lyα resonance lines could be significant in the inner bulge region of M31. The firmness of these estimates largely depend upon how small the bulk and turbulent velocities of the plasma are. Conversely, the quantification of resonance scattering can be used to place thus far unique constraints on the kinematics of the plasma.

Therefore, there are two primary mechanisms that we will explore as responsible for the elevated G-ratio: resonance scattering and a relic AGN. We expect each of these to have a distinct G-ratio spatial pattern, making this analysis diagnostically useful. By helping to elucidate the physical mechanism behind the elevated G-ratio for OVII in M31, we demonstrate the diagnostic power of this methodology.

3.1.2 Study Outline

We herein describe a method for taking the spectroscopic capabilities of XMM-Newton's reflective grating spectrometer (RGS) system, and by extension all other dispersive systems, to the proverbial next level. First we demonstrate how to extract spatial information from the dispersive RGS system, using the grating equations to project emission into the spatial coordinates. We then demonstrate the method's utility for distinguishing between emission mechanisms with the M31 data. We go on to discuss the implications of this fit in the larger context of galactic feedback in spheroids, as well as the broader limitations and potential of the method.

3.2 Methods

Prior to any fitting, the data must be properly processed. To provide some clarity on this process, we here first outline the fitting procedure. The fitting requires calculation of the probability of the data given the model, also known as the likelihood. When doing this, we assume that the data is generated through a Poisson process. Thus, for every pixel of each observation we must calculate the expected number of counts in order to calculate the Poisson likelihood of the observed number of counts. The likelihood is relatively straightforward to calculate for an isolated line. We begin by constructing a source flux map, $\vec{I}_{src}$, from our sampling parameters. We perform a double convolution on $\vec{I}_{src}$ to account for the PSF and LSF, respectively. This is converted to an expected counts map, $\vec{C}_{src}$, by multiplying by the source fluxing map, $\vec{F}_{src}$. We then add it to the background count map, $\vec{C}_{bkg}$, which is generated by multiplying the background flux map, $\vec{I}_{bkg}$, by the background fluxing map, $\vec{F}_{bkg}$. The background needs to modelled in the flux domain, as its effective area is not necessarily smooth and may be non-linear. This procedure generates the expected number of counts in each pixel, from which we may calculate the likelihood.

For blended lines, there is an additional set of steps. A source flux map is generated for each line. After these lines are convolved, they are dispered, multiplied by their relevant fluxing maps, and added together to create a total expected source count map, $\vec{C}_{src}$. In this case, each source line has its own fluxing map as each line energy has a different effective area. After this, the source flux can be added to the expected background count map as was done for the isolated line, creating an image from which we may calculate the likelihood.

3.2.1 Data Reduction

We analyze a total of 32 observations of the M31 bulge (Table 3.1), amounting to 582 ks of observing time. The standard event files and response matrices are produced using the *rgsproc* pipeline of the Science Analysis System (version 15.0.0). Good time files are produced by visual examination of the light curve to remove flares. Within the *rgsproc* pipeline we specify the source location as the center of the galaxy (R.A. = 00h 42m 44.3503s, Dec. = 41d 16m 08.634s; [37]). This handles corrections for boresight in the calculation of the line wavelengths. While this pipeline does much of the heavy lifting in terms of data reduction, it is designed for point sources and does not directly provide information on the spatial distribution of an extended source. To extract spatial information from the data, we need to consider the optics of the RGS system.

3.2.2 Count Map

For a given line of interest, we can place two selections on the data to limit contamination *a priori*. The most obvious is a limit on the event wavelength, as determined by *rgsproc*. The choice of limiting wavelengths has some leeway in regards to their exact values depending upon the physical extent of the source. However, it is important to choose limiting wavelengths that provide enough counts in the

Table 3.1. M31 observations.

Obs. ID	Date	t_{obs} (ks)	t_{eff} (ks)
0109270101	6-29-2001	57.9	24.5
0112570101	1-6-2002	64.3	50.9
0112570401	6-25-2000	46.0	31.8
0112570601	12-28-2000	13.1	7.4
0405320501	7-2-2006	21.9	12.3
0405320601	8-9-2006	21.9	6.1
0405320701	12-31-2006	15.9	14.6
0405320801	1-16-2007	13.9	11.9
0405320901	2-5-2007	16.9	14.4
0505720201	12-29-2007	27.5	23.2
0505720301	1-8-2008	27.2	21.9
0505720401	1-18-2008	22.8	17.8
0505720501	1-27-2008	21.8	13.1
0505720601	2-7-2008	21.9	18.3
0551690201	12-30-2008	21.9	18.5
0551690301	1-9-2009	21.9	18.1
0551690401	1-15-2009	27.1	6.9
0551690501	1-27-2009	21.9	17.2
0600660201	12-28-2009	18.8	16.3
0600660301	1-7-2010	17.3	15.3
0600660401	1-15-2010	17.2	14.4
0600660501	1-25-2010	19.7	13.1
0600660601	2-2-2010	17.3	15.7
0650560301	1-4-2011	33.4	29.5
0650560401	1-14-2011	24.3	15.6
0650560501	1-25-2011	23.9	18.3
0650560601	2-3-2011	23.9	22.8
0674210201	12-28-2011	20.9	20.4
0674210301	1-7-2012	17.3	15.5
0674210401	1-15-2012	19.9	19.7
0674210501	1-21-2012	17.3	17.2
0674210601	1-31-2012	26.0	18.9

Table 3.2. Line selections and parameters.

Line	λ_0 (Å)	PI_{min} (eV)	PI_{max} (eV)	λ_{min} (Å)	λ_{max} (Å)	Bkg. Width (Å)
OVII	21.85	425	710	20.35	23.35	0.5
OVIII	18.967	518	790	17.717	20.217	0.5

continuum dominated regions to estimate the background, as discussed below, while minimizing potential contamination from adjacent lines.

In addition to the wavelength estimated from the grating equations, the low-resolution CCD pulse-height (PI) estimate of a photon's energy can be used to limit contamination. For the RGS detector, the uncertainty of this estimate is approximately Gaussian with $\sigma \approx 68$ eV. We select events from $\pm 2\sigma$ of the line(s) of interest. Data selections for different lines of M31 data are summarized in Table 3.2, along with other parameters needed for extracting spatial information as discussed below.

The procedure for mapping events in the cross-dispersion direction is the most readily understood. After choosing a pixel scale, $R \geq R_{rgs} \approx 1$ arcsec/pixel, we can directly calculate the cross dispersion location of the ith event in the spatial image pixel coordinate:

$$X_i = (\delta\mathrm{XDSP} + \mathrm{XDSP}_i * 206264.8)/R \tag{3.1}$$

where XDSP_i is the event's corrected cross dispersion angle in radians, which is calculated by *rgsproc* and corresponds to the $XDSP\_CORR$ column in the standard events file. The factor 206264.8 converts XDSP_i from radians to arcsec, which is converted to pixels by R. The width in the cross dispersion direction is represented by δXDSP, where 2δXDSP corresponds to the total width. We use an extraction region, δXDSP, of 1.8'. This region size was chosen because the effective area does not suffer much loss within this distance. With an adequate model of the cross-dispersion effective area, this may be expanded in later work.

Due to the mixing of spatial and spectral information, determining the pixel coordinate in the dispersion direction is conceptually less straightforward. However, all

dispersion positions derive from the grating equation, which describes how photons are dispersed as a function of wavelength and incident angle:

$$\cos\beta = \cos\alpha + m\lambda/d \tag{3.2}$$

where β is the dispersed angle, α is the incident angle, m is the spectral order, λ is the wavelength of the radiation, and d is the grating spacing. The grating spacing for the RGS system is $\sim 1.549\mu$m. For our purposes, we only use the first order dispersed data, $m = -1$. This constraint could conceivably be loosened for higher energy photons, however, since we are primarily interested in OVIII and OVII, higher orders do not provide any additional information.

To cast this equation into spatial coordinates, we combine it with the equation that relates a photons sky coordinate to its angle of incidence:

$$\alpha = \alpha_0 + \phi\frac{F}{L} \tag{3.3}$$

where ϕ is the off-axis angular position of the source, L is the distance between the reflective grating array and the prime focus (6700mm), F is the focal length (7500mm), and α_0 is the on axis angle of incidence.

Equations 3.2 and 3.3 clarify why blended lines suffer from a degeneracy. From Equation 3.2, it is apparent that the larger the wavelength, the greater the dispersion angle for the same location. However, from Equation 3.3, a greater dispersion angle can also arise through α from a positive off-axis location angle. With multiple observations dispersed in different direction, ideally opposite, this degeneracy can be broken with full generality. This results from the fact that the wavelength dependence always follows the dispersion direction while any offset due to spatial structure is fixed.

Assuming all photons have the same energy (single line energy or multiplet centroid energy; λ_p), that is, any displacement in the dispersion direction is due to spatial changes, the location of the ith photon in the dispersion coordinate of the spatial image is given by:

$$D_{i,obs} = D_{\lambda_p} + \frac{(\alpha_i - \alpha_0)L}{RF} \tag{3.4}$$

where $D_{i,obs}$ is the event position is the dispersion direction, and D_{λ_p} is the on-axis position of the assumed line energy. α is calculated as:

$$\alpha_i = \cos^{-1}(\cos(\beta_i) - m\lambda_p/d) \tag{3.5}$$

where β_i is calculated within *rgsproc* and corresponds to the BETA_CORR column in the standard events file.

Using Equations 3.1 and 3.4, the events are cast into a count image in the nominal coordinates of the source. An example of this for the OVIII Lyα line of M31 for a single observation (effective exposure of $\sim$ 24 ks) is shown in Figure 3.1. Even after rebinning the data to pixels of 10" on a side, the counting statistics of the diffuse line emission are still extremely limiting. Most of the counts in the image represent the dispersed continuum of bright point-like sources[1].

3.2.3 Fluxing Map

In order to compare a model to the data, a fluxing map is needed to convert the model surface brightness of the source line emission, in units of counts/s/cm^2/arcsec^2, to an expected count image. The fluxing map is a combination of the effective area,

[1]These point sources are accreting compact objects whose continuum emission is primarily blackbody from accretion disks, inverse-Compton, and synchrotron emission. Therefore, it does not contribute to the line emission and is considerably easier to remove than if it did.

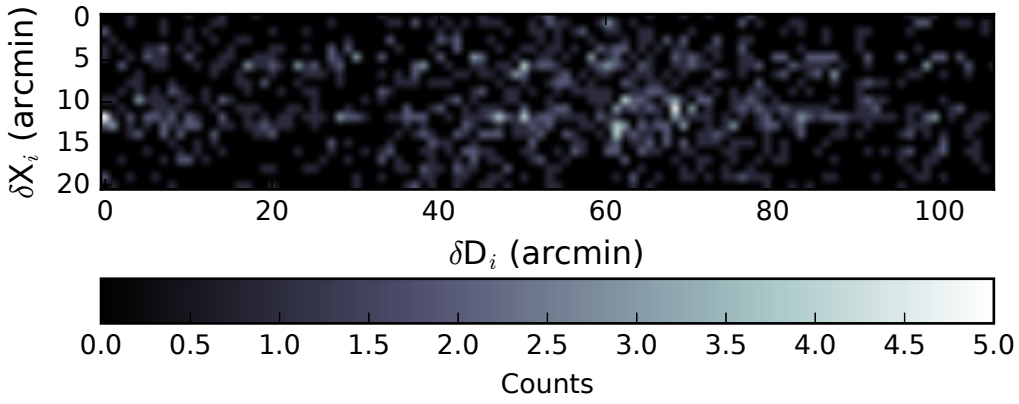

Figure 3.1. OVIII counts map for Observation 0109270101. Pixels are 10" on a side.

exposure, bad pixel corrections, pixel size and vignetting (only for the source line emission). It is unique to both the source and background emission individually. The diffuse gas that comprises the source emission is approximately at a single wavelength, while the background is a combination of instrumental and continuum emission, which spans a range of wavelengths.

Since it is merely a property of the detector, the bad pixel correction of each spatial bin is equivalent for both the background and source emission. It is directly derived from the exposure map generated by *rgsproc*, which gives the effective exposure time at each β + cross-dispersion bin. We simultaneously account for exposure and bad pixels in each spatial bin by summing over all β + cross-dispersion pixels, weighting by the fraction of area that each contributes to the spatial bin. The area contributed by each β + cross-dispersion pixel is determined by calculating the location of the

bin edges using Equations 3.1 and 3.4. This procedure gives the effective exposure time of each spatial bin.

Calculating the effective area is less straightforward. In the dispersion direction, the effective area at some observed line energy, ν_o, is calculated as:

$$A_{\nu_o} = \sum_{\nu_i} A_{\nu_o,\nu_i} \tag{3.6}$$

using the response matrix for a point-source, which gives A_{ν_o,ν_i}, the effective area at each detected energy (ν_o) given an intrinsic energy (ν_i). Unfortunately, the effective area calculated from the *rgsproc* generated response contains corrections for bad pixels without their location in the cross-dispersion coordinate. In order to remove these effects and obtain the underlying smooth response, it is sufficient to remove and interpolate through the bins that are affected by bad pixels. If any dispersion coordinate bin is contaminated by bad pixels through the extent of $\pm 2\sigma$ of the PSF from on-axis in the cross-dispersion direction, then the effective area at that bin is excised and interpolated through. An example reconstruction of the smooth underlying effective area as a function of dispersion coordinate is shown in Figure 3.2. Lastly, recall this effective area is assumed to be constant through the cross-dispersion direction due to the small cross dispersion extraction width.

For the background effective area (discussed below), we use the standard effective area generated by *rgsproc* for a point source after bad pixel effects have been removed. The spatial location of each detected energy is then calculated using Equation 3.2, providing a functional form of the effective area through the dispersion coordinate. Over the narrow extracted wavelength range, the gradient of the continuum emission can be assumed to be approximately constant. Therefore, using the point source response to model the background instead of convolving the point-like response with a spatial model will not result in any gross errors in the estimates of the background

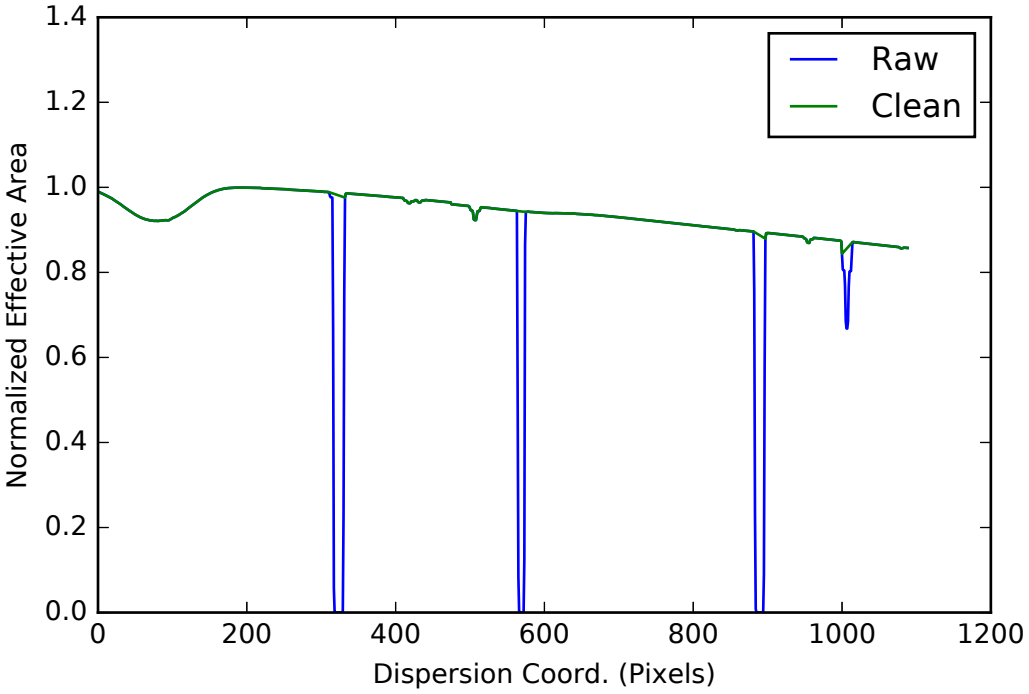

Figure 3.2. OVIII effective area for Observation 0109270101 as a function of dispersion coordinate. Bins are 1" in size.

flux. Further, the background flux value is of little interest to the analysis presented here, as long as the background can be reliably accounted for in the counts image.

For the source line emission, we assume that every photon is of the same energy. Therefore, we expect the effective area to be constant over the image, modulo a vignetting effect. This value can be calculated directly from the interpolated background effective area shown in Figure 3.2 by mapping the line of interest to the spatial domain with Equation 3.4. This value is then multiplied by the exposure map created above which corrects for bad pixels and CCD gaps. The next step is to account for effective area losses of the source emission at large off-axis angles (Figure 3.3) by multiplying by a vignetting factor. Lastly, the fluxing map is divided by the square of the pixel size.

3.2.4 Background Map

The background can arise from three primary sources: instrumental background, diffuse gas continuum, and continuum from point sources. The complexity of modelling these three different contributions individually with all geometric considerations taken into account is incredibly burdensome for very little gain in knowledge. Further, since we are not directly interested in a characterization of the background, as long as it can be reasonably subtracted from the observed emission without being a major source of error or uncertainty, such modelling is beyond the scope of this work. We expect this background modelling to result in a slight underestimate of parameter uncertainty, but the overconfidence will be minimal as our certainty of the diffuse line emission is more limiting.

In order to generate a background map we estimate it directly in the continuum regions surrounding the line(s) of interest, linearly interpolate in between, and consider it fixed. We first collapse some width of the counts and background fluxing maps in the dispersion direction, $\delta\lambda_{bkg}$, to estimate the flux on either side of the

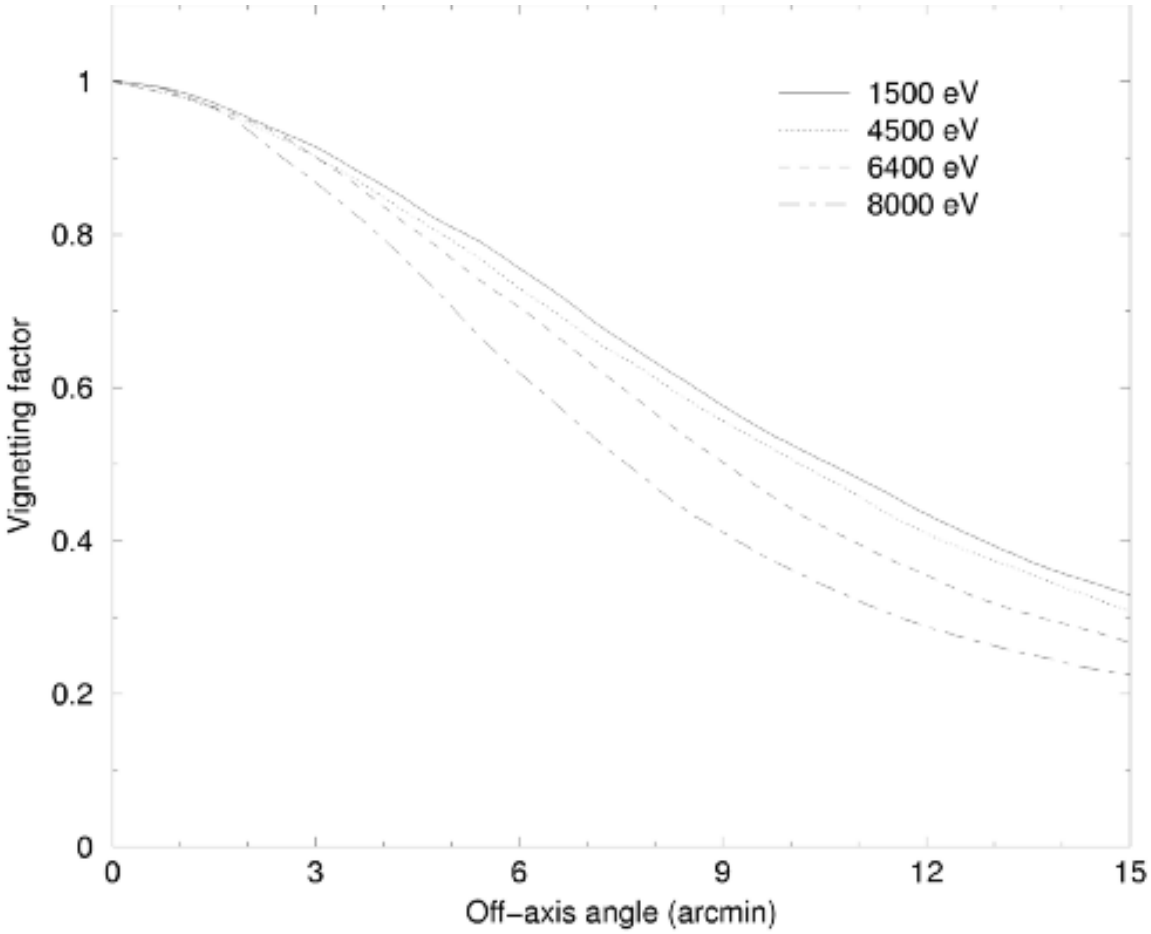

Figure 3.3. The vingetting factor as a function of off-axis angle at several wavelengths. The curve for a 1.5keV photon is used to adjust the flux of all lines sampled in this document. Since this curve does not change significantly at low energies, this will provide a reasonable characterization of any line of interest that is sampled with the RGS system, where the maximum energy of detected dispersed photons is $\sim$ 2 keV. Image is taken from the XMM Users' Handbook.

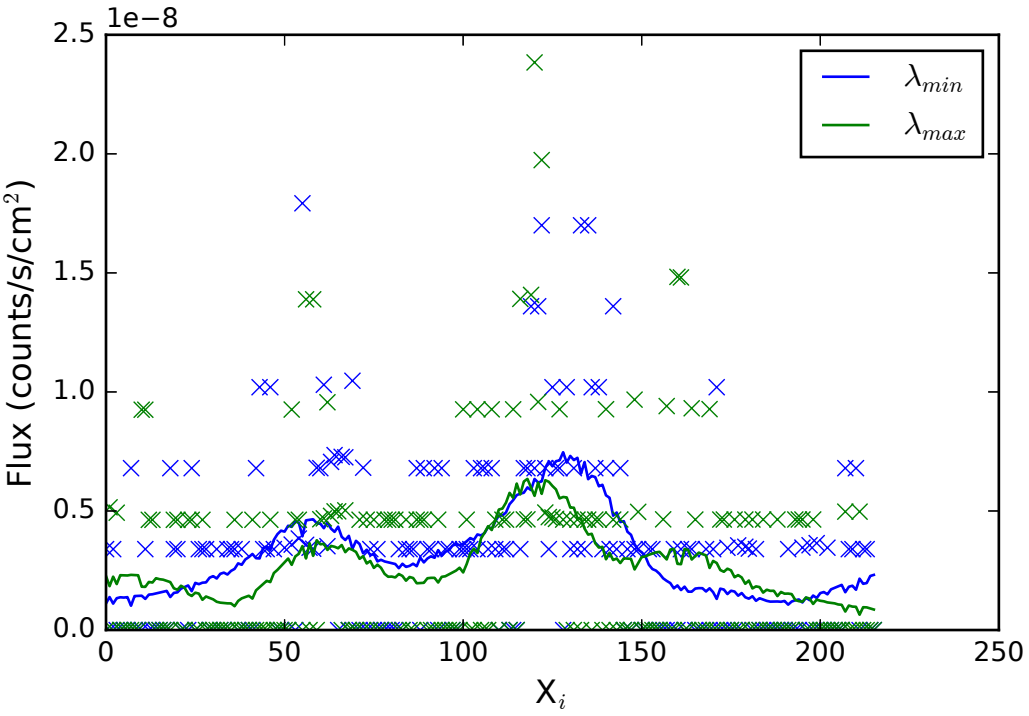

Figure 3.4. Dispersion collapsed continuum region fluxes used to estimate the OVIII background for Observation 010927010. Blue corresponds to the flux at λ_{min} and green corresponds to the flux at λ_{max}. 'X's denote the cross-dispersion row flux in the data and lines are the inferred, smoothed background fluxes at these wavelengths.

observed line image as a function of cross-dispersion coordinate. In the case of M31, for OVII and OVIII we choose this background width to be 0.5 Å from λ_{min} and λ_{max} on either side of the line. This width, along with the total width of wavelength extraction, is chosen to obtain enough counts to accurately estimate the background while minimizing contamination from any line emission in that estimate. For an object that is less extended, one could expand this width to obtain a better estimate of the background. These fluxes are then smoothed with a Gaussian kernel that is approximately equivalent to the cross-dispersion PSF to obtain the final estimated background flux (Figure 3.4). In order to generate the background flux map, we assume these fluxes characterize the background at $D_{\lambda_{max}}$ and $D_{\lambda_{min}}$, respectively, and linearly interpolate between them (Figure 3.5).

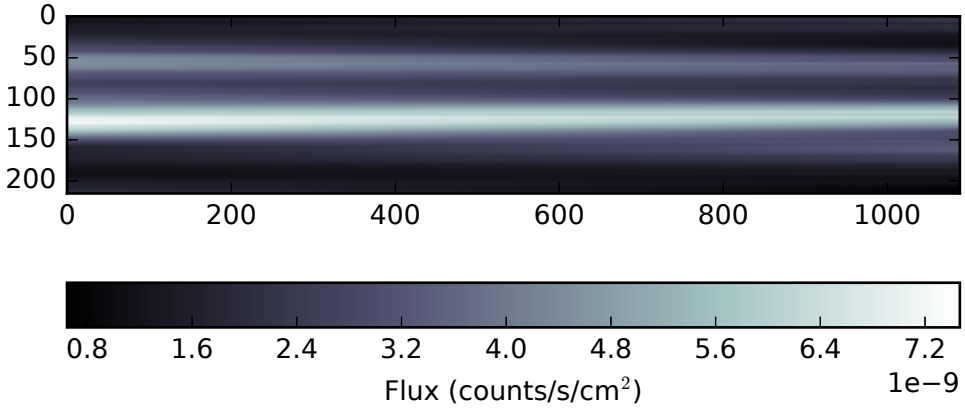

Figure 3.5. OVIII interpolated background flux map for Observation 010927010.

3.2.5 Modelling

Models can be generalized to any functional format desired (including semiparametric surface brightness - see Appendix E for a demonstration). However, because of the very limited counting statistics of M31 we will approximate the diffuse line emission as being produced by an isothermal sphere, which has already been shown to reasonably characterize the broad-band emission ([77]; Figure 3.6). Thus, we parameterize it with the β-model:

$$I(r) = \frac{I_0}{\left[1 + \left(\frac{r}{r_c}\right)^2\right]^{3\beta - 1/2}} \tag{3.7}$$

where I_0 is the surface brightness at the origin, r_c is the core radius where the surface brightness begins its exponential decline, and β determines how steeply the surface brightness declines. This is perhaps the simplest, physically motivated parameteriza-

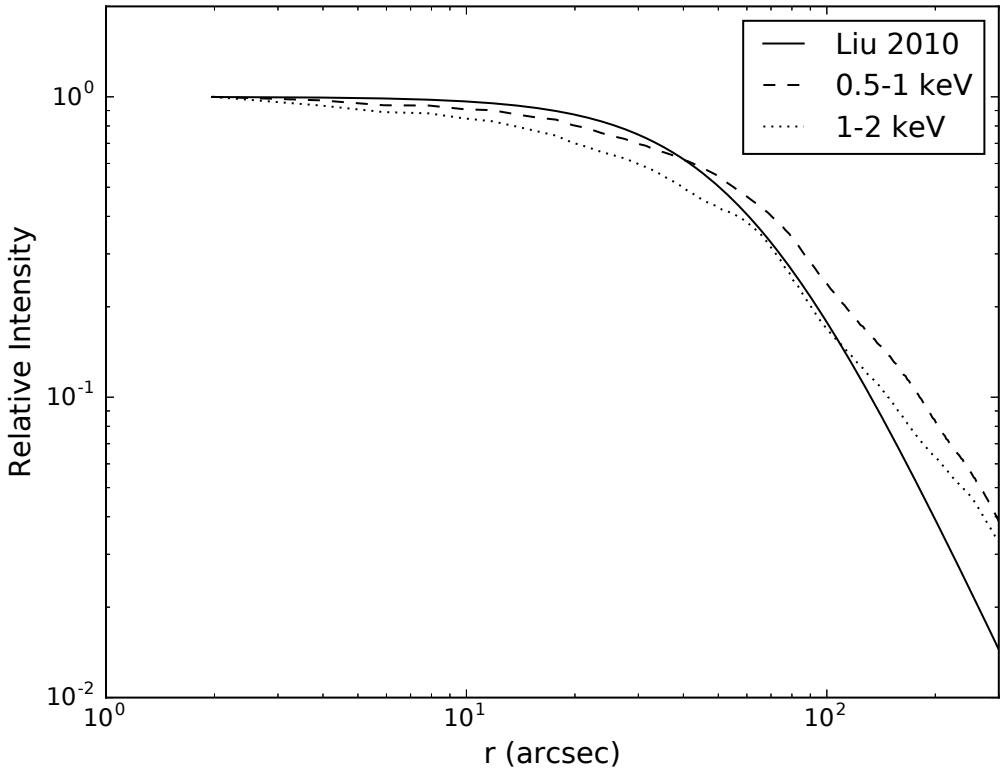

Figure 3.6. Chandra radial surface brightness profiles for M31 in the 0.5-1 keV band (dashed line) and the 1-2 keV band (dotted line). The best fit profile from [77] is given by the solid line.

tion one could imagine for the gas distribution. Not only does Figure 3.6 show that the radial profile follows the characteristic curve of the β-model, but also that there is a very little change in the flux differences between each band with radius. This implies that the X-ray emission from M31 has only a weak temperature gradient, becoming slightly cooler at larger radii, reinforcing the isothermal model as a reasonable approximation. Also, if resonance scattering is important for the emission, it could serve to broaden the soft band due to relatively strong scattering of the OVII and OVIII resonance lines.

We sample parameters using the Metropolis-Hastings Markov Chain Monte Carlo algorithm. This algorithm relies on rejection sampling in order to draw samples

approximately from the posterior probability distribution, or the probability of the model given the newly observed data, which provides the full credibility of parameter values. This can be formalized as:

$$P(\vec{\theta}|\vec{O}) \propto P(\vec{O}|\vec{\theta})P(\vec{\theta}) \tag{3.8}$$

where $P(\vec{\theta}|\vec{O})$ is the posterior probability, $P(\vec{O}|\vec{\theta})$ is the likelihood of the data given the model, and $P(\vec{\theta})$ represents our prior belief about model parameters. As this is a novel analysis without much precendent, all parameters have a prior probability that is uniform in the domain $[0,\infty)$ unless otherwise stated. When calculating the likelihood, we assume all data is Poisson in nature. We simulate and fit data from an isothermal β distribution in Appendix D, showing that the methodology outlined above is able to recover the simulated parameters.

3.3 Results

For reference, the 0.2-12 keV image of the M31 bulge taken with the non-dispersive XMM-Newton EPIC instrument is shown in Figure 3.7 (image taken from [77]). In this image, the white box represents the dispersion axis. The width of this box is 4', suggesting the diffuse X-ray emission is extended to radii of greater than 4'. There are a considerable number of point sources that contribute to the emission. The coherence of these point sources produces the distinct bands in the background estimate (Figure 3.5) through their collectively dispersed continua.

The mean background subtracted flux of OVIII Lyα and OVII Kα can be visualized in Figures 3.8 and 3.9, respectively. These images were created by dividing the raw count image by the fluxing map and subtracting the background map. Visualizing the galactic distribution of hot gas is easier done with OVIII Lyα emission. We see that the emission is quite extended ($\sim 8'$), and is approximately azimuthally

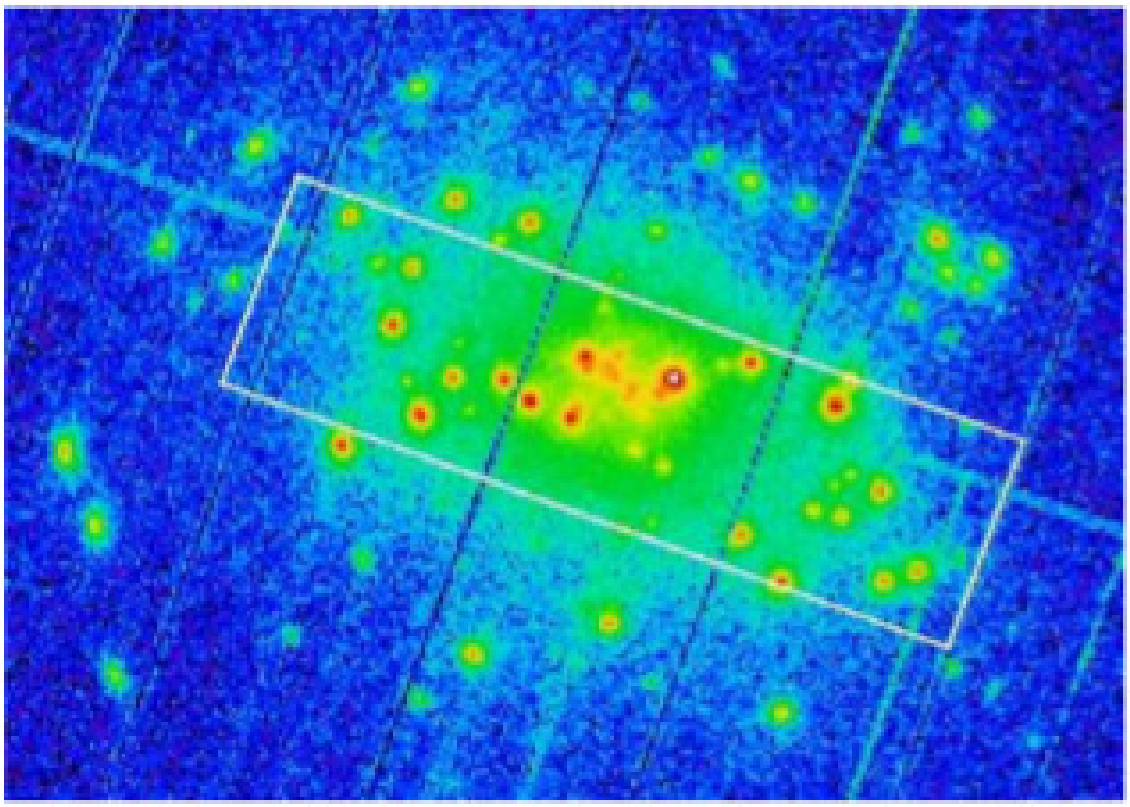

Figure 3.7. Image taken from [77]. M31 bulge image in the 0.2-12 keV band using XMM-Newton's EPIC pn instrument. The long axis of the white box represents the typical dispersion direction of the M31 observations. The short axis, representing the cross-dispersion direction, is 4' wide in this image.

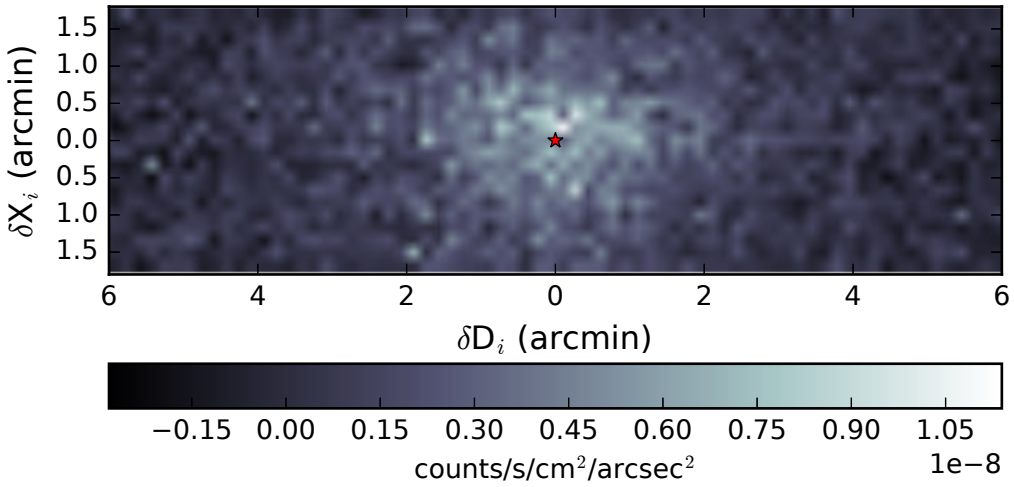

Figure 3.8. Mean background subtracted observed OVIII flux for M31. The red star indicates the location of the galaxy center.

symmetric. There is some elongation in dispersion direction, either due to the LSF or elongation of the emission along the major axis of the galaxy. The surface brightness peaks at galaxy center with $\sim 1 \times 10^{-8}$ counts/s/cm^2/arcsec^2. It then smoothly fades into the background at radii of $> 5'$. This physical extent leads to OVII Kα lines that are well blended. Indeed, it is difficult to visually discern multiple peaks corresponding to the line centers. However, it should be noted that in the left and right side of the image, the emission is dominated by the resonance and forbidden lines, respectively, alone.[2]

[2]Highlighted in red in the OVII Kα emission is a coherent spur of emission where the flux more than doubles. This feature seems unlikely to be physical, and has thus been masked out of the fitting procedure. The origin of this feature needs to be explored in more detail. However, it should be noted that when including this feature in a fit leads to qualitatively similar results.

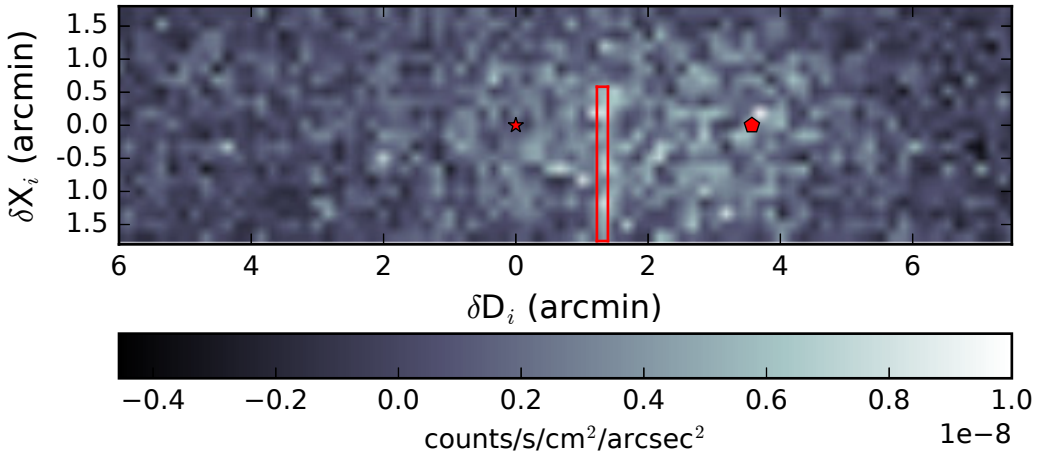

Figure 3.9. Mean background subtracted observed OVII Kα triplet flux for M31. The red star indicates the location of the galaxy center for the resonance line. The red pentagon indicates the location of the galaxy center for the forbidden line. The bright spur outlined in red is removed during fitting.

3.3.1 Understanding the Elevated G-ratio of OVII

The first goal of this work is to discern the physical mechanism (between a relic-AGN and resonance scattering) for elevating the G-ratio. Recall the expectation for the spatial distribution of the G-ratio under each scenario. For resonance scattering, we expect the G-ratio to decrease with increasing radius. Conversely, if a relic-AGN is driving the elevated G-ratio, we expect the G-ratio in increase with increasing radius [145].

To explore the distribution of the G-ratio, we will focus our analysis on OVII. When sampling, we assume that both the resonance line and forbidden line follow. However, since we are primarily interested in the spatial distribution of the G-ratio, we directly sample the spatial distribution of the G-ratio and the surface brightness of the resonance line. The surface brightness of the resonance line is given by the β-model described above, while the G-ratio distribution is characterized by:

$$G(r) = \frac{G_0}{\left[1 + \left(\frac{r}{r_c}\right)^2\right]^{\eta}} \tag{3.9}$$

where G_0 is the core G-ratio, r_c the core radius (assumed to be equal to that of the resonance line distribution), and η defines whether the G-ratio increases or decreases, primarily beyond r_c. Note, a positive η corresponds to a decrease in the G-ratio with radius, and *vice versa*. The priors placed on these parameters are detailed in Table 3.3. Note, because of the poor counting statistics, we have placed an upper limit of 1 on β. This is because, as we will see, β and r_c are highly degenerate, and a $\beta > 1$ loses physical meaning.

The fitting results are listed in Table 3.4 and shown in Figures 3.10-3.12. The highly degenerate parameters of β and r_c are not well constrained, however, this does not mitigate the strength of other conclusions. We see that the core G-ratio, G_0, is approximately 1.5, in agreement with the spectral fitting performed by [77]. Most

Table 3.3. Summary of the priors. U(lower,upper) represents a uniform distribution.

Parameter	Prior
$I_{0,OVII,R}$	U[0,inf)
r_c	U[0,inf)
$\beta_{OVII,R}$	U[0,1]
G_0	U[0,10]
η	U(-inf,inf)

Table 3.4. Joint fitting OVIII and OVII for M31, marginalized parameter best fit and 95% confidence intervals.

Parameter	Best	Lower 95% Limit	Upper 95% Limit
$I_{0,OVII,R}$ (10^{-9} counts/s/cm^2/asec^2)	1.60	1.37	1.95
r_c (asec)	210	107	287
$\beta_{OVII,R}$	0.48	N/A	N/A
G_0	1.50	1.24	1.86
η	1.16	0.37	5.86

interestingly, we find that η is very strongly constrained to be positive, suggesting that there is effectively zero probability of the forbidden line to be more extended than the resonance line. Such a result is qualitatively inconsistent with the relic-AGN scenario, where we expect the forbidden line to be much more extended than the resonance line. Since the compact forbidden line emission provides very strong evidence that resonance scattering is important for modelling the emission in M31, we will perform additional fitting under under this physical framework. This will allow us to make model simplifications and greatly constrain the emission characteristics.

3.3.2 Oxygen Emission in the Resonance Scattering Paradigm

The β-model lends itself well to the resonance scattering scenario. For an isothermal sphere, resonance scattering maintains the β-model functionality [118]. It elevates the G-ratio at the object's core by scattering resonance line photons at the center where the column density is highest, decreasing $I_{0,R}$. However, since these photons are merely scattered, and likely not destroyed, the object integrated G-ratio must remain the thermal value. Resonance scattering accomplishes this by decreas-

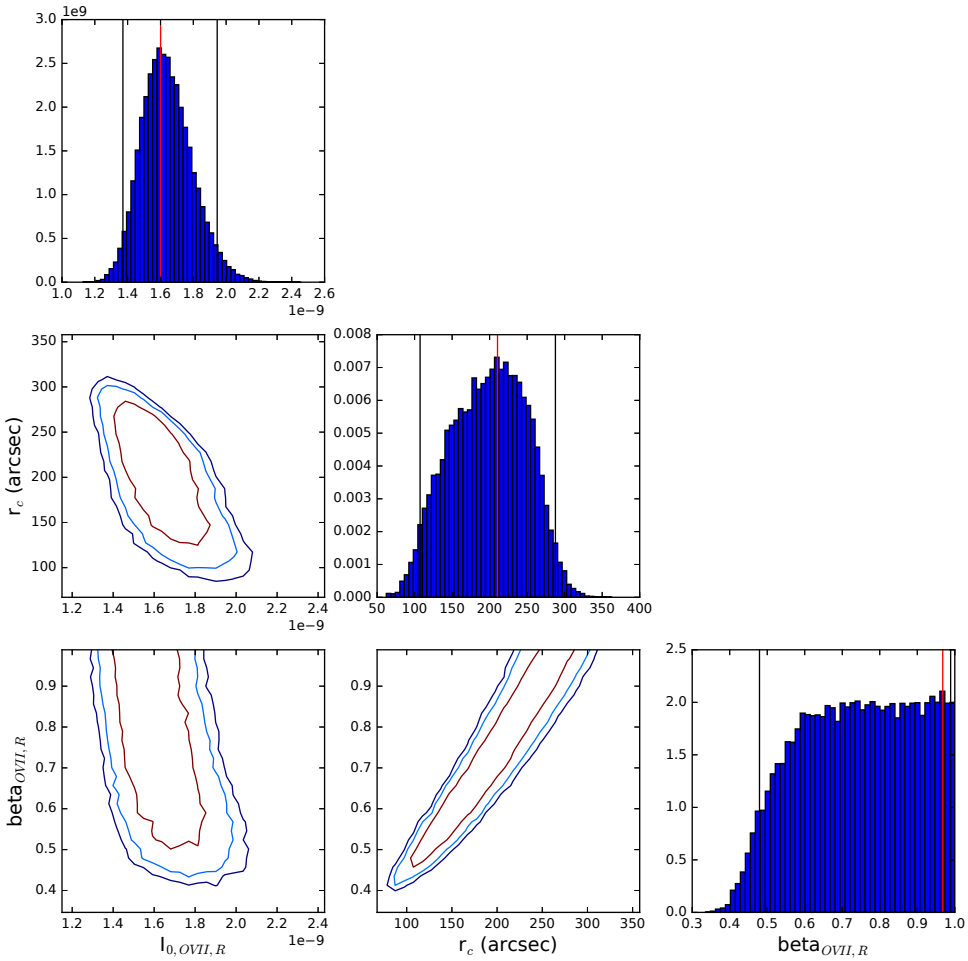

Figure 3.10. Marginalized histograms and parameter-parameter confidence plots for simulated OVIII emission. In the histograms, the best fit is shown by the solid red line, 95% confidence intervals by the black lines, and the true value by the dashed red line. In the contour plots, the red line shows the 67.5% confidence contour, the light blue line shows the 90% contour, and the dark blue line shows the 95% contour. The simulated values are shown by a red star.

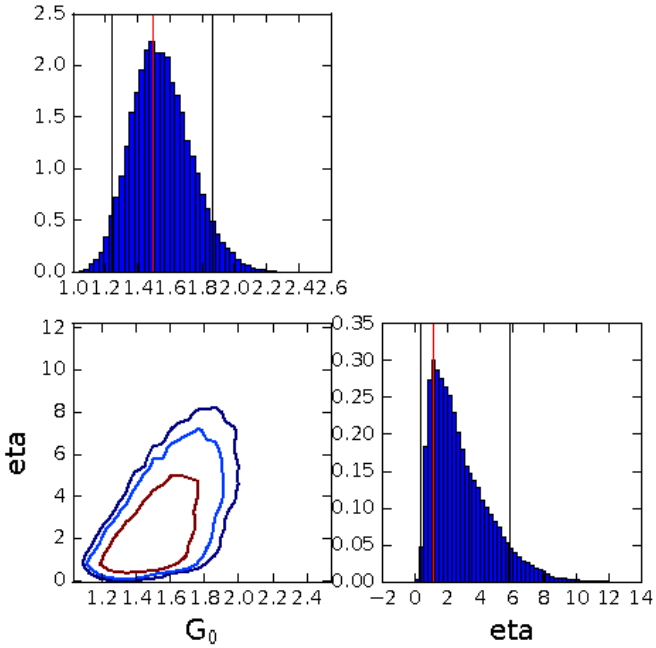

Figure 3.11. Same as Figure 3.10 but for different parameters.

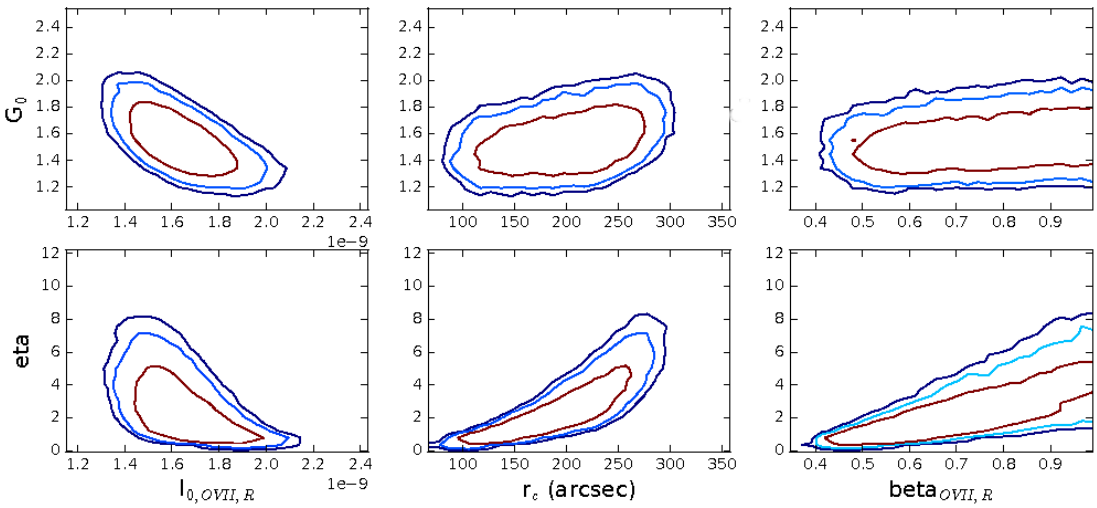

Figure 3.12. Same as Figure 3.10 but for different parameters.

ing the value of β. This leads to a radial G-ratio profile that may begin large at low radii, starts to decrease at r_c, and continues to decrease at larger radii such that it approaches zero at infinity.

To take full advantage of the data, we will jointly fit OVIII Lyα and the OVII Kα lines, linking r_c for all three fitting lines. Again, the contribution from the OVII intercombination line is modelled as 0.22 of the forbidden line. I_0 is left free for all three lines. If the OVII Kα resonance line suffers from scattering, the OVIII Lyα transition is likely to as well. Even though the oscillator strength of the OVII resonance line is ~ 4 times greater than the OVIII Lyα transition, the scattering probability also depends on the ionic fraction of the ions. For example, the ionic fraction of OVIII is greater than OVII for temperatures ~ 0.3 keV, compensating for its lower oscillator strength. Therefore, without losing generality, we leave β free for all three lines.

The fitting results are shown in Figures 3.13 - 3.15 and listed in Table 3.5. We can immediately see that simultaneous fitting has served to greatly constrain our parameters, all to within $\sim 20\%$. As expected under this paradigm, the OVII resonance line is much more extended than the OVII forbidden line, with the ratio $\beta_{OVII,R}/\beta_{OVII,F}$ = 0.55 (0.37, 0.79). The derived G-ratio at galaxy center is 1.41 (1.14, 1.79), in agreement with [77]. Within the image extraction region, the galaxy integrated G-ratio is 0.58 (0.39, 0.89), in agreement with the CIE expected value. As we would expect photons to be conserved over the entire source, this picture is in agreement with the resonance scattering scenario.

3.4 Discussion

Understanding the spatial distribution of X-ray emission lines provides a great deal of diagnostic power for elucidating the nuances of galactic feedback. Without the full spatio-spectral information, line degeneracies can become crippling to scientific progress. We have demonstrated a new approach for extracting spatial information of

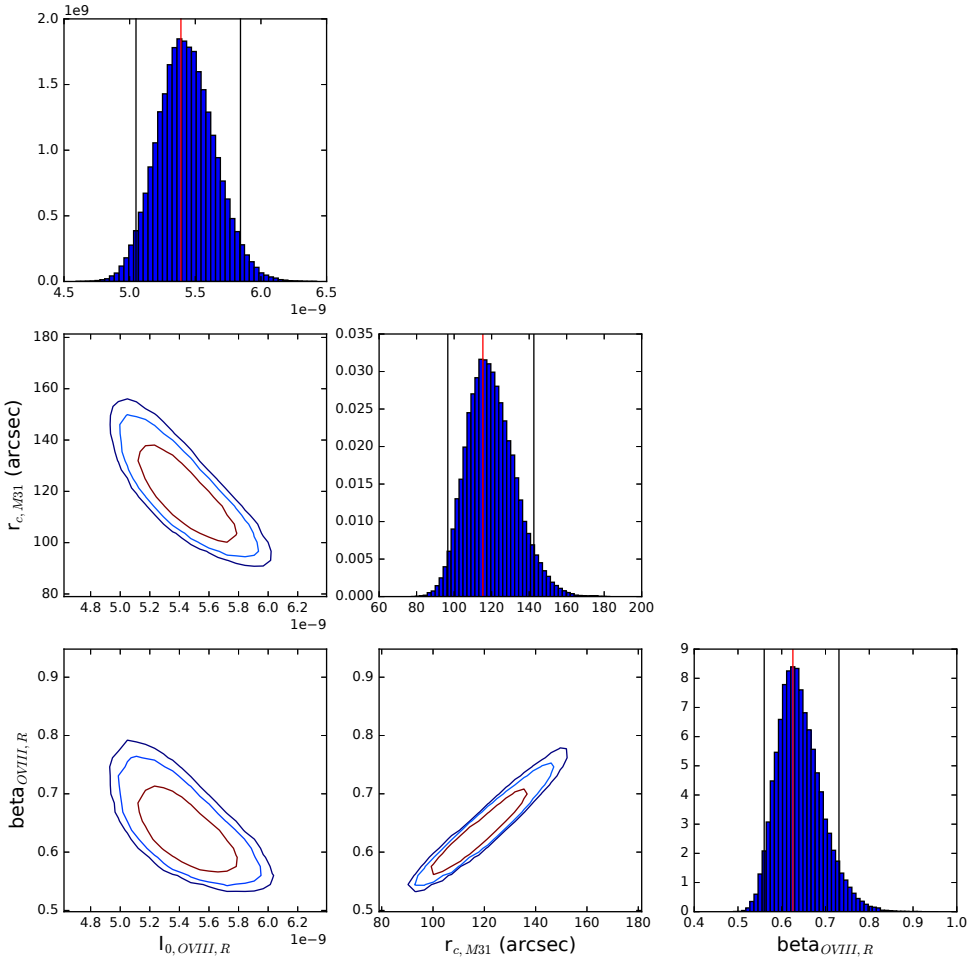

Figure 3.13. Same as Figure 3.10 but for different parameters.

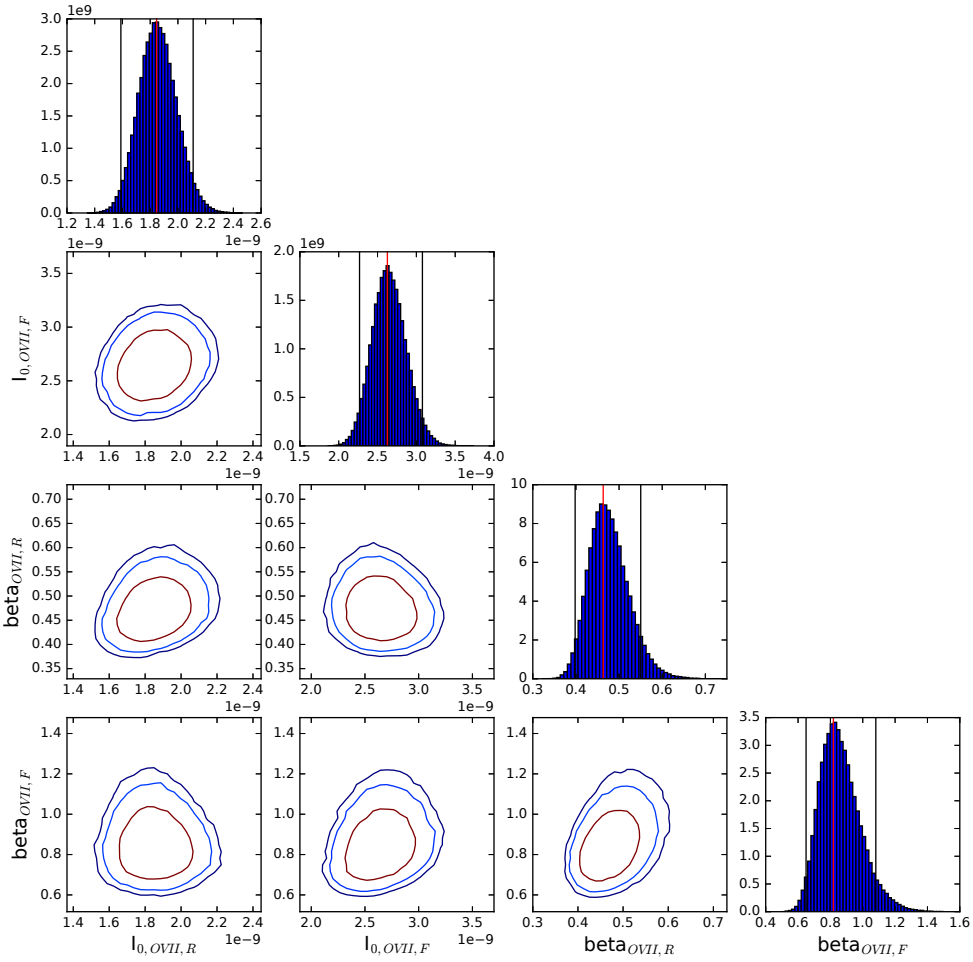

Figure 3.14. Same as Figure 3.10 but for different parameters.

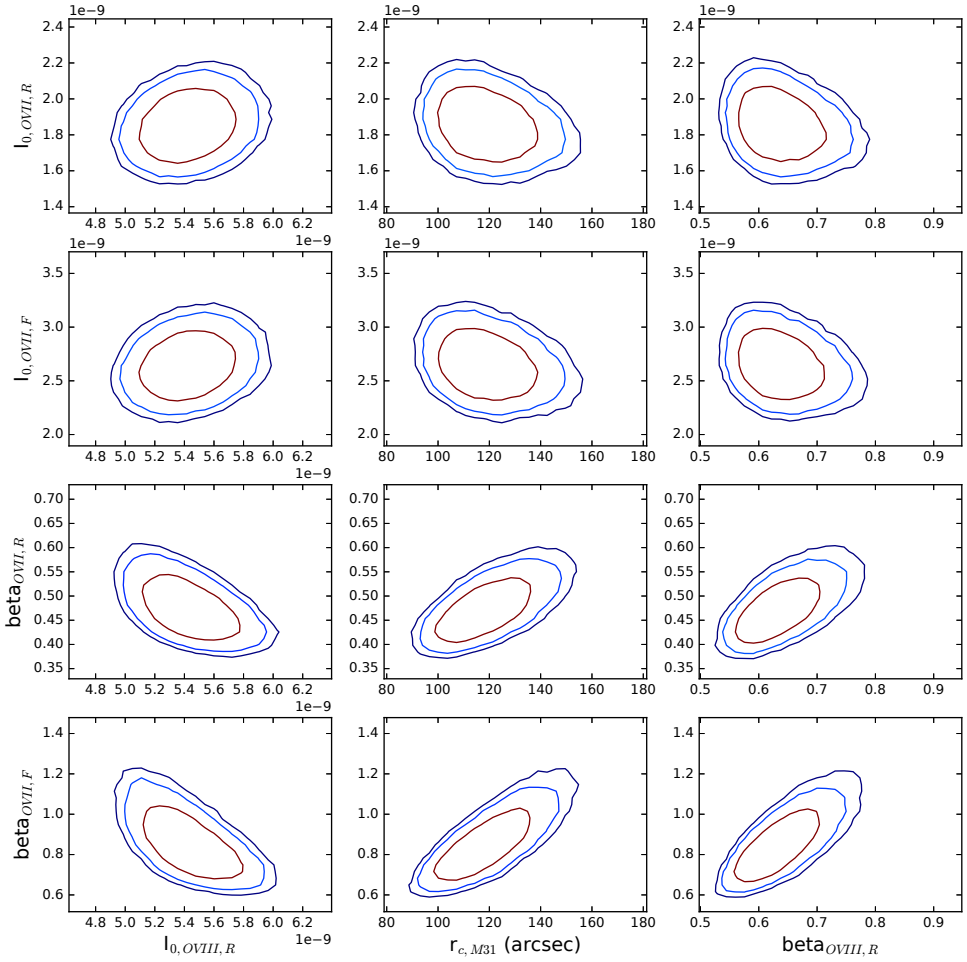

Figure 3.15. Same as Figure 3.10 but for different parameters.

Table 3.5. Joint fitting OVIII and OVII for M31, marginalized parameter best fit and 95% confidence intervals.

Parameter	Best	Lower 95% Limit	Upper 95% Limit
$I_{0,OVIII,R}$ (10^{-9} counts/s/cm^2/asec^2)	5.39	4.93	6.03
$I_{0,OVII,R}$ (10^{-9} counts/s/cm^2/asec^2)	1.85	1.55	2.18
$I_{0,OVII,F}$ (10^{-9} counts/s/cm^2/asec^2)	2.63	2.08	3.26
$r_{c,M31}$ (asec)	115	93	153
$\beta_{OVIII,R}$	0.62	0.53	0.79
$\beta_{OVII,R}$	0.46	0.37	0.62
$\beta_{OVII,F}$	0.82	0.62	1.25
Derived Parameters			
G_0	1.41	1.14	1.79
$G_{integrated}$	0.58	0.39	0.89

individual lines from a dispersive spectrometer using M31 observations with XMM-Newton's RGS instrument as an example. We have simulated the behaviour of the method under different physical conditions and find that physically meaningful results can be obtained for M31-like data when simultaneously fitting multiple lines. We also find that our results strongly support the need for including resonance scattering in the modelling of M31's bulge.

3.4.1 Plasma Conditions in M31 and Implications for Feedback

The inclusion of resonance scattering in the modelling of M31 will have important implications for estimates of the plasma conditions, most notably, for the results of [77]. These authors have performed the most robust analysis of M31's plasma conditions to date. In that work, the authors made estimates of the plasma temperature, iron abundance, O/Fe ratio, and discussed implications for Type Ia SNe feedback assuming the plasma is optically thin and in CIE. However, resonance scattering will have important effects on all of these estimates and implications.

We can directly estimate the temperature using the ratio of the OVIII and OVII resonance lines, after correcting for resonance scattering (but still assuming the plasma is isothermal and in CIE). This correction can be done by considering the

redistribution of photons through β, assuming the OVII Kα forbidden line defines the bulge's intrinsic spatial distribution and that total radiative flux is conserved. The core surface brightness of a line can be corrected for resonance scattering with the following:

$$\frac{I_{0,corr}}{I_{0,fit}} = \frac{\int r \left[1 + \left(\frac{r}{r_c}\right)^2\right]^{0.5-3\beta_{OVII,F}} \mathrm{d}r\mathrm{d}\theta}{\int r \left[1 + \left(\frac{r}{r_c}\right)^2\right]^{0.5-3\beta_{fit}} \mathrm{d}r\mathrm{d}\theta} \tag{3.10}$$

where $\mathrm{I}_{0,corr}$ is the corrected core surface brightness, $\mathrm{I}_{0,fit}$ is the core surface brightness obtained in the fit, β_{fit} is the β value of the fitted line, and $\beta_{OVII,F}$ is the β value of the OVII forbidden line for that particular sample.

Figure 3.16 shows the evolution of the OVIII/OVII resonance line ratio with temperature. Using the ratio of the central bulge, $I_{0,OVII,R}/I_{0,OVIII,R}$, the plasma temperature is 0.26 (0.234, 0.275) keV, consistent with [77]. These two resonance transitions are prominent in the M31 data, therefore it is not surprising that the temperature of the spectral fit in [77] is consistent, as it is likely primarily constrained through these transitions. However, after correcting for the scattering effect, we find the temperature to be 0.175 (0.164, 0.228) keV. This temperature is much closer to the stellar kinematic temperature of the bulge, 0.14 keV [67, 77], suggesting little additional heating from Type Ia SNe is required to explain the temperature of the plasma. This is further supported by the spatial distribution of the OVII forbidden line, where $\beta_{OVII,F} \sim 1$, suggesting very little heating of the ISM beyond that of dynamical.

While we can not directly estimate the Fe abundance with the results presented here, we can discuss the possible implications. Further, these implications resolve some of the discrepancies detailed in [77] and motivate additional study of M31 using the method outlined in this paper. The reduced temperature estimate based on the spatially-integrated OVIII/OVII resonance line ratio has immediate consequences for O/Fe, which was previously estimated as ~ 0.3, and the iron abundance, which was estimated as subsolar. In order to match the full RGS spectrum shown in [77], assum-

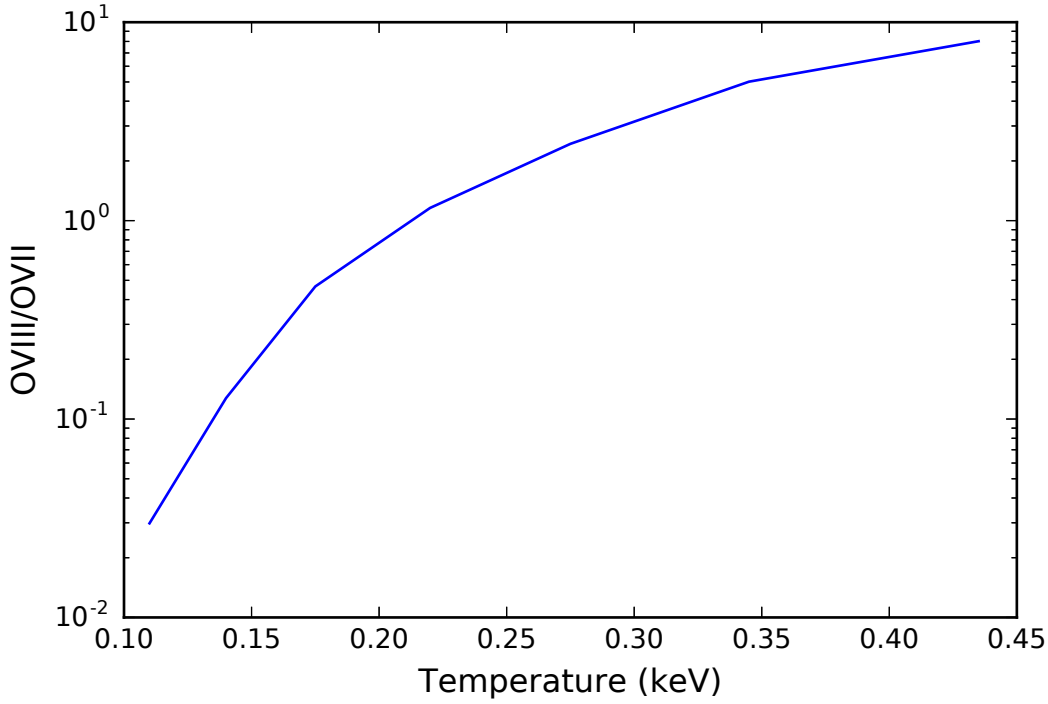

Figure 3.16. Ratio of OVIII Lyα to OVII Kα resonance line emissivity as a function of temperature.

ing a lower temperature as found here, we would expect the overall iron abundance to increase and O/Fe to decrease. This results from iron being primarily constrained through three transitions of Fe XVII at ~ 17Å[3] (of which the potential resonance scattering effect is yet to be investigated), while oxygen is primarily constrained through the OVIII Lyα and OVII Kα transitions modelled herein. This iron transition has a much higher peak temperature than the oxygen lines. Therefore, for a lower temperature plasma, we expect this transition's emissivity to be considerably reduced relative to the oxygen lines, requiring an increase in iron abundance to match the spectrum.

These changes in iron abundance and O/Fe serve to build a nearly unified model of the X-ray emission in M31's bulge. While fast outflows served to create a model that qualitatively matches the iron abundance found in [77], they also led to the expulsion of too much gas, under-predicting the X-ray luminosity by two orders of magnitude [124, 123]. Resonance scattering immediately requires any turbulent and outflow velocities to be very small, sustaining the hot gas reservoir required to match the observed luminosity. In doing so, it also necessitates that iron from Type Ia SNe fully mix with the surrounding hot gas. This leads to an expected iron abundance of up to 6 times the solar value [10]. This estimate is a far cry from that determined by spectral fitting in [77], where the authors found iron to be sub-solar. As discussed above, this discrepancy is naturally relieved when considering resonant scattering, at least qualitatively. However, a more detailed analysis of the iron distribution is required to test this theory more robustly, as well as quantify the velocity dispersion of the plasma.

By extension of this work, resonance scattering may further serve to explain the apparent decrease of the iron abundance at very small radii found for a number of spheroids when analyzing the O/Fe ratio as a function of radius (e.g., [45, 21, 22]),

[3]There is an additional strong Fe XVII transition at ~ 15Å, however, this line is deeply conflated by higher order transitions of OVIII and doesn't provide a great deal of diagnostic power.

an abundance decrease that does not exist when analyzing Mg/Fe (e.g., [55, 49, 80]). This peculiar behaviour has been found in galactic spheroids of nearly all sizes, many typically invoking buoyant, supersonic outflows driven by Type Ia SNe, which prevent Fe from mixing with the local ISM at low radii. Resonance scattering may address these abundance peculiarities through modulation of the temperature profile. These results suggest that much of the controversy over feedback from Type Ia SNe may have a much more mundane origin.

There is one outstanding issue with the interpretation detailed above. First, where does the SNe energy go? Estimates suggest that the energy released from Type Ia SNe in the bulge of M31 is $\sim 3-4$ times larger than that required to drive a galactic outflow [10]. Yet, for the resonance scattering scenario to be relevant, turbulent and outflow velocities must be low. Further, we show here that ISM heating from SNe, while existing, is not extensive. This may be reconciled if much of energy input from the SNe is radiatively lost from the system due to Fe's extremely high emissivity, as suggested by [16]. Another possibility is that collisions with dust grains serves to draw much of the energy out of the hot gas. If the X-ray observable Fe content of the inner bulge is still considerably lower than would be expected under full mixing after accounting for resonance scattering, it is more likely that the energy is lost through a subsonic outflow. This further necessitates a detailed study of the Fe lines, as well as a detailed accounting energy and mass budget.

There are two scenarios that we can't fully exclude as the source of the elevated G-ratio: CX and a young relic of a weak AGN burst. While the lack of significant cold gas in the bulge is highly suggestive, CX is incredibly efficient under the proper conditions. Its details are dependent on the surface area between any hot/cold gas interface and their relative velocities. Given the low turbulent velocity [67], necessity of any outflow velocity to be subsonic [77, 123], and low amount of cold gas/dust [33], we expect both the surface area and relative velocity between gas phases to

be low. However, without the counts to perform a meaningful spatial comparison between the G-ratio and cool gas distributions, it is difficult to absolutely rule out this scenario. Therefore, as CX modelling capabilities increase, it will be important to test its efficacy in the M31 bulge environment.

A young relic of a weak AGN event could also hypothetically lead to a less extended forbidden line. If the AGN luminosity is very weak, the radiative energy density will be too low to over-ionize the gas beyond the core radius. This leads to a forbidden line that is only elevated in the very inner regions. Yet, for a SMBH of the size that resides in M31, we expect the AGN to have a bolometric luminosity of $\sim 10^{43} - 10^{46}$ ergs/s during its high luminosity phase [135]. Assuming a luminosity of $\sim 10^{44}$ ergs/s, all of the gas in the bulge would be over-ionized immediately after the AGN "shuts off", leading a forbidden line that is much more extended than the resonance line [145]. Thus, the weak AGN burst scenario is also unlikely.

3.4.2 Methodological Limitations

The primary limiting factor to the study of diffuse gas with this method is the relative strength of the source emission. Even when viewing broadband emission, the X-ray regime is photon starved. When attempting to map an individual emission line in space, rather than fitting an entire spectrum, we are incredibly limited by the number of detected counts. Further, the only instruments currently capable of mapping individual emission lines, gratings, have a much lower effective area. This is because a great deal of the telescope's viewing power is lost during dispersion. Additionally, due to the dispersion through energy into the spatial detector coordinates, the bandpass is very limited for the RGS detector, which limits the power of multi-line modelling. Both of these issues conspire to make spatio-spectral X-ray analysis more difficult. However, to a large degree, proper modelling can serve to greatly overcome these issues.

The most useful approach to overcoming weak counting statistics is to parameterize the fit. This reduces the number of parameters from some factor of the number of spatial bins to several. Additionally, if parameterizing a fit, it is likely that flux limitations can also be greatly mitigated through the use of outside information (e.g., other lines or data) as demonstrated in Section 3.3. By linking spatial parameters between lines in a physically motivated way, one can greatly enhance their diagnostic power. This is particularly the case when linking blended lines with isolated lines. Even in the semiparametric case, certain lines are likely to correlate. Therefore, assuming the gas is approximately isothermal, one possible solution is to fit a single non-parametric 2D distribution and add an additional offset parameter, which is not spatially dependent, for each additional line that is expected to correlate with the first.

Another possibility is to link multiple lines through temperature and density as hyperparamters, causing the strength of the fit to increase with the addition of more lines. This strategy of course necessitates fitting under different emission paradigms as was done above. However, it is unclear to what extent certain emission mechanisms, particularly CX, alter resonance line ratios such as the OVIII/OVII used in this work. The effects depend not only on uncertain microphysical processes, but also on the macrophysical properties of the plasma (e.g., the relative velocity between cold and hot gas phases). Therefore, in practice, this approach is currently only feasible for truly CIE emission.

A final solution for alleviating weak counting statistics, the most naive, is to spend more time observing extended sources with the current fleet of dispersive spectrometers. Since the standard data reduction pipeline is designed for point sources, extended sources have not been given a large amount of grating observation time, with the exception of a few notable sources. However, with the methodology out-

lined above, we can tailor the use of dispersive X-ray spectrometers to tackle many challenging problems currently facing the hot regime of galactic feedback.

3.4.3 Methodological Potential

If given the observational time and computational resources, the methodology outlined above has a great deal to offer for understanding galactic feedback. This is true of both stellar (early and late time) and AGN feedback. Detailed spatio-spectral studies can lead to the best constraints to date on the plasma conditions, including temperature and metallicity, as well as information on the outflow mass and energetics. Further, all studies discussed below can be greatly enhanced with the incorporation of non-CIE emission models, all of which are on the brink of release if not recently released (e.g., the *atomdb* release of a CX model). While some of these models are still a bit primitive, they are a necessary step for understanding the hot component of galactic feedback.

3.4.3.1 Galactic Spheroids

Through careful analysis of the Fe XVII lines at ~ 17 Å, we may be able to place more direct constraints on Type Ia SNe in M31. It may also be possible to place constraints on the outflow velocity through quantification of Fe's ISM mixing. Further, simultaneous modelling of multiple Fe and O lines will allow us to discern whether the temperature is consistent between the two after correcting for resonance scattering. It they are not, the relic-AGN scenario may still be important for modelling the global spectrum, despite its unimportance for defining the spatial distribution of O.

We can further extend the pilot study presented herein to spheroids spanning a range of masses (Table 3.6). As we probe into larger spheroids, the effects of hidden or relic-AGN may become more prominent. Thus, by examining a range of masses, we may be able to disentangle the importance of AGN and late-time stellar feedback for the regulation of hot gas in bulges and elliptical galaxies. Additionally, we believe

it is possible to place constraints on recent AGN activity by examining the plasma over-ionization structure through a statistical sample of galaxies.

Table 3.6. Example Galactic Spheroid Sample and RGS observations

Galaxy	Type	D (Mpc)	$V_{\rm Helio}$	t(ks)/N_{ob}
NGC 0224 (M31)	SA(s)b bulge	0.72	-300	977/43
M86	E3	15.1	-244	86/1
NGC 3031 (M81)	SA(s)ab/LINER	3.6	-34	140/2
NGC 4382 (M85)	SAO(s)	18.5	729	205/5
NGC 4459	SA0(r)	15	1192	111/2
NGC 4638	S0	15.5	1152	105/4

Note: D and $V_{\rm Helio}$ are the galaxy distance and helio. radial velocity (obtained from NED), while N_{ob} and t represent the number of the observations within $2'$ of each galaxy's center and the total XMM-Newton exposure.

3.4.3.2 Active Star Forming Regions/Galaxies

Active star forming regions and galaxies provide insight into early-time stellar feedback (feedback related to young and massive stars). With this type of feedback, radiation pressure, stellar winds, and supernovae (SNe) combine to drive gas out of the galaxy. However, we have very little observational scope as to the galactic outflow's full multiphase energetics, chemical composition, and fate. For example, it remains unclear whether the diffuse soft X-ray emission observed around starburst galaxies is the superwind itself or just its interface with comingled cool gas clouds/filaments (e.g. [121, 4]). Unsurprisingly, temperature and abundance anomalies have been reported for starburst galaxies when the emission is modelled purely as a CIE plasma (e.g., [65]), suggesting the assumptions of optically-thin and CIE are not representative of reality.

The most useful candidate for the study of galactic winds generated by stellar feedback is the nuclear starburst galaxy M82. As previously demonstrated for the galaxy, the charge exchange (CX) contribution to line emission can be substantial (e.g., $\gtrsim 50\%$ of key He-like Kα triplets), which significantly affects the estimation of

the thermal and chemical properties of the hot plasma [76, 146]. That work, however, was based on only one RGS observation. With the available high-quality RGS data (12 observations amounting to $\sim$ 500 ks exist in the archive), it may be possible to spatially decompose the CXE and CIE contributions. Such an analysis has great potential for generating the best estimates to date of mass and chemical composition of the hot gas outflow and how it evolves.

It would also be useful to examine the spatial correlation of the CXE component, as traced by the OVII Kα forbidden line, with cool gas, as traced by Hα or dust emission. Such correlation may be leveraged in spatio-spectral studies of other starburst galaxies that lack the quality of data that M82 has. This may allow us to expand the case study of M82 and look at a statistically representative number of star forming galaxies (Table 3.7). With such a sample, one could investigate the dependence of the X-ray line emission on other galaxy properties (e.g., stellar mass density and specific star formation rate).

Table 3.7. Example Star-forming Galaxy Sample and RGS observations

Galaxy	Type	D (Mpc)	$V_{\rm Helio}$	t(ks)/N_{ob}
NGC 0253	SAB(s)c/Sbrst	3.2	243	340/9
NGC 2903	SAB(rs)bc	9.4	556	96/1
NGC 3034 (M82)	edge-on Sbrst	3.9	203	427/12
NGC 4631	edge-on SB(s)d	6.7	606	55/1
NGC 5236 (M83)	SAB(s)c/Sbrst	4.6	513	175/5
M51	SAbc/LINER	8.0	600	207/9
IC 342	SAB(rs)cd	3.3	31	202/6
Antennae	HII	22	1705	260/10

Note: D and $V_{\rm Helio}$ are the galaxy distance and helio. radial velocity (obtained from NED), while N_{ob} and t represent the number of the observations within $2'$ of each galaxy's center and the total XMM-Newton exposure.

It may even be possible to explore the exciting possibility of direct bulk and/or turbulent velocity measurements for the hot plasma in superwinds. So far, such velocity information is only available about the entrained cool gas, which is expected to be accelerated to lower velocities than the hot, metal-enriched, plasma (e.g., [121]).

The cool gas shows outflow velocities in the range of 200 - 1000 km s^{-1}, as measured in UV/optical emission and/or absorption lines (e.g.,[82]). But to truly understand the dynamics and ultimate fate of such outflows, we must directly measure the velocities of the hot plasma flows, which can alter both the centroids and widths of the X-ray emission lines. For example, a radial velocity of 10^3 km s^{-1} at a wavelength of 15.0 Å would correspond to a dispersion shift of $22''$, which can be measured with a RGS spectrum of good counting statistics.

We are particularly interested in systematic velocity structures (e.g., bipolar outflows from at least moderately inclined galaxies like M82). Depending on the counting statistics, such a velocity structure can be characterized in either 1-D or 2-D. For compact starburst regions with high-S/N RGS spectra (e.g., the M83 and M51 nuclear starburst regions), one can infer the total velocity dispersion from fitting individual emission lines (e.g., OVIII Lyα). Preliminary analysis shows that for a strong line with $S/N \gtrsim 10$, we can measure the velocity dispersion to a limit smaller than ~ 500 km s^{-1} and the line centroid to a significantly higher accuracy, although potential systematic uncertainties are yet to be carefully considered.

3.5 Summary

Teasing out X-ray emission mechanisms is the first step to unravelling the mysteries of the hot component of galactic feedback. Currently the only instruments truly capable of doing this are slit-less dispersive spectrometers. Unfortunately, by dispersing spectral details into the spatial coordinate, the data from these instruments suffer from information confusion. In this work, we demonstrate the methodology for spatially mapping individual emission lines, including blended lines. Assuming a parametric spatial model, the spatio-spectral degeneracy is easily broken due to the fact that different lines dominate the source emission on different sides in the dispersion direction. Further, with multiple observations at different roll angles, this

degeneracy can be broken in full generality, allowing for a semi-parametric sampling of the surface brightness (Appendix E).

Using M31 as an example, we show that it is possible to distinguish the physical reason for the elevated G-ratio at the center of the OVII Kα line. We find that the M31 bulge emission shows clear evidence for resonance scattering. By simultaneous fitting of OVIII Lyα and OVII Kα under this physical paradigm, we are able to place significant constraints on the emission distribution. Correcting for resonance scattering, we find that the temperature of the hot plasma in M31's bulge is 0.175 (0.164, 0.228) keV, considerably lower than previous estimates. These results suggest Type Ia SNe are much less important for heating of the ISM than previously presumed. Further, they qualitatively relieve tension between the estimated Fe abundance and predictions of ejecta mixing from Type Ia SNe. A significant expansion of the work detailed herein, particularly a focus on the spatial distribution of Fe, may provide considerable observational constraint for both stellar and SMBH feedback mechanisms.

CHAPTER 4

CONCLUDING REMARKS

We began this work with the intent of extracting new insights out of the existing data by looking at it from a unique perspective. We have largely accomplished this goal. In Chapter 2 we made the first observational estimate of the accretion flow circularization radius in our Galactic Center by performing a spatio-spectral fit with 2D hydrodynamic simulations. We were also able to self-consistently deconvolve the residual point-like emission and speculate as to its nature. In Chapter 3 we demonstrate the methodology for using the data from a grating spectrometer to extract spatial information for individual emission lines, including blended lines. Both pieces of work demonstrate the usefulness of spatio-spectral analysis with X-ray data. Further, both methods provide a framework of advanced statistical analysis for illuminating the hot component of galactic accretion and feedback.

4.1 Obfuscated Spectra: The Need for Modelling in More Than One Dimension

When performing a spectral analysis, the standard approach to X-ray astronomy is to simultaneously model the entire spectrum (which spans over an order of magnitude in wavelength space!). This is done because of the entangled nature of the model parameters through poor to moderate spectral resolution, typically. Unless model simplifications are made, a basic CIE model requires simultaneously fitting the absorption, electron temperature, emission measure, and individual metal abundances for approximately 10 elements. For emission that can be reasonably characterized as

optically-thin and CIE, we expect the results to be fairly reliable. Unfortunately, this is rarely the case (e.g., [107, 77, 146]). Further, for moderate resolution spectra it is nearly impossible to discern diagnostics that can be used to assess these assumptions. Therefore, with the standard approach, the model degeneracies often become irreducible, stymieing further scientific inquiry.

This spectral obfuscation was discussed in great detail in Chapter 3. In the absence of well developed spectral models for non-equilibrium emission mechanisms, such as CX and relic-AGN, and high spectral resolution, it becomes impossible to discern even a very basic statement of emission production. However, we point out that each of the physical paradigms can be disentangled by utilizing spatial information in conjunction with the spectral information. The risk of not doing so is highlighted in that Chapter. For the case of M31, where it appears resonance scattering is the primary cause of the elevated G-ratio, spectral obfuscation has led authors to attribute many of the spectral peculiarities to more trendy topics, such as CX due to stellar feedback (e.g., [77]) and relic-AGN (e.g., [145]).

Even when CIE is a reasonable characterization of the plasma, if we err in any assumptions of thermodynamic spatial structure, then we can expect to have misleading results. This was shown in Chapter 2 for the Galactic Center. In that Chapter it was shown that assumptions about the flow structure in [131] led to a mischaracterization of residual point-like emission. Further, it is seen that [141] mischaracterize the density profile of the Sgr A* accretion flow, likely due to 1-D simplifications of their spatial model. While we can, in painstaking detail, work to justify our assumptions, any deviation from reality will bias fitting results. Unfortunately, this bias may not necessarily be clearly understood for some time.

The best way forward is to remove as many assumptions as reasonable. For X-ray observed extended sources, we already have the necessary information by design. It exists in every piece of archival data and will exist in every future observation. The

fact that we simultaneously get both imaging and spectroscopic data from observations can be an incredible boon to the X-ray community. Spatio-spectral analysis provides a very natural way to reduce assumptions and build a much more self-consistent picture of the X-ray universe. This modelling can also be done in a much more rigorous manner than was done in Chapters 2 and 3. In principle, this modelling could be extended by creating a spectrum for each spatial bin, truly utilizing all spatial and spectral information obtained.

Admittedly, the usefulness of spatio-spectral analysis may be somewhat mitigated by the strategy hitherto for X-ray telescope production. On our journey to create an omniscience granting telescope, X-ray astronomers have successively built instruments that do one thing in particular extremely well. This is a natural evolution when trying to balance budgetary needs with scientific desires. For Chandra ACIS, it is unparalleled angular resolution. For XMM-Newton's RGS, it is unprecedented spectral resolution. These telescopes have served our needs as a scientific community very well in the past. However, there are very clear examples of when this strategy breaks down (enumerated throughout this work). As we push forward, the greatest modelling alleviation will be provided by a Renaissance telescope, such as the X-ray Surveyor, which will provide both exquisite spatial and spectral resolution simultaneously. As such, this instrument has the power to usher in a golden era of spatio-spectral analysis.

4.2 On the Pragmatism of Bayesian Inference

A conceptualization of Bayesian inference is that it provides a framework for updating our belief in some model in light of newly found data. Through the prior, it effectively provides a means for introducing subjectivity. Naturally, as scientists, we would like to believe our version of subjectivity is objective reality. However, each piece of prior research provides additional foundation to build upon. Different shades

arise as each of us may choose to interpret these past results differently. Further, we may have different degrees to which we place our confidence in a particular study. While this may sound strange, as if our results are shrouded in an obscurity only known to the inner depths of a modeller's mind, all of these assumptions, confidences (or lack there of), and interpretations are stated up front when you specify the priors.

The prior also provides a straightforward way to incorporate and propagate uncertainty through sampling parameters. For example, in Chapter 2, we included the inclination angle of the accretion flow in our fit. The data was far from the necessary quality to adequately constrain this parameter beyond our current belief, which was well defined by stellar dynamics. However, the inclusion of this parameter as a sampling parameter easily allowed us to propagate its uncertainty (through the prior) to other parameters. If parameters are at all correlated, this propagation is necessary to understand the true credibility of other parameters. There is no equivalent procedure when fitting data under the Frequentist paradigm. Either we would let the parameter roam free, which limits the modelling power of our data given our knowledge from other experiments, or we would likely fix it at the assumed canonical value, which would lead to overconfidence in other parameters and may indeed bias our results.

4.3 A Roadmap for Understanding the Hot Component of Galactic Feedback

True understanding of physics in astronomy is layered within the electromagnetic spectrum. Studying X-ray spectra is one of the best ways to explore galactic feedback events. Being the instruments with the highest spectral resolution, grating spectrometers provide the best opportunity to understand the details of the high-energy physics that drives much of galactic evolution. However, we have largely been limited to the study of point sources due to the inherent difficulty of studying resolved gas with a dispersive instrument. Unfortunately, spatially resolving the spectral nuances of this

diffuse gas is the only way to break emission mechanism degeneracy and illuminate the driving galactic evolutionary forces, currently.

The tools demonstrated herein to allow spatially resolved spectroscopic study with a grating system, and more generally, can deeply augment our understanding of hot gas in and around galaxies and the physical processes that govern it. First, they provide the ability to illuminate X-ray emission mechanisms. This allows one to derive the inherent plasma conditions. Only at this point can one begin discussing X-ray observations in the larger context of galactic feedback. One could potentially constrain the hitherto ambiguous, large-scale manifestations of the underlying physics, such as the radial evolution of galactic outflows or the decomposition between frequency and duration in the AGN duty cycle. These estimates will provide some of the first observational constraints to certain modes of both stellar and SMBH feedback, elucidating a path for subgrid modelling within cosmological simulations.

APPENDIX A

SGR A* GOODNESS OF FIT

Looking again at Figure 2.5, we see that there are no apparent residuals within the inner $\sim$1.", however, beyond this, there may be significant residual effects. It should be noted there are multiple contributions to the per pixel error that are not being modelled, including discrete X-ray sources, possible unmodelled extended structure, and time avaeraging of a chaotic simulation. To exactly what extent these lead to an underestimate of the error, it is difficult to quantify. However, we will point out why, all things considered, we believe we have obtained a reasonable fit.

Let us first consider the time averaging of the simulation, despite the actual simulation being quite chaotic and turbulent as the outflowing gas collides with the inflowing gas. Indeed, the temporal dispersion of a single grid cell can lead to a flux difference of a factor of two in either direction, probably leading to a slight underestimate of the size of our confidence intervals. How much effect this would have after smoothing is unclear, since individual grid cells are not independent, but have clear turbulent structure between themselves during the simulation. It is clear, though that at any particular point in time, the emission from a single point in space can deviate significantly. However, these deviations are the strongest at low radii, which contribute relatively little to the overall flux in the image, and would likely be smoothed out by not only the PSF, but also the emission from the outer parts of the flow.

Now, let us consider the effects that operate at larger radii. One such source of uncertainty in the residuals is the number statistical fluctuations of discrete X-ray sources. However, it is likely this term contributes negligibly to the emission and is

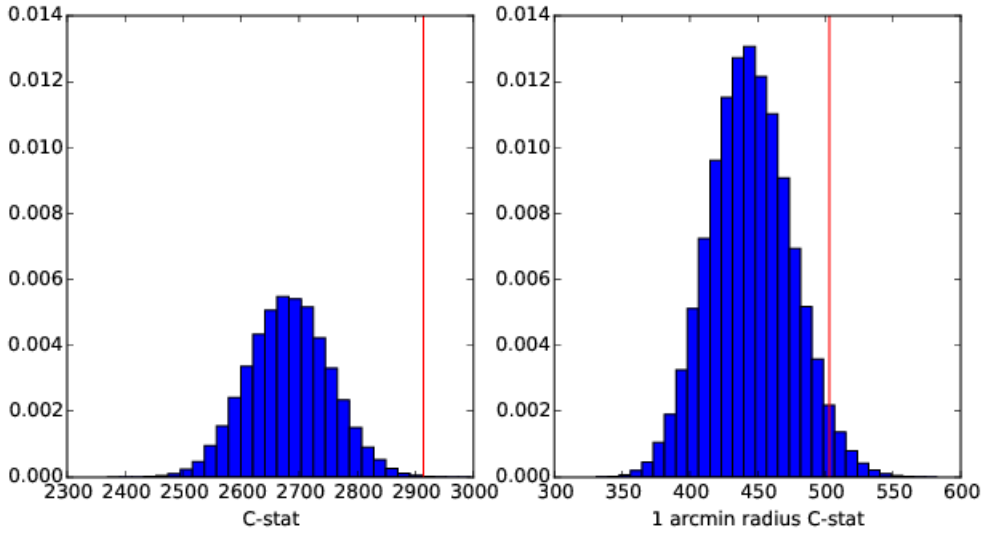

Figure A.1. Best fit C-statistic comparison to poisson fluctuations for the *free* model. The red line indicates the best fit model compared to the data while the distributions are random realizations of the model.

merely absorbed into the background component. More importantly, is unmodelled extended sub-structure that skirts the fitted region, such as dispersed emission and material from the G2 object, or the discreteness of the stellar winds and their colliding shocks. The apparent southeast excess, excluded from our fit, may represent an extreme case of such substructures. The presence of similar, probably fainter sub-substructure in the fitting region is echoed in the goodness of fit estimate. As we can see in Figure A.1, when excluding the pixels beyond 1", the fit becomes remarkably better; the formal statistical consistency increases from ∼0.1% to ∼2.6%. Further, and importantly, by performing several fits masking beyond different radii, we find the parameter results are not sensitive to the fitted region within the image, leading us to conclude that the component does not contaminate our parameter estimates.

APPENDIX B

REVISITING SGR A*'S SPECTRAL ENERGY DISTRIBUTION

Understanding the physical processes surrounding low luminosity active galactic nuclei (LL-AGN), weakly accreting and emitting supermassive black holes (SMBHs), is integral to understanding how their feedback affects the circumnuclear environment. The general picture of how the accretion flow evolves has begun to emerge in recent years for the LL-AGN in our galaxy, Sgr A*. As stellar winds spew forth from Sgr A*'s massive, circumnavigating stars, they collide with each other, shocking to X-ray emitting temperatures (e.g., [24]). This gas is captured by the SMBH at the center of Sgr A* and begins falling deeper into the potential well. With a substantial amount of coherent angular momentum, the gas is at least partially rotationally supported throughout, as shown in Chapter 2. As angular momentum is transported, the gas turbulently funnels inward. Some of this gas will accrete onto the BH, however, most of it will be driven away in a strong collimated polar outflow [142, 89, 70, 131, 139]. Yet, even with this general framework in place, some contradictions between studies of different wavebands need to be resolved before a truly unified model of the accretion flow structure of Sgr A* can be claimed.

One very important study for understanding the quiescent emission of the Sgr A* accretion flow, including the emission from very near the event horizon, was that of [141]. By studying the multi-wavelength spectral energy distribution (SED), these authors estimate the accretion rate onto the BH to be $\dot{M}_{BH} \approx 4 \times 10^{-8} \mathrm{M}_{\odot}/\mathrm{yr}$. The general picture of the [141] model is as follows. They show that the SED can be explained by electrons in a quasi-thermal distribution. The bulk of the electrons

are thermal, emitting strong synchrotron emission in the radio bands. Some of this thermal synchrotron emission is inverse-Compton scattered into the UV, with a high energy exponential tail extending into the X-rays. Based on their calculations, we expect this inverse-Compton emission to contribute anywhere from a few tenths of a percent to a percent of the X-ray emission, and, is naturally quite steep due to its thermal origin.

[141] also show that approximately $\leq 1.5\%$ of the electrons must be non-thermally accelerated to emit synchrotron in order to match the radio emission. Further, they show that the powerlaw index of the high energy synchrotron tail must be greater than or equal to 3.5. This scenario is consistent with the multi-wavelength spectral energy distribution spanning from radio through IR and to X-ray, including more recent estimates of the mean IR flux [112]. A powerlaw index of 3.5 places the synchrotron contribution to X-ray emission at roughly a few percent. Some of this non-thermal synchrotron emission is also inverse-Compton scattered to X-ray energies, contributing $\sim 10\%$ to the quiescent emission with approximately the same slope as the synchrotron emission. Taken in conjunction, the synchrotron and inverse-Compton emission contribute non-negligibly ($\sim 15-20\%$) to the observed X-ray flux, while the bulk of X-ray emission is due to the extended accretion flow. Unfortunately, at the time of this study no significant X-ray data existed for the authors to include more spatial and spectral information, which can provide direct constraints on the flow geometry.

Such a large non-thermal contribution to the X-ray emission is in direct conflict with the recent results of Chapter 2. These authors took advantage of the self-similar nature of radiative inefficient accretion flows (RIAFs)[70] to deconvolve the residual point-like emission (primarily synchrotron and inverse-Compton) from the spatially extended accretion flow. The authors do this by comparing three different band images of the combined quiescent *Chandra* data (the same data set as analyzed

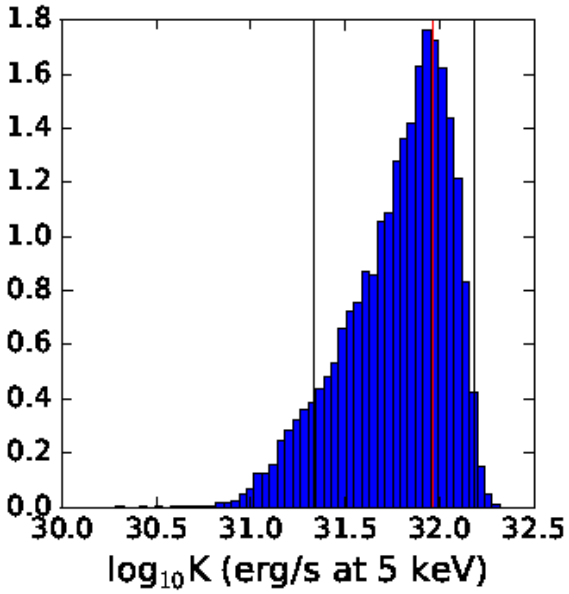

Figure B.1. The probability distribution of the point-like flux (egs/s) at 5 keV.

in [131]) directly to simulations of black hole accretion via the power of Markov Chain Monte Carlo (MCMC) sampling. They find that the point-like component has a specific luminosity of $\log_{10}\nu L_\nu \sim 31.96$ (31.32, 32.18) ergs/s at 5 keV, and is responsible for 4.2% (2.3, 7.0) of the observed emission within 1.5" in the 1-9 keV band with *Chandra* (see Figure B.1). The authors also find that the point-like emission can be well characterized by a single powerlaw, with $\alpha \sim 4.8$ (3.5, 7.5; 90% confidence interval). This steepness suggests the emission is primarily due to some combination of inverse-Compton and a steep synchrotron powerlaw, qualitatively in agreement with [141]. However, the lower flux contribution needs to be reconciled.

A second major, and more prominent, difference between the work of [141] and Chapter 2 is their radial density profiles. Consistent with other recent estimates from X-ray spectral fitting [131], we find that the density profile must be very flat due to the presence of a strong outflow ($s \sim 1$, where $n(r) \propto r^{-3/2+s}$; Figure B.2). In contrast, [141] find that $s \sim 0.3$. They found that this slope was able to simultaneously characterize both the X-ray and sub-mm emission. With all other parameters fixed,

an increase in s would lead to a significant reduction in sub-mm emission for the model of [141]. Therefore, it is unclear to what extent this difference can be reconciled within the uncertainty of other parameters.

In light of these recent results from X-ray fitting, the RIAF model of [141] needs to be updated to consider these new, direct constraints to the density profile and non-thermal contribution (synchrotron and inverse-Compton) of the quiescent X-ray emission. We will herein do this by performing a model comparison in the same way as in [141], while including the constraint on the flux within 400 r_s. While the present state of the code does not provide a straightfoward approach to including constraints on the density profile or X-ray spectral slope of the inner accretion flow, this update will be an important test for creating a fully unified model of the emission from Sgr A*.

B.1 Methods

We examine the emergent spectral energy distribution (SED) of Sgr A* in light of new constraints on the accretion flow. Data spanning much of the SED is used, including: radio [43, 147], IR [115, 53], and X-ray [2]. As in [141], we assume that a fraction η of the energy in thermal electrons is injected into the nonthermal particles (i.e., power-law electrons) with the power-law index p. Other tunable parameters include the mass accretion rate at the outer boundary, $\dot{M}_{out}$, and mass accretion profile slope, s, where $\dot{M}_r = \dot{M}_{out}(r/r_{out})^s$. Fixed parameters include $\beta = 0.1$ (defined as the ratio of the magnetic pressure $p_{\rm mag}$ and the gas pressure $p_{\rm gas}$, $\beta \equiv p_{\rm mag}/p_{\rm gas}$; e.g., [27, 28, 3]), the fraction of the turbulent dissipation that directly heats the electrons $\delta = 0.3$ (e.g. [9, 99, 100, 68, 54]), and the viscosity parameter $\alpha = 0.1$ (e.g., [48]).

For an exhaustive treatment of the fitting procedure, we refer the reader to [141]. However, in short, the fitting procedure is as follows. First, we calculate the one-dimensional dynamics of the RIAF (or ADAF) by solving for conservation of mass,

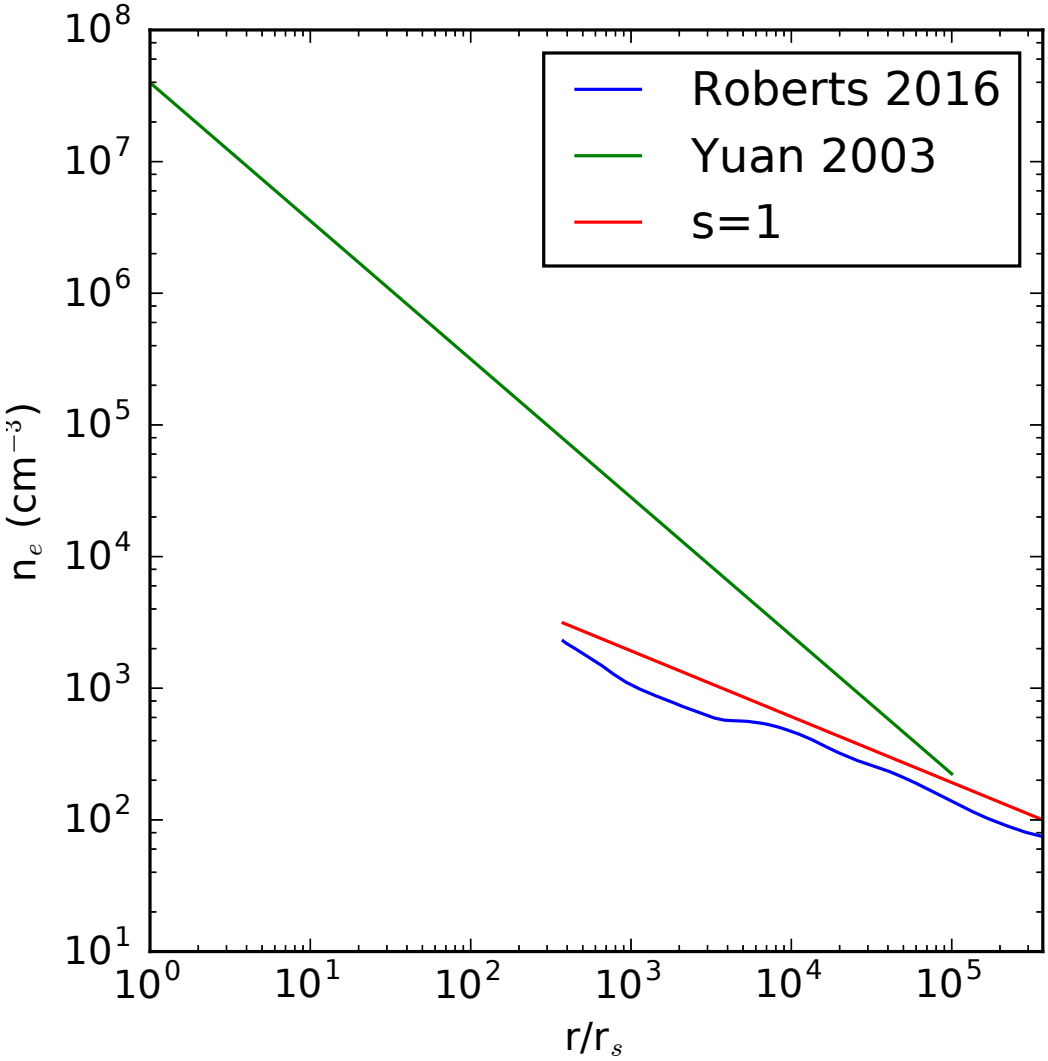

Figure B.2. The electron density as a function of radius. Green is the profile assumed by [141]. The blue profile shows the best fit azimuthally averaged profile found in Chapter 2. Some things to note: The Roberts profile is much shallower than that of Yuan. Another thing is the outer boundary of the flow is assumed to be much different.

radial momentum, angular momentum, electron, and ion energy equations (Equations 1-5 in [141])[1]. The outer boundary conditions of these equation, i.e., the electron/ion temperature and mass accretion rate, are constrained by observational results [2, 131]. We adjust the specific angular momentum of the flow at the horizon j_0 to obtain the global solutions of the hot accretion flow. The radiation from the RIAF can then be calculated by taking into account the synchrotron, bremsstrahlung of the thermal electrons, synchrotron of the nonthermal electrons in the accretion flow and their Comptonization ([141], and references therein). As we need to fit the point-like component inside ≤ 400 r_s of the accretion flow inferred from X-ray observations, we further decompose the radiation from the RIAF spatially to obtain their contribution in different regions. The spatially decomposed emission (≤ 400 r_s) can then be used to compare with the residual point-like component in X-ray band [106].

B.2 Results

A well fit model to the SED of Sgr A* is shown in Figure B.3, with the parameters listed in Table B.1. Note that bremsstrahlung radiation has been omitted from the Figure, as it contributes negligibly to the emission in the inner accretion flow, r ≤ 400 r_s. We can see that the residual point-like component in X-ray band is well accounted for by non-thermal synchrotron emission in the region of r < 400 r_s. The spectrum slope determined by the synchrotron emission after taking into account the synchrotron cooling is $\alpha \approx (p+1-3)/2 = 0.8$ ($\nu L_\nu \propto \nu^{-\alpha}$), corresponding to a photon index of 2.8. This photon index is at the limits of what is reasonable in the context of Chapter 2. The accretion rate at 10^3 r_s is 4.0×10^{-7} $M_\odot$ yr^{-1}, roughly consistent with

[1]It should be that the equations solved here are not fully consistent since they do not account for any energy or angular momentum that is lost in an outflow. However, an outflow primarily manifests itself through a flattening of the density profile, which we allow for (e.g., [136]). Any additional uncertainties from modification of the temperature structure, for example, we expect to be absorbed into the deeply uncertain heating parameter, δ.

Table B.1. Model parameters and fitted results from the SED fitting. $\dot{M}_{\rm out}$ is the mass accretion rate at $\sim 10^5$ r_s, $\dot{M}_{1000}$ is the accretion rate interpolated to 10^3 r_s. $L_{\rm 5keV}(400\ r_s)$ is the fitted 5 keV luminosity from the region < 400 r_s of the accretion flow.

Model	This Work	Yuan03
$\dot{M}_{\rm out}$ ($M_\odot$ yr^{-1})	1.8×10^{-6}	10^{-6}
s	0.33	0.27
η (%)	0.9	1.5
p	3.5	3.5
$\dot{M}_{1000}$ ($M_\odot$ yr^{-1})	4.0×10^{-7}	N/A
$\log[L_{\rm 5keV}(400 r_s)]$	31.95	N/A

the value of $\sim 1.0 \times 10^{-6}$ $M_\odot$ yr^{-1} determined in Chapter 2. However, the outflow parameter, $s = 0.33$, which is much smaller than the value ($s \sim 1.0$) inferred from the He-like Fe Kα line fitting [131] and X-ray image fitting (Chapter 2).

B.3 Discussion

The accretion flow model has been adjusted in several ways to better accomodate the new data point and inferences from Chapter 2. In order to capture the new constraint on residual point-like emission, it is sufficient to decrease the non-thermal particle fraction. Further, given the results of [131] and Chapter 2, we have also attempted to increase the steepness of the mass accretion profile. In order to maintain the sub-mm bump, this requires an increase in the mass accretion rate at the outer boundary. However, too drastic an increase leads to an overprediction of the total X-ray luminosity, which is primarily generated in the outer accretion flow. Thus, there is considerable tension between this model and the work in Chapter 2 for balancing the emission of the sub-mm bump and that of the X-ray. Yet, there are some model differences that help explain the results, which, when reconciled, may create a fully unified model.

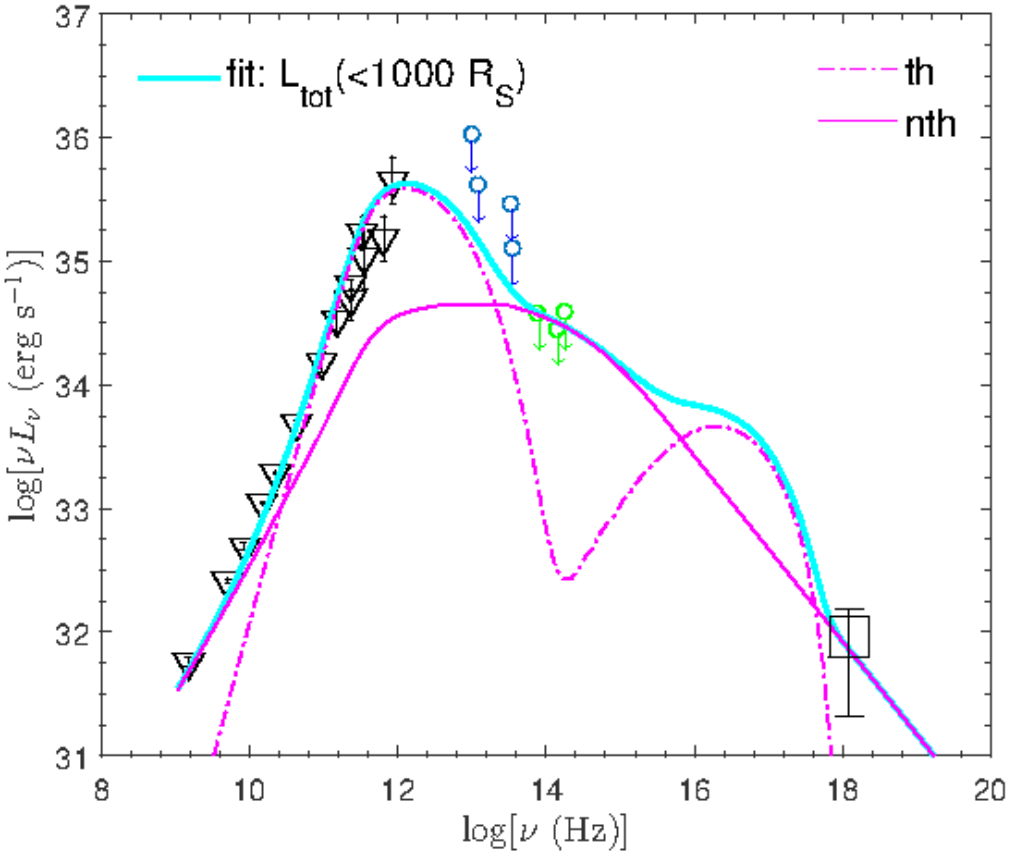

Figure B.3. The SED model of Sgr A*. The quiescent SED of Sgr A* are mainly adopted from [140] and references therein. The 5 keV X-ray data point (black square with error bar) is from Chapter 2. The dot-dashed pink line denotes the synchrotron and Comptonization from the thermal electrons in the hot accretion flow within 10^3 r_s, the thin solid pink line denotes the nonthermal synchrotron component from the same region of the accretion flow. The sum of the two components is denoted by the thick solid green line.

B.3.1 Reconciling Model Differences

We believe this difference could be reconciled by a more appropriate treatment of the multidimensional flow structure. In fact, it may be sufficient to simply allow certain parameters to vary with radius. For example, in [141], the authors note that if the turbulent electron heating, δ, were to be stronger in the inner accretion flow ($\mathrm{r} \leq 10\ \mathrm{r}_s$), the data would be consistent with with a larger value of s. Another key parameter that may need to be revised is the ratio of magnetic to thermal pressure, β. This parameter is held constant at 0.1 for all radii and azimuthal angles. However, from the GRMHD simulations of [3], this value appears to increase at low radii ($\mathrm{r} \leq 10\ \mathrm{r}_s$).

It is also possible that there is a physical change in the density profile at low radii. The results of [131] and [106] are only sensitive to the outer accretion flow ($r > 10^3 r_s$). A model in which the density profile is shallow at large radii and becomes steeper somewhere near the inner $100 r_s$ may naturally be able to accomodate the large synchrotron flux at sub-mm wavelengths without significantly affecting the X-ray flux. Detailed 3D magnetohydrodynamical (MHD) simulations show a transition at very low radii [142]. These simulations show that for $r \leq 10\ \mathrm{r}_s$, $s \sim 0$. However, the density profile does not rise with the flattening of the $\dot{M}_r$. Instead, the flattening is due to the assymptotic approach of the radial velocity toward the speed of light. Therefore, it is unclear why/how such a transition in the density profile would/could occur at radii of $\sim$ few $\times 10^2\ \mathrm{r}_s$.

Another prominent issue that needs to be addressed is the estimation of the quiescent emission itself. Separating the X-ray flares from the quiescent emission is perhaps the easiest, as these flares are the strongest, increasing the flux by up to 100x the quiescent rate. These flares are alos extremely narrow temporally. However, at longer wavelengths, these flares broaden out to the point that the mm emission fluctuates by only a factor of a few and it becomes difficult to define the quiescent state due to their

temporal broadness [46]. Since these data points in the SED were estimated through the mean flux, it is possible that the true Quiescent flux is a factor of a few lower in the mm and sub-mm. A lower sub-mm and mm flux would naturally be compensated by a decrease in density at low radii through a stronger outflow solution. However, with all other parameters fixed, an increase in s from 0.3 to ≈ 1 would result in a decrease of the sub-mm flux by multiple orders of magnitude. Therefore, it is unclear to what extent a more accurate estimate of the quiescent sub-mm emission would add to model reconciliation. Nevertheless, it is an issue that needs to be addressed.

One final issue that should be mentioned is the fitting procedure itself. With the current code setup, it is difficult to robustly explore parameter space. Therefore, it is unclear if we are in a local minima of parameter space. In priciple, this procedure could be updated to sample under the Bayesian framework. Such would be a natural next step to robustly contrain the model parameters detailed above. Further, it provides a straightforward way to include constraint on the point-like residual slope and the mass accretion profile from Chapter 2 through the use of priors.

B.3.2 On the Origin of a Steep Synchrotron Slope

The steep powerlaw slope found above and by [141] is considerably different than the flare emission analyzed by [131]. Further, [131] found that the slope of the flare emission is insensitive to the strength of the flare. Unless there is a state change below the flare detection limit, this difference in synchrotron powerlaw slope between the quiescent and flare emission implies a different origin of the particle acceleration. We speculate that this difference can be physically understood within the context of recent theoretical works.

[66] explore how different mechanisms of particle acceleration affect the energy of particles. Specifically, they show how the energy of a particle increases as a function of time with respect to the acceleration process. For the fiducial flare particle

acceleration mechanism, magnetic reconnection, particles are efficiently accelerated ($E \propto t^{1.43}$). Contrastingly, when reconnection isn't important and turbulence drives particle acceleration through a second order Fermi process where $E \propto t^{0.66}$. To first order, this decreased efficiency appears to naturally result in a spectrum of powerlaw index ~ 3.5 when considering the powerlaw index of flare emission (~ 2.6), which would be in broad agreement with the results of [141] and detailed in Chapter 2.

In the near future, it may be possible to directly test the quiescent slope against theoretical predictions of turbulence driven particle acceleration. Recent work by [148] studying relativistic plasma shows that turbulence can accelerate electrons into a powerlaw spectrum. Further, this work provides a fitting formula for how the powerlaw index evolves with magnetization and system size. They show that a non-thermal powerlaw particle energy distribution, $N(E) \sim E^{-\delta}$, with $\delta \sim 1 + C(L/B)^{0.5}$, where C is a constant, B is the magnetic field strength, and L represents the system size. However, they note that it is unclear how efficient particle acceleration from turbulence would be in the context of a SMBH accretion flow due to the system size. Yet, as in the case of magnetic reconnection (e.g. [119, 47]), it is possible that particle acceleration due to turbulence becomes scale free for asymptotically large systems.

B.4 Summary and Conclusions

We have revisited the SED of Sgr A* in the context of recent results from [131] and Chapter 2. These works suggest that the mass accretion profile is much steeper than previously assumed based on analysis of the SED [141]. Further, In Chapter 2 we place constraints on the X-ray emission from the inner accretion, both its' flux and slope. We have attempted to reconcile model differences between the 1D RIAF used to fit SED and the 2D simulations used to fit the spatio-spectral properties of the X-ray emission with limited success. While both models agree on the steepness of non-thermal synchrotron emission, it remains difficult to reconcile their differences in

the density profile. We further discuss the origin of this steep non-thermal emission, as well as a possible path forward for model reconciliation. Specifically, we find:

- The added constraint on residual point-like emission from Chapter 2 can be reconciled through minor modification of the original work of [141].
- A more robust fitting procedure is necessary to include new constraints on the density profile and X-ray spectral index, and to explore the parameter space in a more statistically rich way.
- For a simple 1D RIAF model, it is difficult to simultaneously model the X-ray emission and sub-mm bump when considering a strong outflow solution.
- Multidimensional modelling of the accretion flow is likely necessary to reconcile the prior point. Other possbile important issues exist, including: estimation accuracy of the quiescent sub-mm and mm fluxes and a possible steepening of the density profile at low radii.
- The steep spectral index of the synchrotron emission is suggestive that it is accelerated through magnetic turbulence, a second order Fermi process, rather than magnetic reconnection, a first order Fermi process.

APPENDIX C

MARGINALIZED HISTOGRAMS AND PAR.-PAR. CONFIDENCE PLOTS FOR THE SGR A* FIT

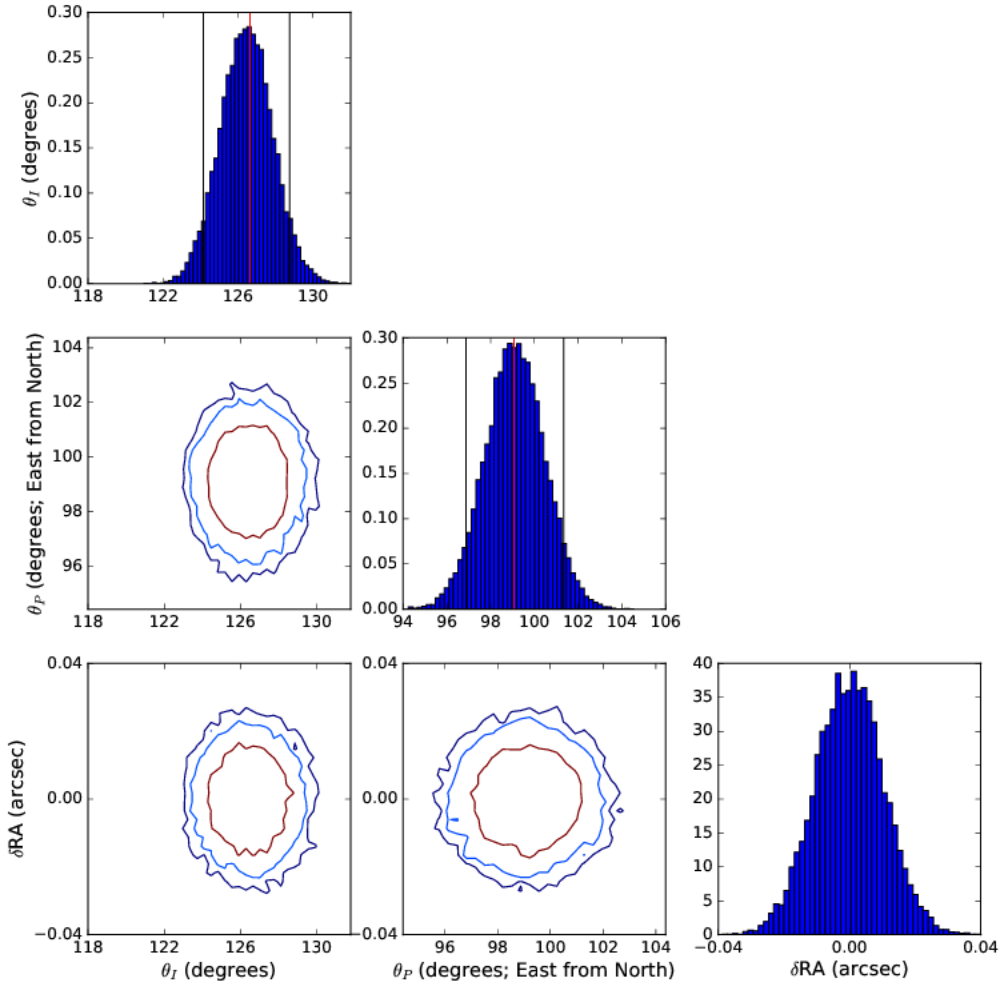

Figure C.1. Marginalized parameter histograms and parameter-parameter confidence intervals.

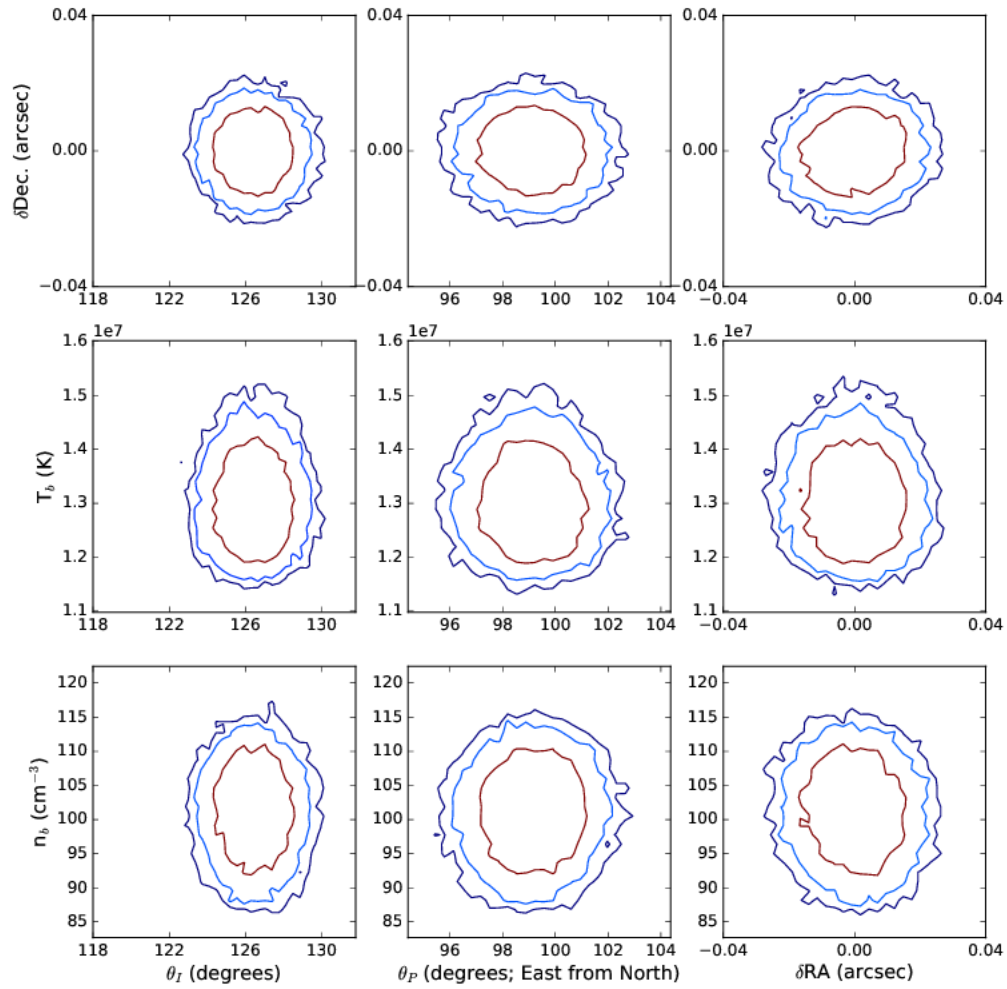

Figure C.2. Marginalized parameter histograms and parameter-parameter confidence intervals.

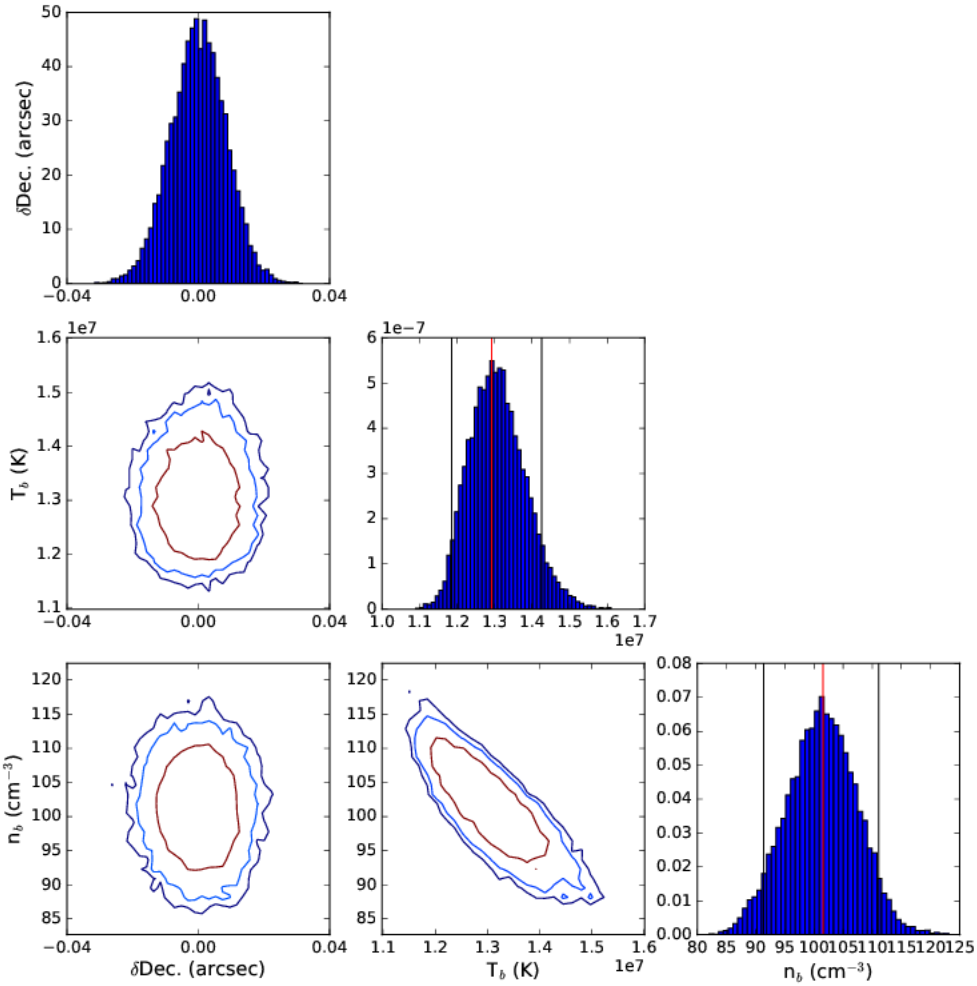

Figure C.3. Marginalized parameter histograms and parameter-parameter confidence intervals.

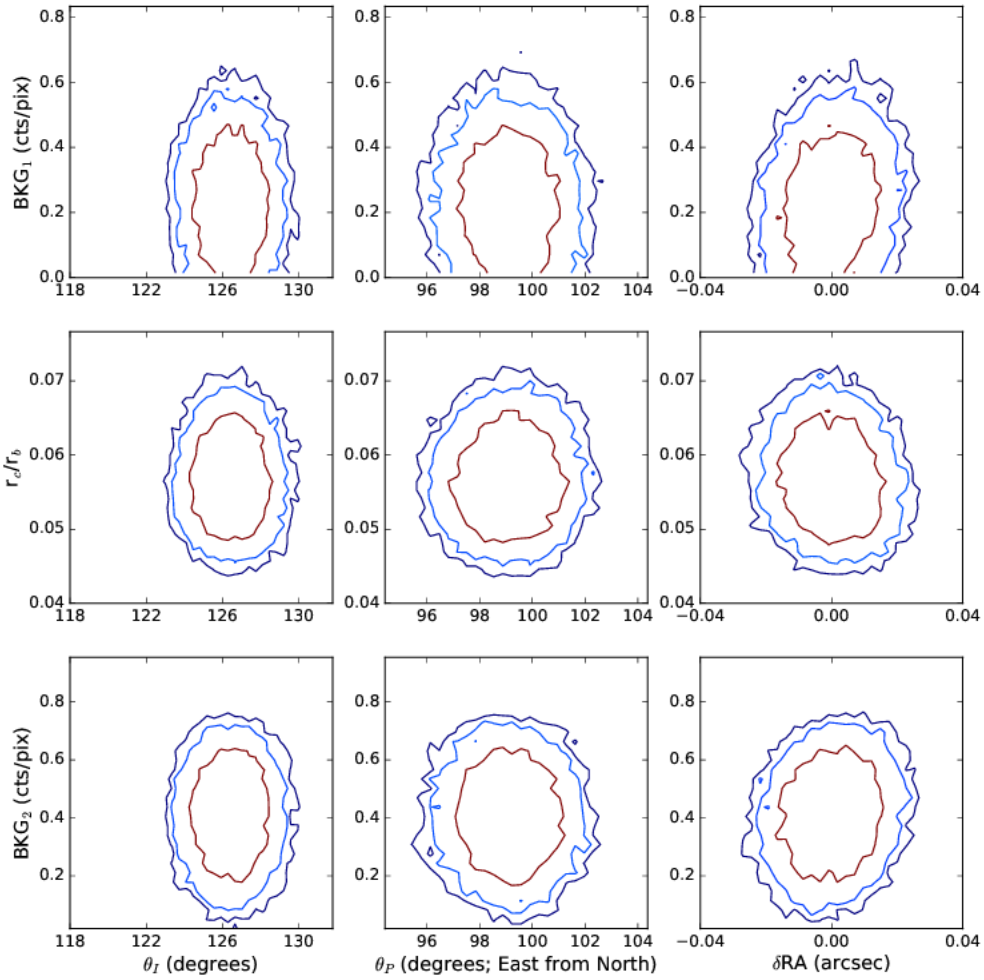

Figure C.4. Marginalized parameter histograms and parameter-parameter confidence intervals.

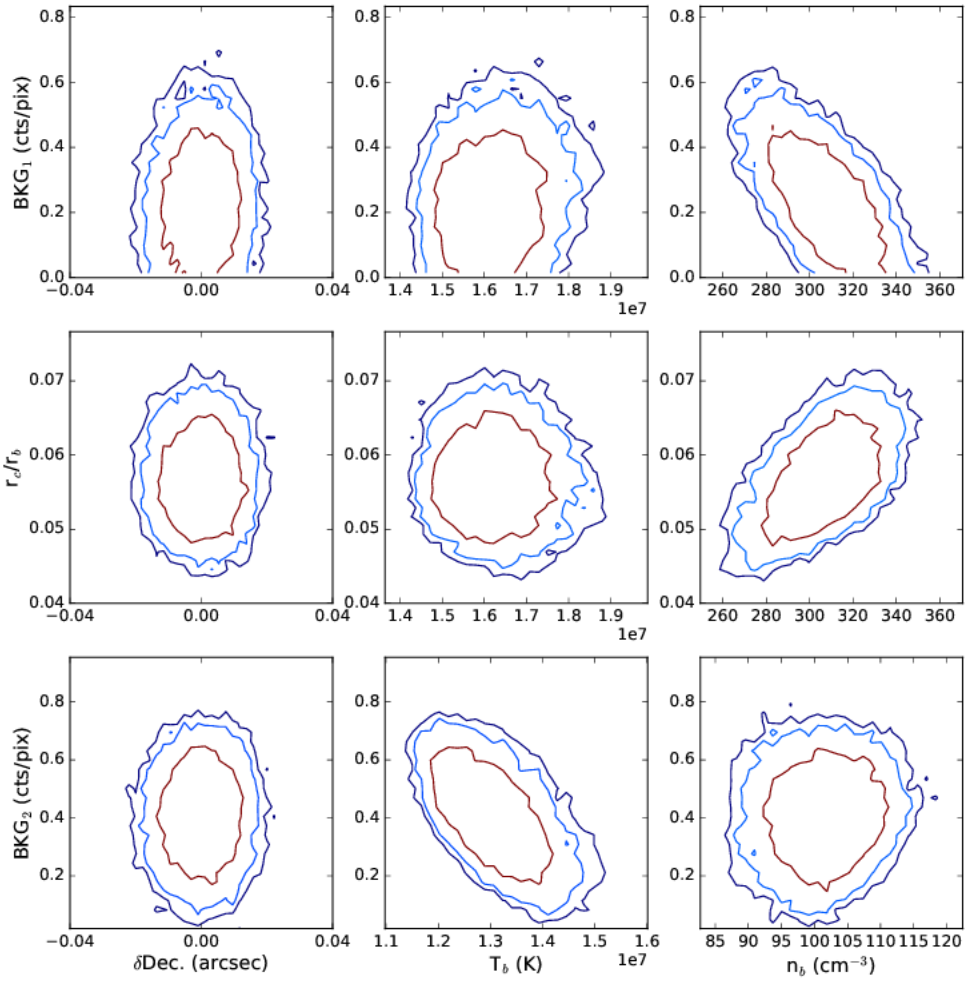

Figure C.5. Marginalized parameter histograms and parameter-parameter confidence intervals.

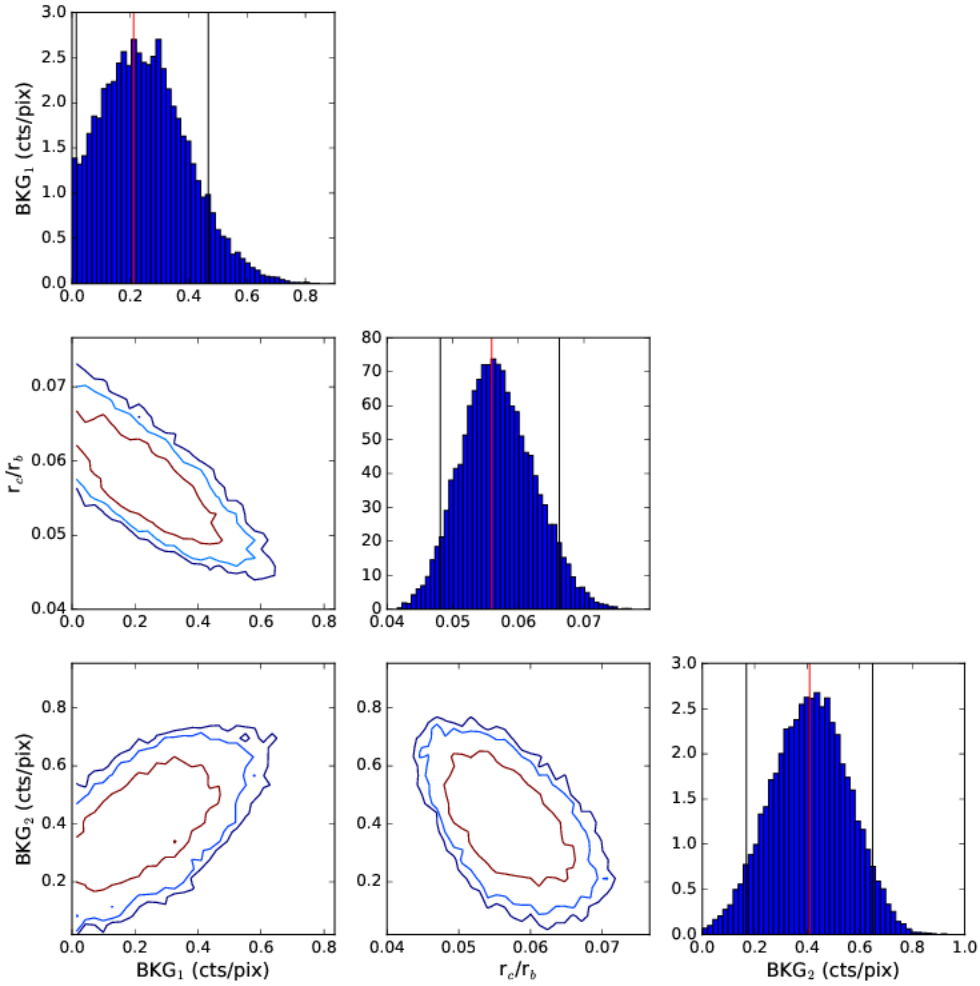

Figure C.6. Marginalized parameter histograms and parameter-parameter confidence intervals.

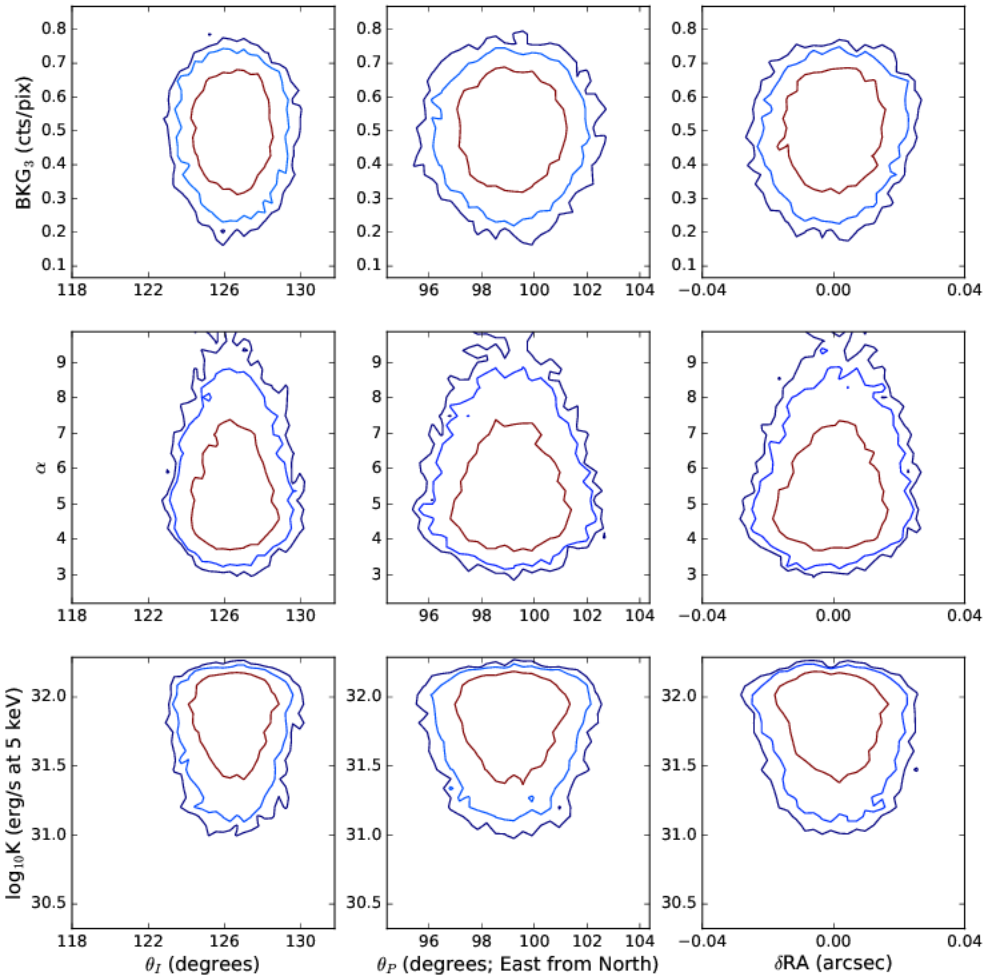

Figure C.7. Marginalized parameter histograms and parameter-parameter confidence intervals.

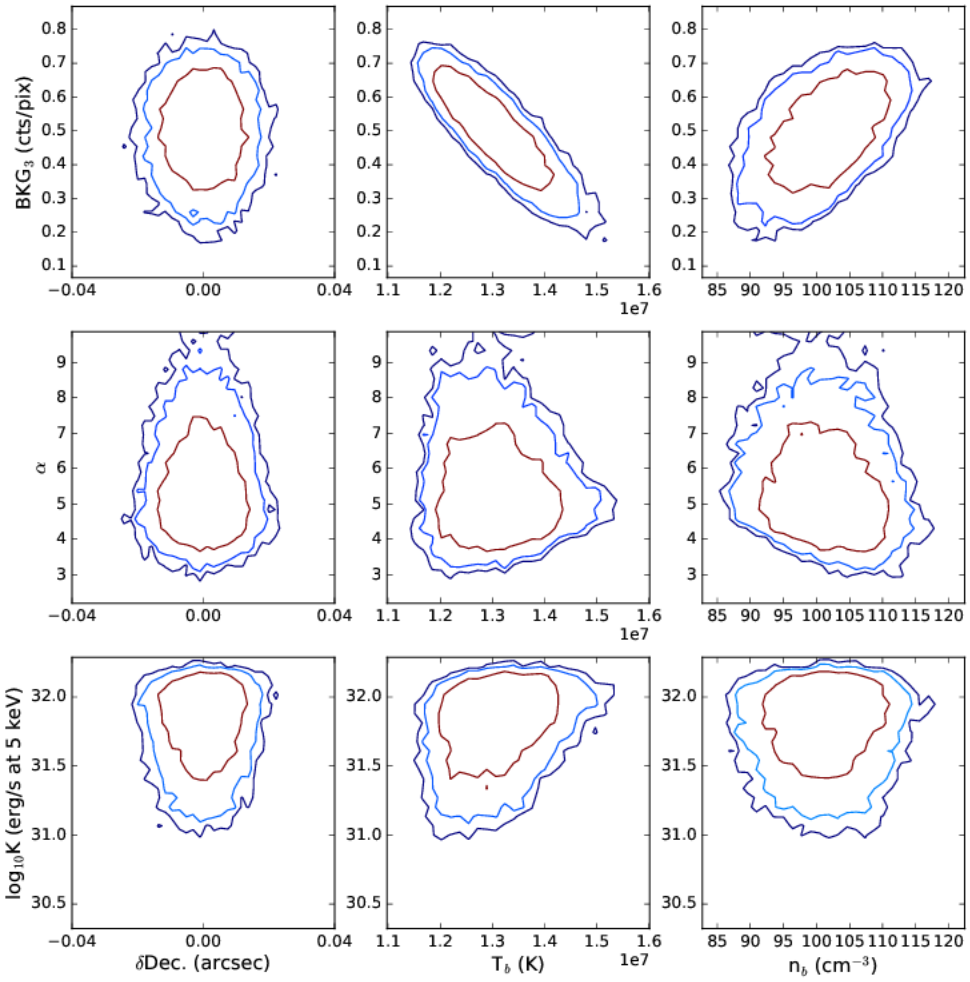

Figure C.8. Marginalized parameter histograms and parameter-parameter confidence intervals.

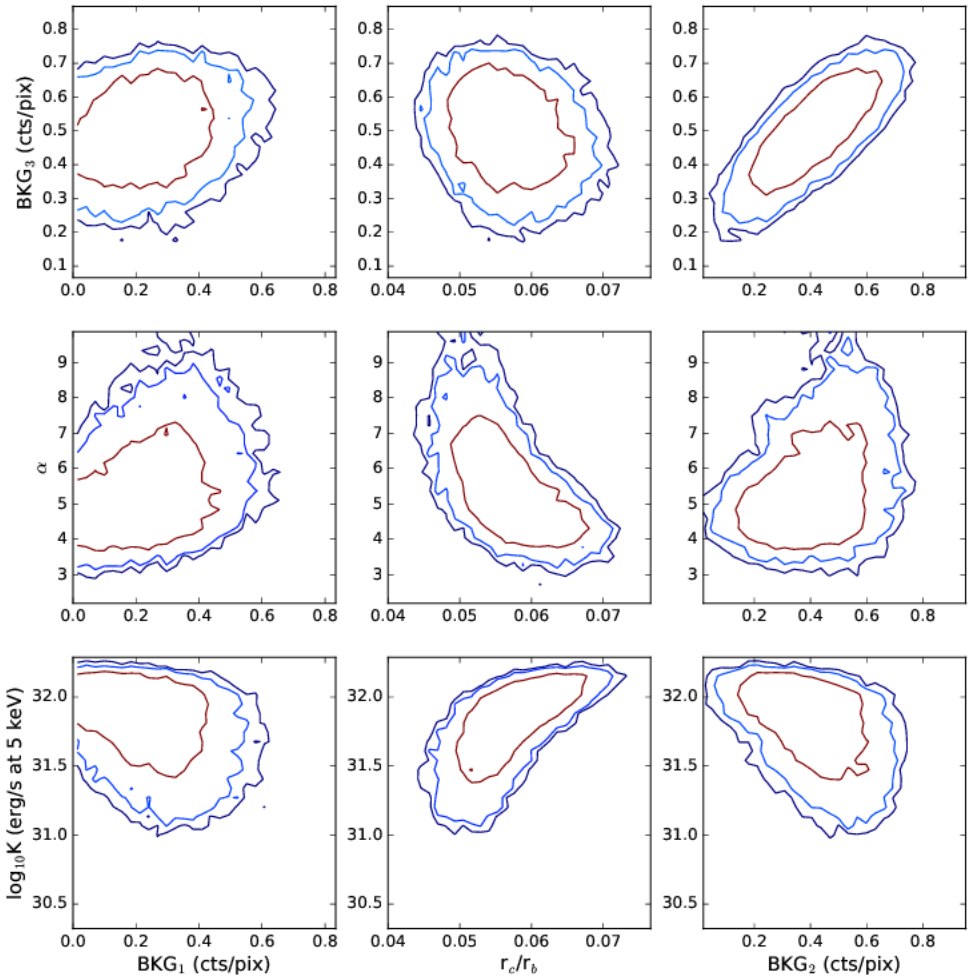

Figure C.9. Marginalized parameter histograms and parameter-parameter confidence intervals.

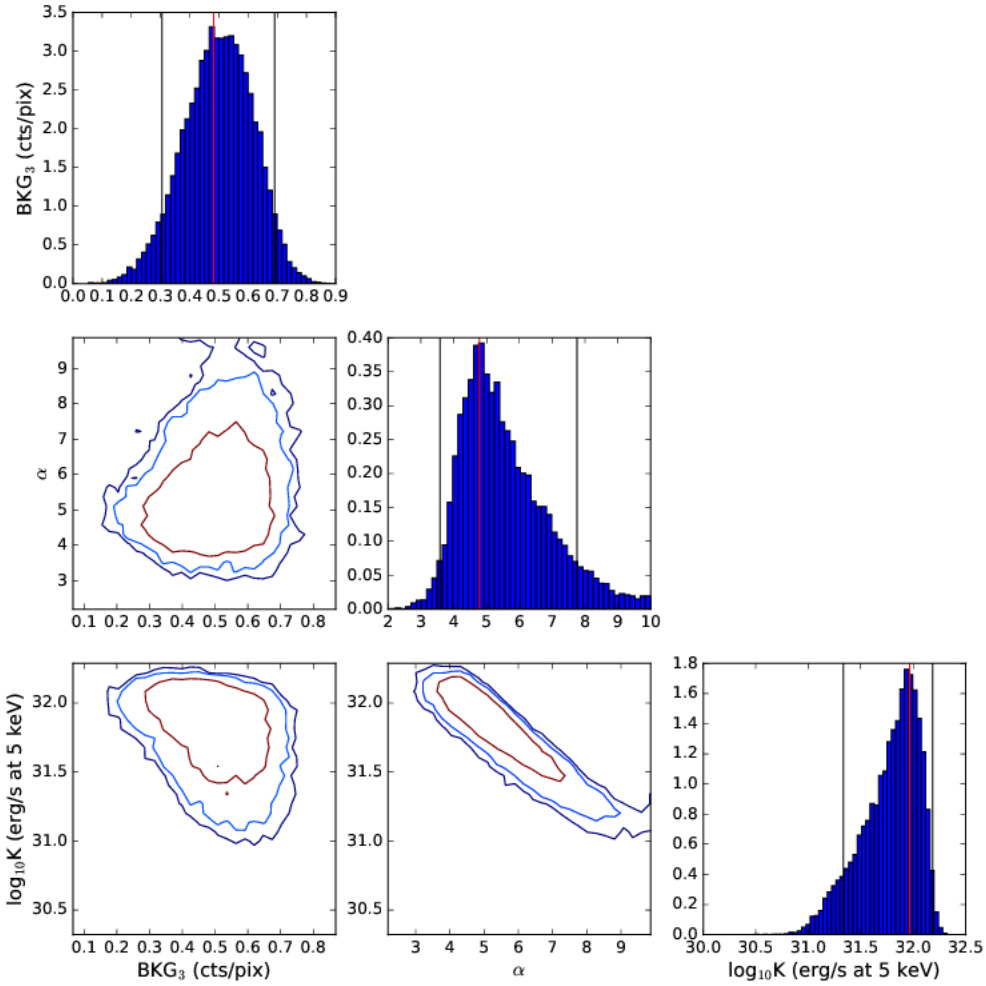

Figure C.10. Marginalized parameter histograms and parameter-parameter confidence intervals.

APPENDIX D

TESTING THE SAMPLING OF RGS LINE MAPS

Since this type of analysis of the RGS data has yet to be performed, testing is required to ensure physically meaningful results. However, it is infeasible to test all possible scenarios. Therefore, while we can set some basic guideline, we encourage users of this method to simulate observations of their target object considering all potentially important emission mechanisms. Past results and current data should be used to design the simulations as much as possible.

We assess simulations built specifically to mimic the emission from M31, which has useful past results that can be leveraged, under different physical scenarios. It has previously been found that the surface brightness in the broadband Chandra images can be described by the β-model with $r_c \sim 1'$ and $\beta \sim 0.5$ [77]. We can further estimate an appropriate I_0 for simulation by considering the observed image flux and the approximate fraction of observed counts contributed by the diffuse line emission. I_0 is estimated by requiring the integrated source emission to match the proper fraction of total emission. With this estimate, we have a fully characterized model to simulate from.

D.0.1 OVIII Lyα Emission

Building synthetic observation of the OVIII Lyα emission is relatively simple task. We begin by estimating parameters that provide a similar number of source counts as the observed M31 data. The background, as estimated above, represents 77% of the observed counts of the M31 OVIII line map on average. If we assume

Table D.1. Simulated OVIII parameters, best fit, and 95% confidence intervals.

	$I_{0,R}$ (counts/s/cm^2/asec^2)	$r_{c,R}$ (asec)	β_R
Simulated Value	0.64	60	0.5
Fitting Results	0.57 (0.5, 0.67)	68 (50, 90)	0.52 (0.45, 0.61)

that the fluxing maps are unity and pixels are 10" on a side, this implies $I_0 \approx 0.64$ counts/s/cm^2/arcsec^2. These parameters result in simulated observations with the same mean number of counts as the archival M31 observations, as well as the proper fraction of source to background emission. In order to simulate the data, we build an expected count image from the β-model and estimated background in the same way as when calculating the likelihood during model fitting, convolve it with the PSF and LSF, then add Poisson random noise.

Simulating and fitting 64 observations (OVIII allows us to use both RGS1 and RGS2) with these parameters, leads to the best fit parameters and confidence intervals shown in Figure D.1 and listed in Table D.1. We see that the parameters are reasonably well characterized. Perhaps the least constrained parameter is β, which is natural considering how weak the source emission of M31 is, only comprising 23% of the extracted image data. At radii larger than r_c, the emission is dominated by the background. Indeed, simulations with a larger source fraction of 50% are able to place a much stronger constraint on β. Yet, we see that we return our simulated parameters within the uncertainties. This suggests that the method proposed herein for characterizing the emission from isolated lines is reasonable to first order for M31.

D.0.2 OVII Kα Emission

While it is interesting to characterize the spatial distribution of isolated lines, the scientific meat of an X-ray spectrum resides in the diagnostic power of He-like triplets, making their characterization an important test for this method. For the case of M31, we know that the OVII Kα G-ratio is elevated to some extent [77]. Therefore, we need

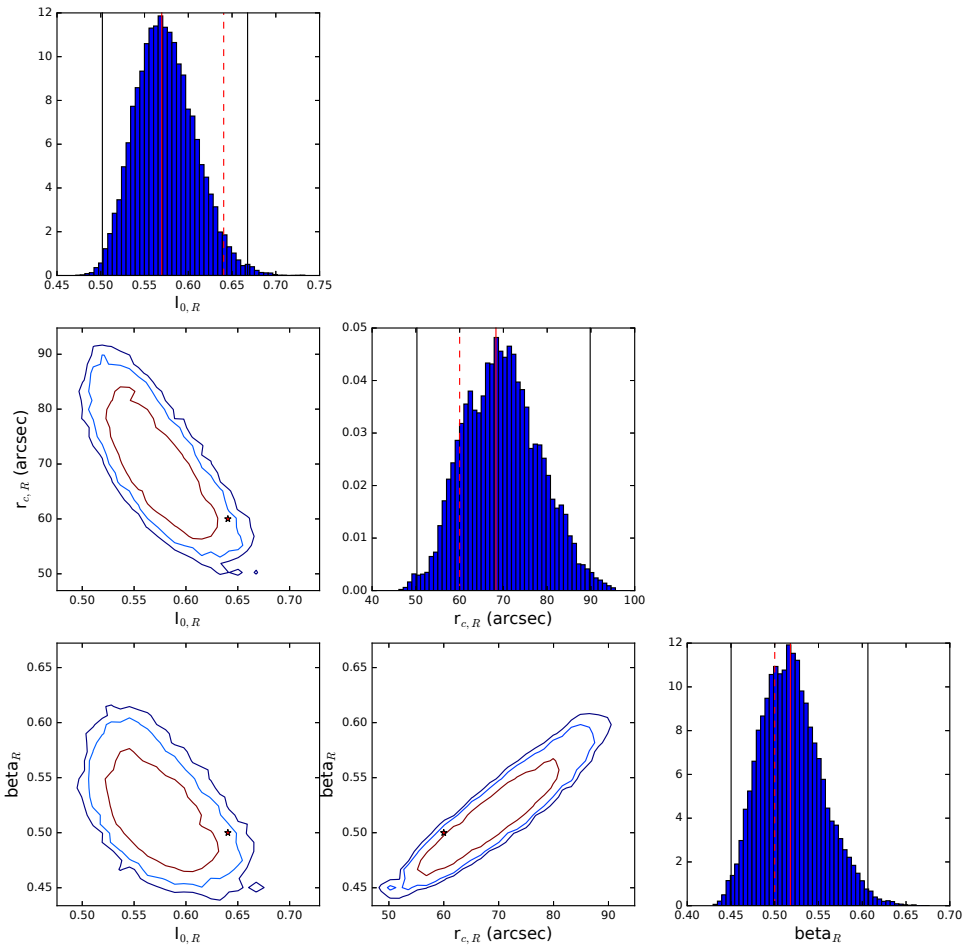

Figure D.1. Same as Figure 3.10 but for different parameters.

to specifically simulate any relevant physical scenarios beyond thermal. In this case we show simulate fits assuming resonance scattering is important for the emission.

In order to set expectations of a fit to the M31 data under the resonance scattering scenario, we can directly calculate what these profiles would be given past results. Previous fitting suggests the G-ratio (F/R) $\sim$ 1.5 in the inner bulge [77], implying $I_{0,F} = 1.5 I_{0,R}$. We also know that the object integrated G-ratio should be approximately thermal for resonance scattering. Assuming $\beta_{M31} = 0.5$ (that found with broadband fitting), this implies that $\beta_R \sim 0.32$ by requiring that the galaxy integrated G-ratio remains thermal. We will assume that $r_c = 1'$ is unchanged by resonance scattering. Lastly, to build the full model we simply need to estimate the total source flux in the M31 data, $I_{0,F} + I_{0,R}$. This is done in the same way as for OVIII. Unfortunately, OVII Kα is even fainter, with a source contribution to the flux of only 20%. This source flux implies $I_{0,F}$ and $I_{0,R}$ to be 0.17 and 0.11 counts/s/cm^2/arcsec^2, respectively. Note, we have also included in the simulated data a contribution from the inter-recombination line. In the case of resonance scattering, the profile of this line is equivalent to $C \times I_F(r)$, where C is a multiplicative constant equal to 0.22 (as calculated by *atomdb* for thermal emission).

The parameters and fitting results for 32 OVII observations[1] are shown in Figures D.2-D.4 and listed in Table D.2. As in the case of OVIII, we see that the simulated parameters are reproduced within the uncertainties. Unfortunately, the uncertainties are very large, particularly for both β and r_c for both lines. This perhaps shouldn't be surprising. Not only is the OVII emission relatively weaker than the OVIII emission, but it is also split among multiple lines. This results in a background dominated image throughout. Further, r_c and β can loosely be used to characterize the physical extent of the object, making them highly degenerate.

[1]Due to a CCD failure, only RGS1 data can be used for OVII.

Table D.2. Simulated OVII parameters, best fit, and 95% confidence intervals.

Resonance Line:	$I_{0,R}$ (counts/s/cm^2/asec^2)	$r_{c,R}$ (asec)	β_R
Simulated Value	0.11	60	0.32
Fitting Results	0.08 (0.05, 0.13)	105 (20, 390)	0.35 (0.32, 0.83)
Forbidden Line:	$I_{0,F}$ (counts/s/cm^2/asec^2)	$r_{c,F}$ (asec)	β_F
Simulated Value	0.17	60	0.50
Fitting Results	0.12 (0.08, 0.19)	83 (30, 185)	0.45 (0.36, 0.83)

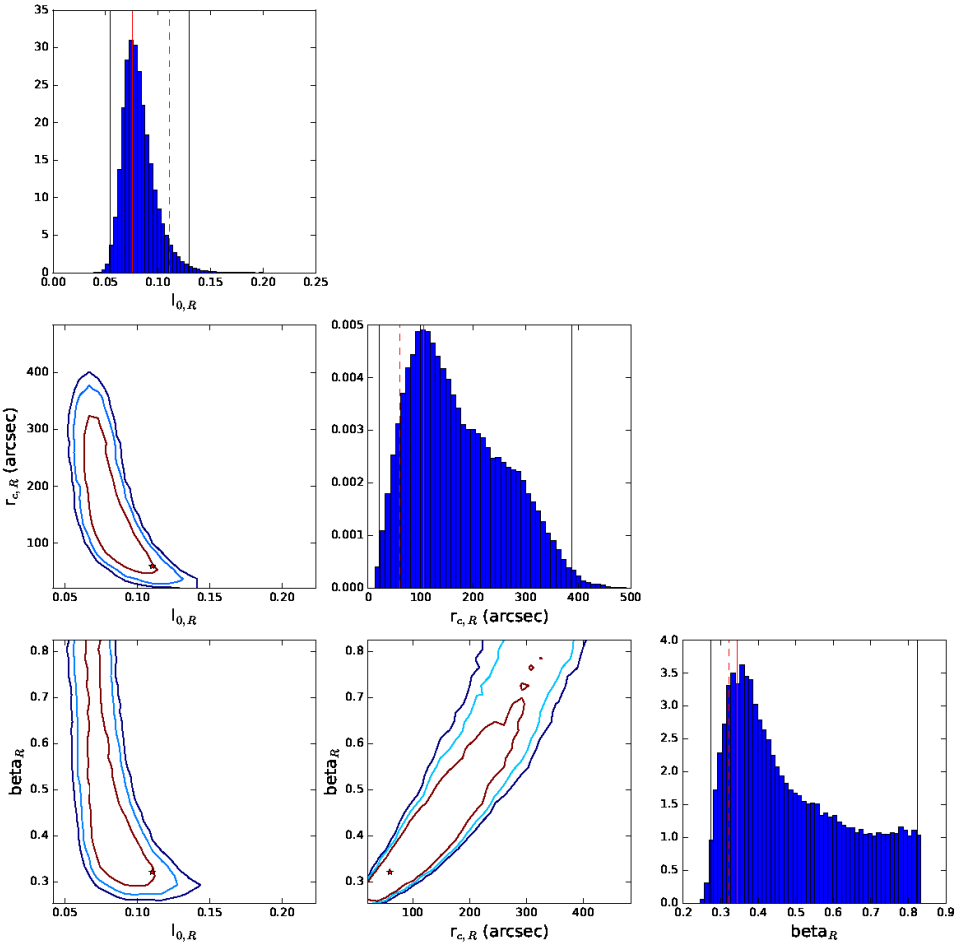

Figure D.2. Same as Figure 3.10 but for different parameters.

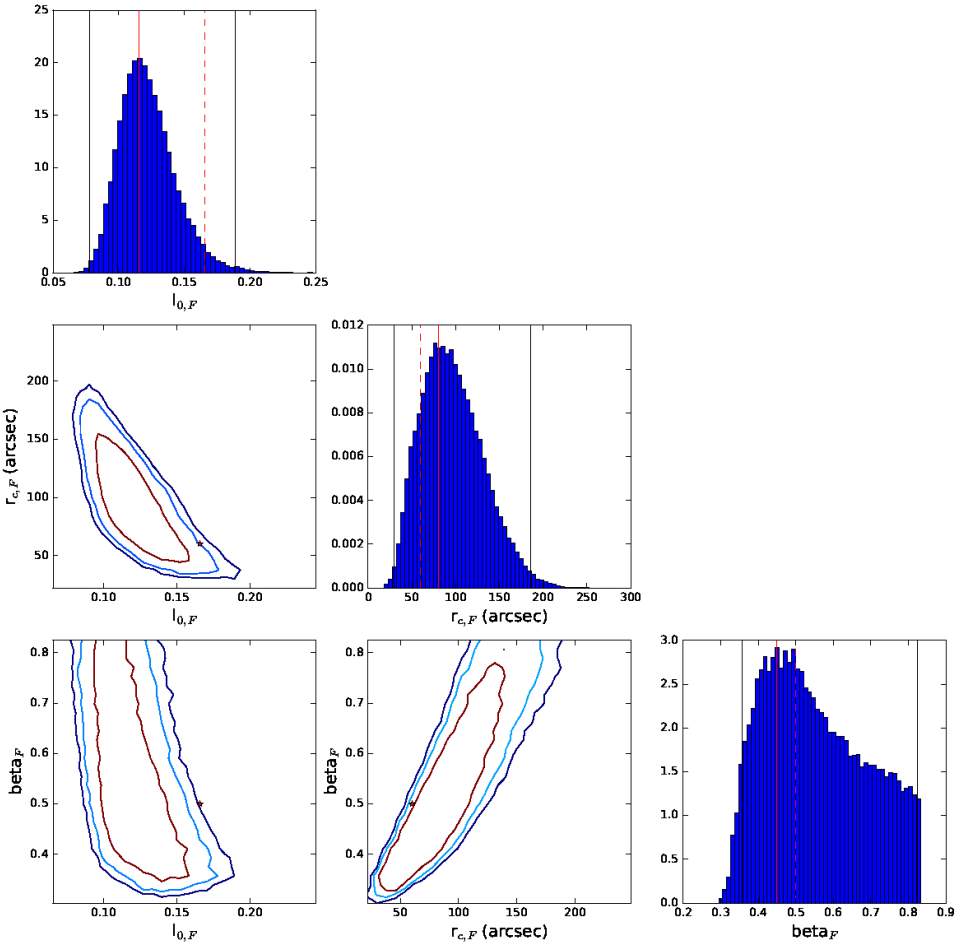

Figure D.3. Same as Figure 3.10 but for different parameters.

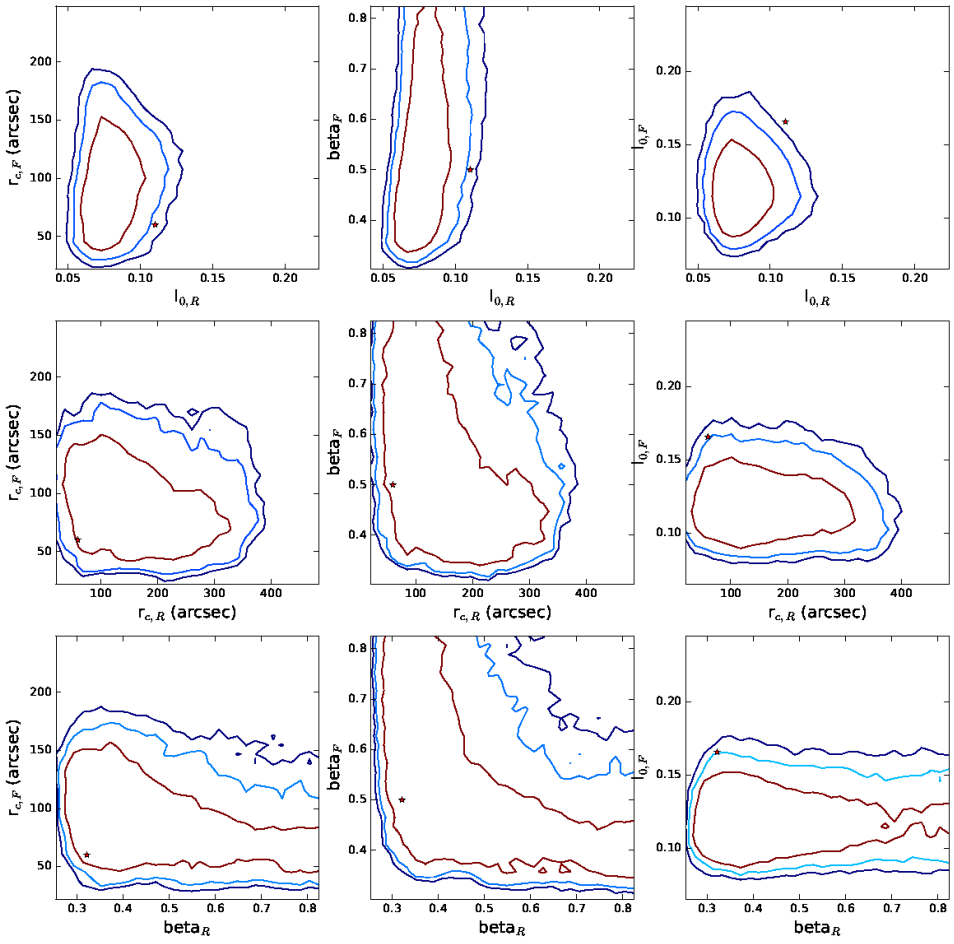

Figure D.4. Same as Figure 3.10 but for different parameters.

D.0.3 Joint Fitting

The strong correlation between many β and r_c suggests that using outside information to constrain either parameter will serve to greatly improve the fitting results. This can be done in one of two ways: using the broadband Chandra data or RGS imaging of other lines (either as a prior or simultaneous fitting). We will focus on simultaneous fitting of the latter case in this work. Fitting isolated lines in conjunction with blended lines provides particular power to constrain r_c and β. This power arises from the fact that for each physical scenario, we may link at least one of these parameters between the isolated line and one or more of the blended lines.

When fitting under the resonance scattering paradigm, we link r_c for all lines [118]. We may additionally link β for any lines that are not affected by resonance scattering. Thus, simultaneously fitting multiple lines and linking these parameters in a physically motived manner provides a natural way to overcome statistical limitations and provide tighter constraint to the β-model parameters. In this simulation, we assume that the OVII Lyα line is not effected by resonance scattering, and thus assume it has the same distribution as the forbidden line.

An example of this type of fit is shown in Figures D.5-D.7 and tabulated in Table D.3. We see that parameters are very well constrained, all to within $\sim 20\%$. This suggests that if the redistribution of photons through β for the OVII Kα resonance line leads to a change of 0.1, we will be able to detect the presence of resonance scattering in the M31 bulge. Therefore, this type of joint fitting allows us to overcome the weak flux of M31's diffuse hot gas.

Table D.3. Joint fitting OVIII and OVII for simulated data in the resonance scattering scenario, best fit and 95% confidence intervals.

Parameter	Sim. Val.	Best	Lower 95%	Upper 95%
$I_{0,OVIII,R}$ (counts/s/cm^2/asec^2)	0.64	0.64	0.57	0.71
$I_{0,OVII,R}$ (counts/s/cm^2/asec^2)	0.31	0.33	0.29	0.38
$I_{0,OVII,F}$ (counts/s/cm^2/asec^2)	0.16	0.17	0.14	0.20
$r_{c,M31}$ (asec)	60	53	45	64
β_{M31}	0.5	0.48	0.45	0.53
$\beta_{OVII,R}$	0.5	0.49	0.45	0.56

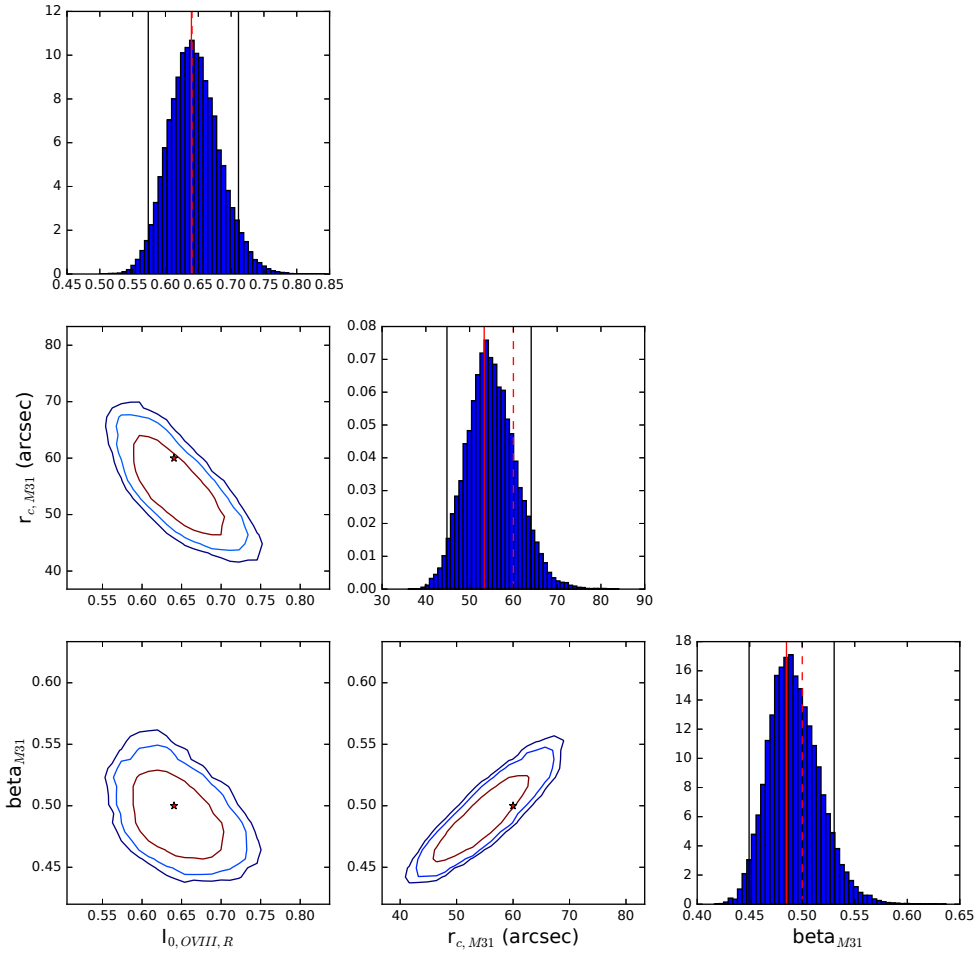

Figure D.5. Same as Figure 3.10 but for different parameters.

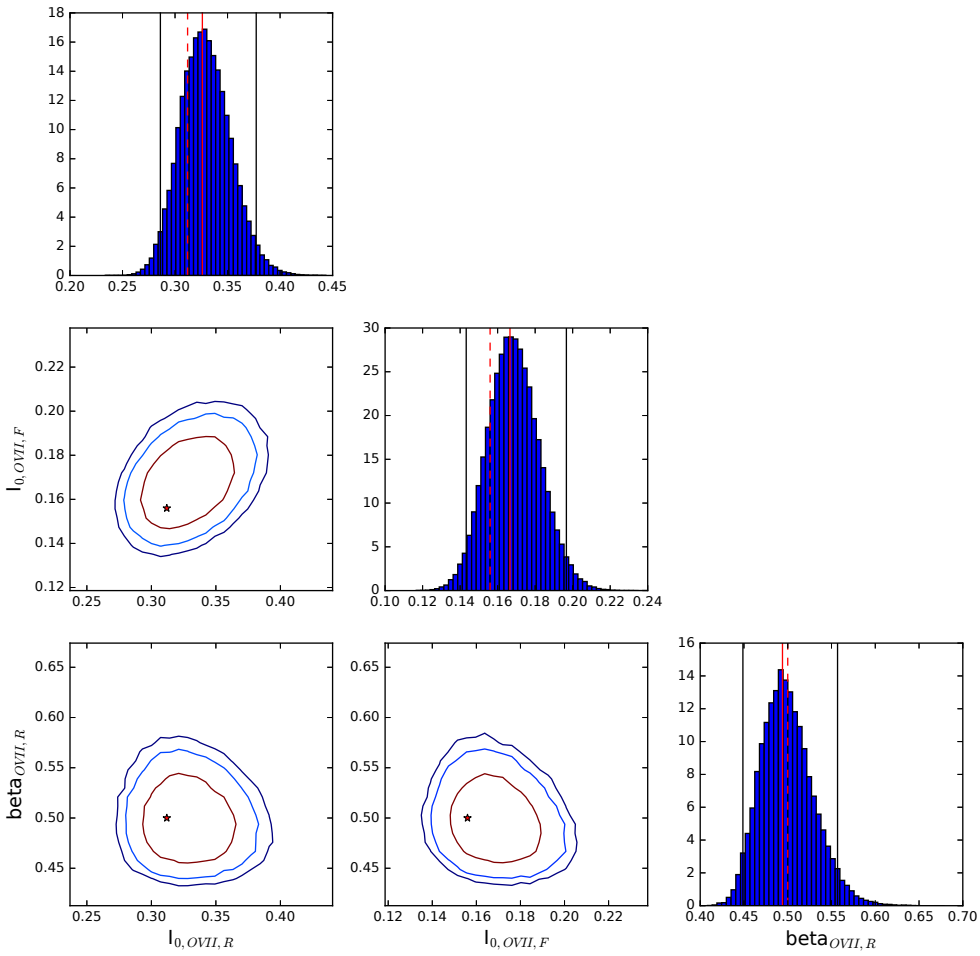

Figure D.6. Same as Figure 3.10 but for different parameters.

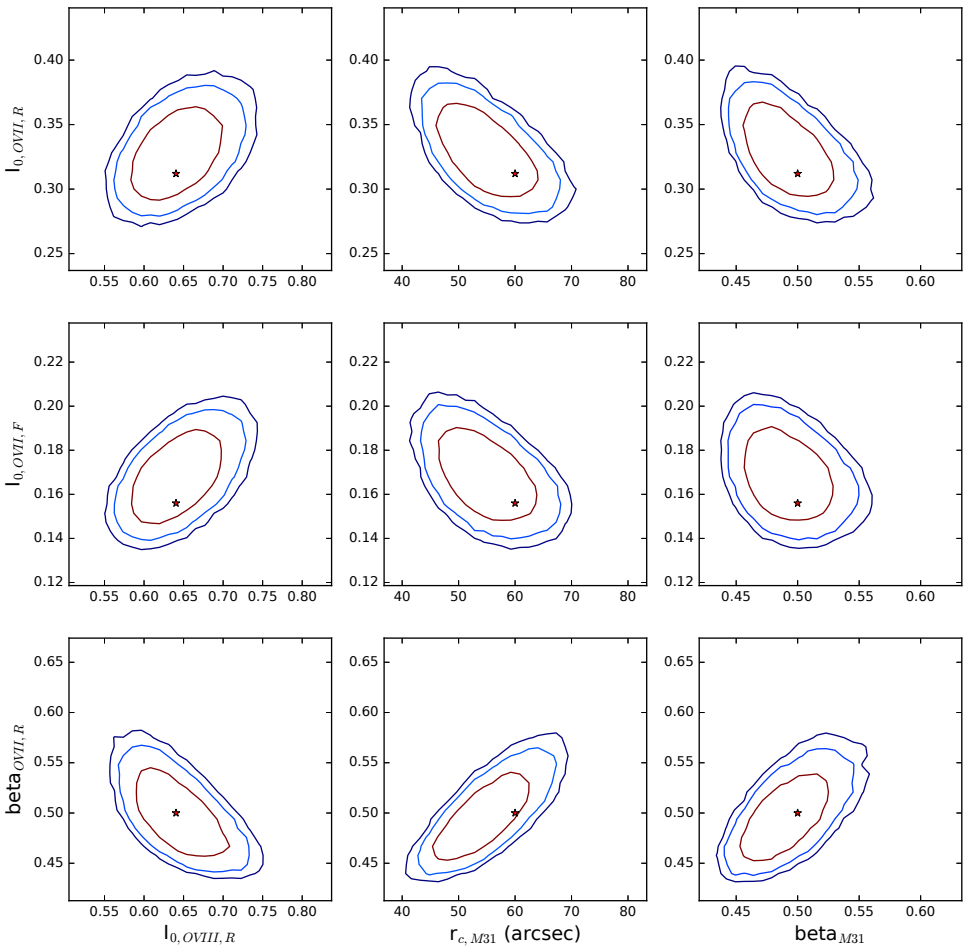

Figure D.7. Same as Figure 3.10 but for different parameters.

APPENDIX E

SEMIPARAMETRIC LINE MAPPING

The modelling discussed in Chapter 3, where we parameterized the emission as a β-model, was a natural first step. However, there are a couple reasons why we would want to avoid resorting to a parametric model. The primary reason is for understanding the spatial correlation between emission that traces a similar process or other gas phases. For example, the spatial complexity that gives rise to CX in the context of galactic winds is untenable with parametric modelling. When considering He-like Kα complexes, spatial correlation can be very useful for understanding the mechanism behind an elevated G-ratio [107]. This underscores the need for non-parametrically sampling of the underlying surface brightness.

Unfortunately, it is not possible to completely forward-fit the intrinsic surface brightness non-parametrically, treating each spatial point truly independently, due to the double convolution from the PSF and LSF. This can be naturally understood when considering what a convolution does. If you have two adjacent pixels, one with a very large value and the other with a very small value, their convolution will look much the same as two adjacent pixels with equal value, as long as the convolution kernel is at least similar in size to the pixel sizes. This means that the intrinisic surface brightness at some location that we are trying to sample is decoupled from the actual observed surface brightness at that location. Therefore, we need to include some kind of spatial model within the fit to get statistically meaningful results, particularly for blended lines.

One possibility would be utilizing Chandra data to guide how the the intrinsic surface brightness is spatially modelled by setting a prior on the scale of the Chandra PSF. Unfortunately, this approach has it's own challenges. The spectral resolution of the Chandra instrument is not sufficient to separate out individual line emission. Therefore, we would be trying to leverage spatial correlation in broadband emission. Individual emission lines can deviate significantly from their encompassing broadband emission, depending on which line(s) are being observed and which physical processes are important for the emission. For example, if the emission is significantly contaminated by CX, the OVII Kα forbidden line may not correlate well with the broadband emission (depending on the width of the broadband emission). If the emission is a reasonable blend of CX and thermal emission, none of the Kα lines may be well characterized by the broadband emission (as in Chapter 3). Therefore, this approach effectively holds us hostage to the thermal assumption once again.

E.1 Azimuthally Symmetric Models

A natural spatial model for a spheroid is to assume azimuthal symmetry. In this case, we sample bins through the projected radius. Since we assume azimuthal symmetry, any transformation due to roll angle can be neglected. For the case of an isolated line, the only correction that needs to be considered is for boresight between observations, which is naturally handled in the reduction pipeline. For a multiplet, the only additional consideration is the dispersion of individual line images in the proper direction. Therefore, this model is relatively simple and straightforward to implement. It also allows us to simultaneously retain a considerable amount of information from the observations and fit at very high signal-to-noise. However, there are some nuances.

The sampling procedure used in the semiparametric case is similar to that of the parametric example in Chapter 3. Both use a blocked Metropolis-Hastings MCMC sampler to estimate parameters and their confidence bounds, in this case, individual

pixels. However, there is one significant difference shown here. For the semiparametric fits to simulated emission we also fit the surface brightness in the background component. Without including the uncertainty in the background, we become far too overconfident in the source surface brightness estimate in regions where the background dominates. In the parametric case, the uncertainty in the background was much less important since the parameters were primarily constrained by the source surface brightness where the source emission dominates. Therefore, we weren't neglecting a major source of uncertainty.

We account for uncertainty in the background surface brightness by sampling a normalization parameter at each side of the image extraction region in the dispersion direction, $\vec{\mathscr{F}}_{bkg}$. The shape of the background in the cross dispersion direction is determined by the shape of the source flux. This is a reasonable characterization of the background for simulated data, where we generate images without including point sources. However, for real data, any point source emission must be taken into account for accurate results. Also, there will be a smooth instrumental background that needs to be considered. The renormalized background surface brightness at each image end are linearly interpolated along the dispersion direction to define the background at every pixel. This sampling has a separate probability calculation using only the continuum regions of the image where it is estimated.

Determining how to include the contribution from point-sources is a major challenge for semiparametric sampling of real data. One possible solution is to generate the shape of the background in the cross-dispersion direction in the same way as Chapter 3, then sample a normalization at each edge. This will include at least a portion of the uncertainty of the background flux in the fit.

If the line of interest is a blended line, each pixel will have an additional parameter, $\mathscr{G}$, equivalent to the ratio of the two lines. The additional line, however, also creates some problems for the background generation. For example, in the case where an ele-

vated G-ratio is primarily due to CX, any CX that results in the increase in forbidden line emission (and therefore total flux) would not affect the continuum (background) emission. Therefore, in this case we expect the background emission to closely follow the resonance line only. However, in the limiting case where the elevated G-ratio due to resonance scattering, the continuum will not follow the flux of the resonance line, but rather the forbidden line. Therefore, to move forward beyond this simplistic approach, it is again necessary to fit for both instances and then perform a model comparison as in Chapter 3.

E.1.1 Testing

As in Chapter 3, we simulate data to test the efficacy of the method. Again, we use the archival M31 data to guide our simulations. Recall, this data is convenient for two reasons: it has an abundance of archival data and being quiescent bulge emission, we expect it be reasonably well behaved. Therefore, testing against the M31 data should provide a good intuition for what is possible with the method.

To generate synthetic data from the M31 data, we start by calculating the mean number of counts in each observation. In this case, as opposed to Chapter 3, we assume that approximately 50% of the counts are background and the rest from the source. Note, this source percentage is larger than the actual data of M31, allowing us to probe a greater dynamic range in source to background flux through the image. We further assume the background is constant across the dispersion direction and that the source emission is a Gaussian with $\sigma \sim 100$ arcsec, similar to the angular extent of M31. These assumptions are taken to be true for all the simulations presented here. Lastly, to generate simulated observations, Poisson random noise is added to the theoretical emission profile. We create 30 simulated observations to analyze in tandem. For simplicity sake, when simulating data we will assume for each simulated

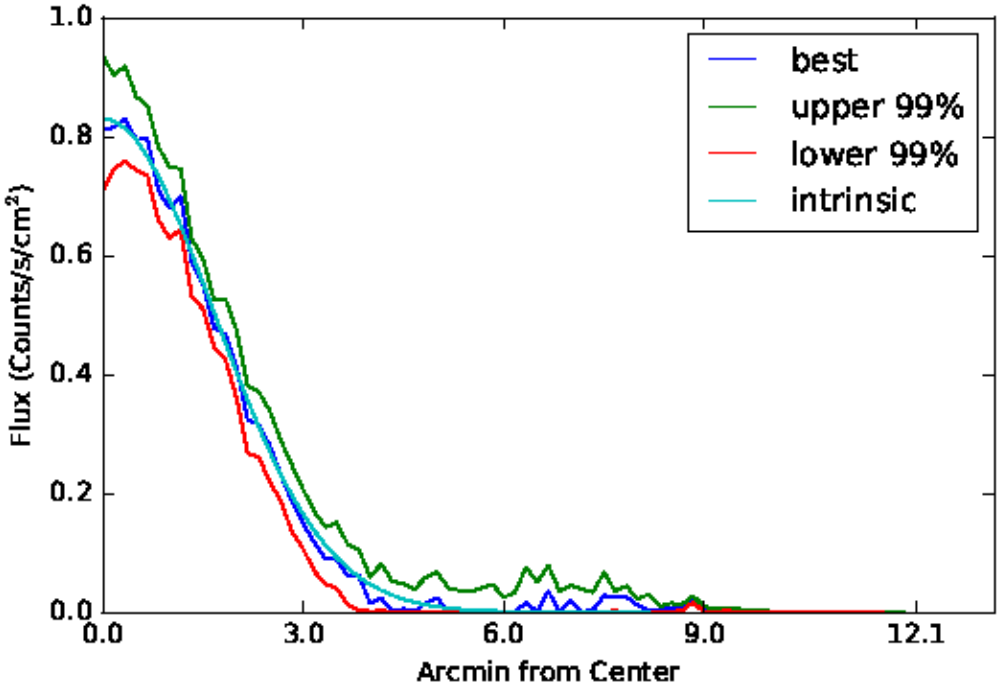

Figure E.1. Projected radial OVII flux profile for simulated data. Bin size is 10x the original RGS data. Radial bins are sampled independently.

observation that the exposure and effective area are unity. Also, all data has been rebinned to 10x the size of the raw RGS data for computational convenience.

We test this fitting procedure to a known simulated OVII complex under the resonance scattering paradigm. From Figures E.1 and E.2, we see that this model does reasonably well constraining the G-ratio and total flux through a range of radii. This fitting procedure sacrifices constraint at the lowest radial bins in order to extend the radial range of high quality fit. For physical circumstances similar to those simulated, we should be able to constrain the G-ratio fairly well out to $\sim$ 3'. Even though the signal-to-noise drops as we go to larger radii, the area of each radial bin is increasing out to moderate radii, until the small width of the cross dispersion extraction mitigates the gains. This is what allows the azimuthally symmetric model to constrain so well out to considerable radii.

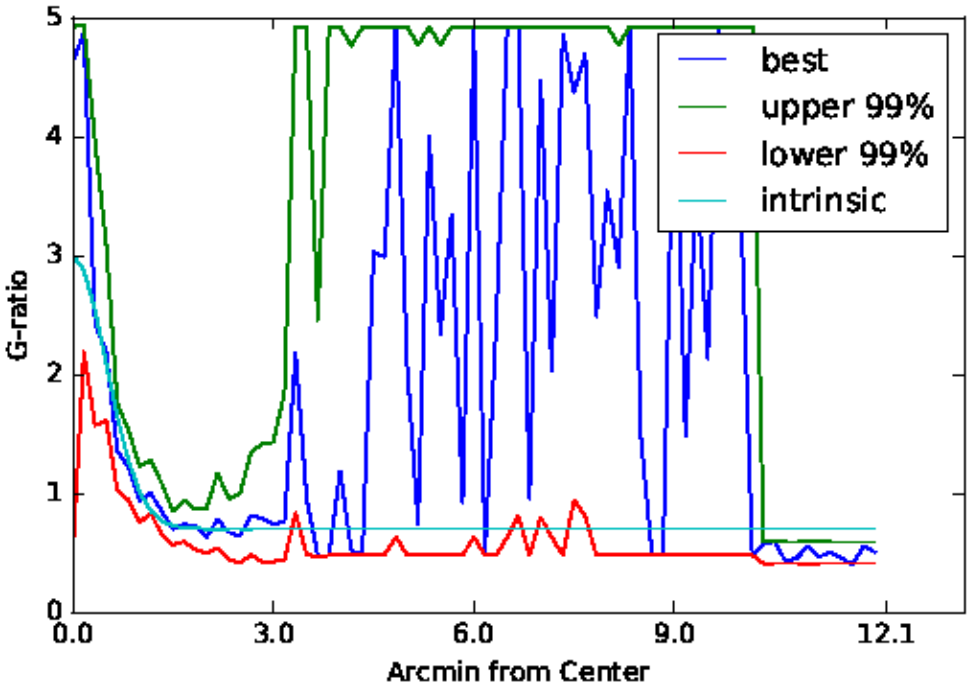

Figure E.2. Projected radial OVII G-ratio profile for simulated data. Bin size is 10x the original RGS data. Radial bins are sampled independently.

E.2 Kernel Model

Since the observed flux must be correlated on at least the scale of the PSF, another natural choice for including a spatial model is to model the emission after it has entered the telescope and been dispersed by the PSF. Because the data is Poisson, spatial correlation of the observed flux is difficult to visualize, and indeed, is not necessarily required by the data for a finite number of observations, each with finite exposure time. However, we know that the underlying distribution is smooth on at least the scale of the PSF, but the stochasticity of a Poisson process can mask this point. Therefore, there is additional untapped information in adjacent spatial bins if sampling each pixel independently.

The way in which we approach this can be conceptualized as fitting the distribution of a smoothing kernel. The smoothing kernel is defined by a radial basis function where the smoothing scale (or bandwidth) is set by the PSF of the instrument. That is, when sampling the surface brightness of some pixel, $\mathscr{F}_i$, we randomly draw a new new surface brightness, $\mathscr{F}_{i,new}$, and simultaneously adjust the surrounding pixels by this difference modulo a radial basis function:

$$\mathscr{F}_{j,new} = (\mathscr{F}_{i,new} - \mathscr{F}_{i,cur}) \exp\left(-\frac{(\mathscr{D}_{i,j})^2}{2(\epsilon/R)^2}\right) + \mathscr{F}_{j,cur} \tag{E.1}$$

where $\mathscr{D}_{i,j}$ is the distance between pixels i and j, ϵ is the spatial correlation scale between pixels (defaults to the RGS PSF, ~ 9.17 arcsec), and R is the pixel binning. Spatial correlation is thus fixed by the smoothing kernel during sampling.

For most observations, the signal-to-noise will not be great enough to allow a fully semiparametric 2-D fit to the data without symmetry assumptions. This is certainly not the case for M31. Therefore, we will demonstrate how this type of fit can be done by using 1D (cross-dispersion collapsed) data as an example. In this case, all maps are summed through the cross-dispersion direction. Sampling proceeds in the

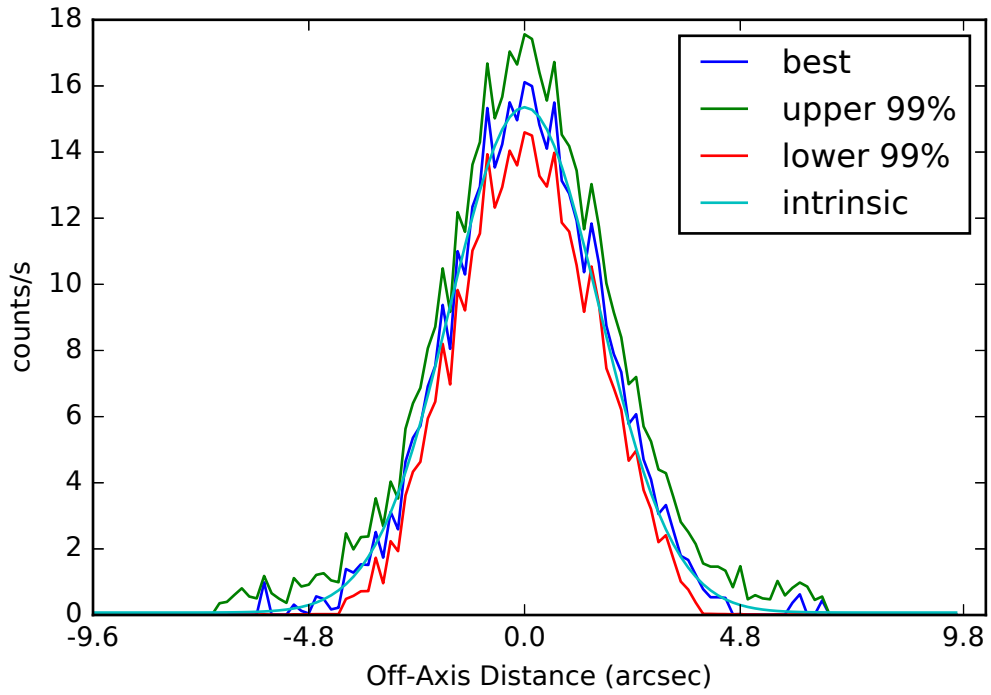

Figure E.3. Intrinsic OVIII profile and sampling best fit and confidence intervals. Observations are sampled at 0.1x RGS pixel resolution.

same fashion as in Chapter 3. However, in this case, since we are sampling the PSF convolved flux, we only convolve with the LSF when calculating the likelihood.

E.2.1 Testing

Naturally, an isolated line, such as OVIII Lyα, is the simplest. Figure E.3 shows the best fit and confidence intervals for pixels of 10x the original RGS data. The intrinsic flux is well represented within the confidence bounds, even within the background dominated regions. Therefore, in addition to being able to model more prominent emission very well, we also expect to be able to model an isolated line very well for M31.

Blended lines are a bit more complicated, as there are multiple components that need to be properly dispersed. For the case of He-like Kα emission, we sample the G-ratio and total flux at each pixel location. To cast into the coordinates of the observed

emission, this G-ratio and flux has to be separated into individual lines, dispersed, and recombined. For a theoretical G-ratio profile, we can look at some limiting cases. In this demonstration, we will consider the limiting case of the a relic-AGN.

In the relic-AGN scenario, the AGN burst leads to the plasma being over-ionized, which also leads to enhanced forbidden line emission relative to resonance line. In the core of the galaxy, where the density is large, the plasma is able to return to equilibrium on a shorter timescale. This leads to a G-ratio that is lowest in the center of the galaxy and enhanced in the outskirts. For this scenario, we use an inverse Guassian that rises from 1 in the center to 3 in the outskirts to define the G-ratio profile. It has the same width as the resonance scattering example. In this case, the flux and G ratio are both well fit and the results are shown in Figures E.4 and E.5. However, the G-ratio is not well constrained, suggesting we need to find a different solution for weak sources.

E.3 Discussion

We have demonstrated throughout this appendix and Chapter 3 the current potential of spatially mapping individual emission lines with a dispersive spectrometer. For isolated lines, we have shown this approach to be robust, even under conditions of very weak S/N. Therefore, we expect it to be possible to get semiparametric spatial information from these lines in 2D without relying on strong assumptions. Blended lines, however, may prove problematic. Nevertheless, in addition to the symmetry assumptions discussed above, there are a couple strategies we could leverage to further alleviate the problems with sampling blended lines.

We saw in Chapter 3 the tremendous power of simultaneously fitting lines. In that work, linking parameters between lines that are expected to be the same under a particular physical scenario allowed us to go from being enitrely incapable of distinguishing between physical scenarios to making considerably robust conclusions.

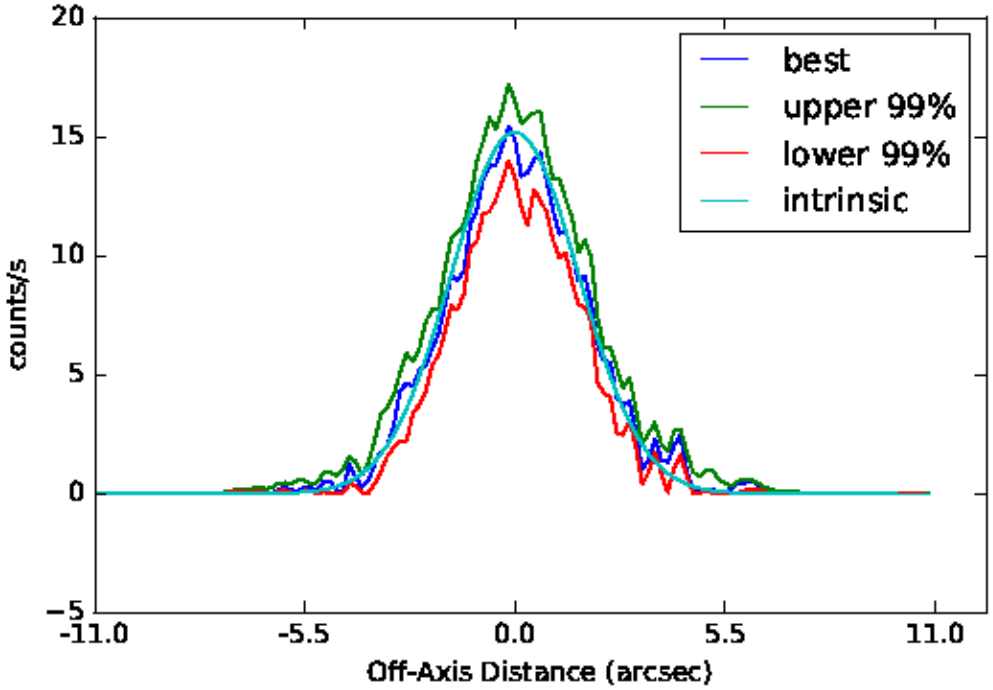

Figure E.4. Intrinsic OVII profile and sampling best fit and confidence intervals for the AGN burst scenario. Observations are sampled at 0.1x RGS pixel resolution.

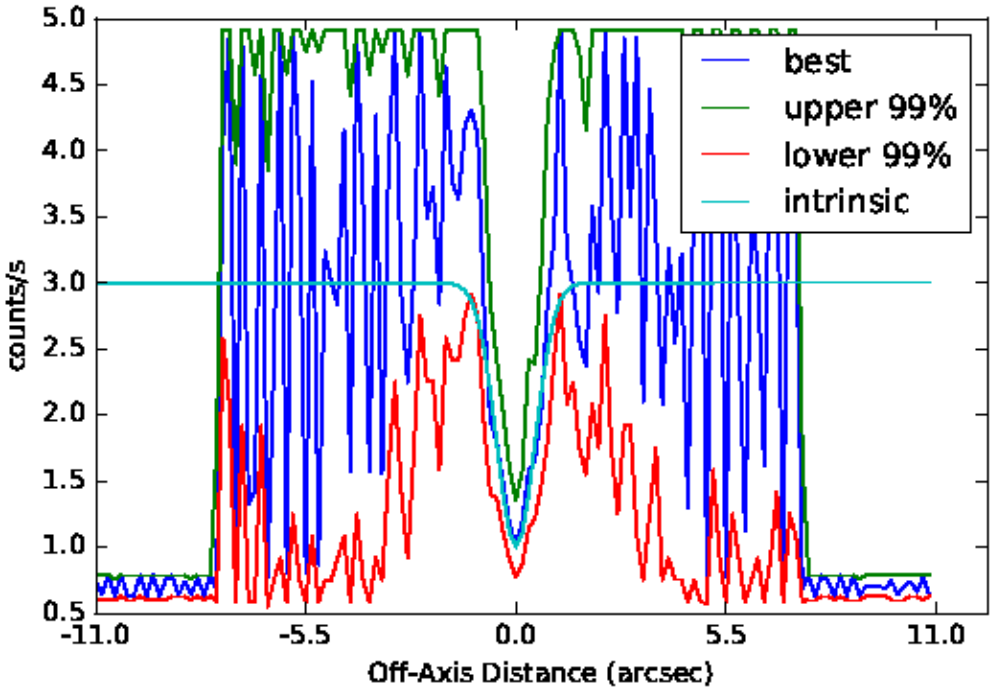

Figure E.5. Intrinsic OVII G-ratio profile and sampling best fit and confidence intervals for the AGN burst scenario. Observations are sampled at 0.1x RGS pixel resolution.

Such linking was straightforward in the parametric case. It is also straightforward in the non-parametric case, if we assume the plasma is isothermal. Such an assumption allows the linkage of any lines not affected by non-thermal processes with a global offset parameter. Therefore, if two lines are being fit, the number of parameters have been effectively halved. This strategy breaks geometry assumptions. Unfortunately, it is still hostage to the isothermal assumption.

In the absence of adequate CX and relic-AGN modelling, this final assumption of isothermality may only be removed for truly thermal emission, and possibly emission contaminated by resonance scattering. In those cases, a more elegant solution would be to simultaneously sample temperature and density distributions semiparametrically. In the case of resonance scattering, it may be adequate to fit these parameters using the azimuthally symmetric model, since this is likely only an issue for spheroids. Any lines not expected to be heavily contaminated by scattering may be directly linked. Lines that are contaminated may tangentially linked, as their object integrated fluxes should not deviate from thermal. For the case of purely thermal emission, all lines are linked through the hyperparameters of temperature and density. Therefore, in this case, it would be ideal to simultaneously fit as many lines as possible with the kernel model.

One final modelling technique for spheroids bears mentioning. Rather than fitting under azimuthal symmetry, one may assume spherical symmetry. Although, this may requires considerable computational overhead, as it necessitates integrating along the line of sight in each pixel. At full resolution, this may include 200,000 pixels. However, as the emission is much simpler than that in Chapter 2, the integral may be well estimated with the trapezoidal rule using relatively few bins. This method also places us in units that are more physically meaningful, that is, the emission properties as a function of the true radius, rather than the projected radius.

In conclusion, given the demonstrated capabilities and potentials discussed above, we believe this methodology has a considerable amount to offer X-ray astronomers, and astrophysics more generally. Novel techniques are required to move much of X-ray astrophysics forward, particularly with the unfortunate failure of Astro-H. Repurposing and leveraging the current fleet of grating spectrometers allows us to extract information that has no other clear methodology for illuminating at present. Therefore, we believe we are well poised to tackle the observation tasks enumerated in Chapter 4 to help elucidate the hot component of galatic feedback.

BIBLIOGRAPHY

[1] Baganoff, F. K., Bautz, M. W., Brandt, W. N., Chartas, G., Feigelson, E. D., Garmire, G. P., Maeda, Y., Morris, M., Ricker, G. R., Townsley, L. K., and Walter, F. Rapid X-ray flaring from the direction of the supermassive black hole at the Galactic Centre. *Nature 413* (Sept. 2001), 45–48.

[2] Baganoff, F. K., Maeda, Y., Morris, M., Bautz, M. W., Brandt, W. N., Cui, W., Doty, J. P., Feigelson, E. D., Garmire, G. P., Pravdo, S. H., Ricker, G. R., and Townsley, L. K. Chandra X-Ray Spectroscopic Imaging of Sagittarius A* and the Central Parsec of the Galaxy. *ApJ 591* (July 2003), 891–915.

[3] Ball, D., Ozel, F., Psaltis, D., and Chan, C.-k. Particle Acceleration and the Origin of X-ray Flares in GRMHD simulations of Sgr A*. *ArXiv e-prints* (Feb. 2016).

[4] Bauer, M., Pietsch, W., Trinchieri, G., Breitschwerdt, D., Ehle, M., and Read, A. High-resolution X-ray spectroscopy and imaging of the nuclear outflow of the starburst galaxy NGC 253. *AAP 467* (June 2007), 979–989.

[5] Bayes, T., and Price. An Essay towards Solving a Problem in the Doctrin of Chances. *Phil. Trans. 53* (Jan. 1763), 370–418.

[6] Begelman, M. C. Radiatively inefficient accretion: breezes, winds and hyperaccretion. *MNRAS 420* (Mar. 2012), 2912–2923.

[7] Beirão, P., Armus, L., Lehnert, M. D., Guillard, P., Heckman, T., Draine, B., Hollenbach, D., Walter, F., Sheth, K., Smith, J. D., Shopbell, P., Boulanger, F., Surace, J., Hoopes, C., and Engelbracht, C. Spatially resolved Spitzer-IRS spectral maps of the superwind in M82. *MNRAS 451* (Aug. 2015), 2640–2655.

[8] Beloborodov, A. M., Levin, Y., Eisenhauer, F., Genzel, R., Paumard, T., Gillessen, S., and Ott, T. Clockwise Stellar Disk and the Dark Mass in the Galactic Center. *ApJ 648* (Sept. 2006), 405–410.

[9] Bisnovatyi-Kogan, G. S., and Lovelace, R. V. E. Influence of Ohmic Heating on Advection-dominated Accretion Flows. *ApJL 486* (Sept. 1997), L43–L46.

[10] Bogdán, Á., and Gilfanov, M. Unresolved emission and ionized gas in the bulge of M31. *MNRAS 388* (July 2008), 56–66.

[11] Bond, J. R., Kofman, L., and Pogosyan, D. How filaments of galaxies are woven into the cosmic web. *Nature 380* (Apr. 1996), 603–606.

[12] Bondi, H. On spherically symmetrical accretion. *MNRAS 112* (1952), 195.

[13] Boroson, B., Kim, D.-W., and Fabbiano, G. Revisiting with Chandra the Scaling Relations of the X-ray Emission Components (Binaries, Nuclei, and Hot Gas) of Early-type Galaxies. *ApJ 729* (Mar. 2011), 12.

[14] Braun, R., Thilker, D. A., Walterbos, R. A. M., and Corbelli, E. A Wide-Field High-Resolution H I Mosaic of Messier 31. I. Opaque Atomic Gas and Star Formation Rate Density. *ApJ 695* (Apr. 2009), 937–953.

[15] Bregman, J. N. X-ray coronae around galaxies. *ApJ 237* (May 1980), 681–685.

[16] Brighenti, F., and Mathews, W. G. Thermal Evolution of Supernova Iron in Elliptical Galaxies. *ApJ 630* (Sept. 2005), 864–874.

[17] Broderick, A. E., Fish, V. L., Johnson, M. D., Rosenfeld, K., Wang, C., Doeleman, S. S., Akiyama, K., Johannsen, T., and Roy, A. L. Modeling Seven Years of Event Horizon Telescope Observations with Radiatively Inefficient Accretion Flow Models. *ApJ 820* (Apr. 2016), 137.

[18] Broos, P. S., Townsley, L. K., Feigelson, E. D., Getman, K. V., Bauer, F. E., and Garmire, G. P. Innovations in the Analysis of Chandra-ACIS Observations. *ApJ 714* (May 2010), 1582–1605.

[19] Bu, D.-F., and Yuan, F. Does the circularization radius exist or not for low-angular-momentum accretion? *MNRAS 442* (July 2014), 917–920.

[20] Bu, D.-F., Yuan, F., Wu, M., and Cuadra, J. On the role of initial and boundary conditions in numerical simulations of accretion flows. *MNRAS 434* (Sept. 2013), 1692–1701.

[21] Buote, D. A. Iron Gradients in Cooling Flow Galaxies and Groups. *ApJ 539* (Aug. 2000), 172–186.

[22] Buote, D. A., Lewis, A. D., Brighenti, F., and Mathews, W. G. XMM-Newton and Chandra Observations of the Galaxy Group NGC 5044. II. Metal Abundances and Supernova Fraction. *ApJ 595* (Sept. 2003), 151–166.

[23] Collinge, M. J., Brandt, W. N., Kaspi, S., Crenshaw, D. M., Elvis, M., Kraemer, S. B., Reynolds, C. S., Sambruna, R. M., and Wills, B. J. High-Resolution X-Ray and Ultraviolet Spectroscopy of the Complex Intrinsic Absorption in NGC 4051 with Chandra and the Hubble Space Telescope. *ApJ 557* (Aug. 2001), 2–17.

[24] Cuadra, J., Armitage, P. J., and Alexander, R. D. Stellar dynamical evidence against a cold disc origin for stars in the Galactic Centre. *MNRAS 388* (July 2008), L64–L68.

[25] Cuadra, J., Nayakshin, S., and Wang, Q. D. The role of feedback in accretion on low-luminosity AGN: Sgr A* case study. *MNRAS 450* (June 2015), 277–287.

[26] Davé, R., Katz, N., Oppenheimer, B. D., Kollmeier, J. A., and Weinberg, D. H. The neutral hydrogen content of galaxies in cosmological hydrodynamic simulations. *MNRAS 434* (Sept. 2013), 2645–2663.

[27] De Villiers, J.-P., and Hawley, J. F. Global General Relativistic Magnetohydrodynamic Simulations of Accretion Tori. *ApJ 592* (Aug. 2003), 1060–1077.

[28] De Villiers, J.-P., Hawley, J. F., Krolik, J. H., and Hirose, S. Magnetically Driven Accretion in the Kerr Metric. III. Unbound Outflows. *ApJ 620* (Feb. 2005), 878–888.

[29] Dennerl, K. Discovery of X-rays from Mars with Chandra. *AAP 394* (Nov. 2002), 1119–1128.

[30] Dennerl, K., Lisse, C. M., Bhardwaj, A., Burwitz, V., Englhauser, J., Gunell, H., Holmström, M., Jansen, F., Kharchenko, V., and Rodríguez-Pascual, P. M. First observation of Mars with XMM-Newton. High resolution X-ray spectroscopy with RGS. *AAP 451* (May 2006), 709–722.

[31] Diehl, S., and Statler, T. S. Adaptive binning of X-ray data with weighted Voronoi tessellations. *MNRAS 368* (May 2006), 497–510.

[32] Dong, H., Li, Z., Wang, Q. D., Lauer, T. R., Olsen, K. A. G., Saha, A., Dalcanton, J. J., and Groves, B. A. High-resolution mapping of dust via extinction in the M31 bulge. *MNRAS 459* (June 2016), 2262–2273.

[33] Draine, B. T., Aniano, G., Krause, O., Groves, B., Sandstrom, K., Braun, R., Leroy, A., Klaas, U., Linz, H., Rix, H.-W., Schinnerer, E., Schmiedeke, A., and Walter, F. Andromeda's Dust. *ApJ 780* (Jan. 2014), 172.

[34] Dunn, J. P., Bautista, M., Arav, N., Moe, M., Korista, K., Costantini, E., Benn, C., Ellison, S., and Edmonds, D. The Quasar Outflow Contribution to AGN Feedback: VLT Measurements of SDSS J0318-0600. *ApJ 709* (Feb. 2010), 611–631.

[35] Dunn, R. J. H., and Fabian, A. C. Investigating AGN heating in a sample of nearby clusters. *MNRAS 373* (Dec. 2006), 959–971.

[36] Eckart, A., García-Marín, M., Vogel, S. N., Teuben, P., Morris, M. R., Baganoff, F., Dexter, J., Schödel, R., Witzel, G., Valencia-S., M., Karas, V., Kunneriath, D., Straubmeier, C., Moser, L., Sabha, N., Buchholz, R., Zamaninasab, M., Mužić, K., Moultaka, J., and Zensus, J. A. Millimeter to X-ray flares from Sagittarius A*. *AAP 537* (Jan. 2012), A52.

[37] Evans, I. N., Primini, F. A., Glotfelty, K. J., Anderson, C. S., Bonaventura, N. R., Chen, J. C., Davis, J. E., Doe, S. M., Evans, J. D., Fabbiano, G., Galle, E. C., Gibbs, II, D. G., Grier, J. D., Hain, R. M., Hall, D. M., Harbo, P. N., (Helen He, X., Houck, J. C., Karovska, M., Kashyap, V. L., Lauer, J., McCollough, M. L., McDowell, J. C., Miller, J. B., Mitschang, A. W., Morgan, D. L., Mossman, A. E., Nichols, J. S., Nowak, M. A., Plummer, D. A., Refsdal, B. L., Rots, A. H., Siemiginowska, A., Sundheim, B. A., Tibbetts, M. S., Van Stone, D. W., Winkelman, S. L., and Zografou, P. The Chandra Source Catalog. *ApJS 189* (July 2010), 37–82.

[38] Fabian, A. C. Observational Evidence of Active Galactic Nuclei Feedback. *ARAA 50* (Sept. 2012), 455–489.

[39] Fabian, A. C., Arnaud, K. A., Bautz, M. W., and Tawara, Y. ASCA observations of cooling flows in clusters of galaxies. *ApJL 436* (Nov. 1994), L63–L66.

[40] Fabian, A. C., Sanders, J. S., Crawford, C. S., Conselice, C. J., Gallagher, J. S., and Wyse, R. F. G. The relationship between the optical Hα filaments and the X-ray emission in the core of the Perseus cluster. *MNRAS 344* (Sept. 2003), L48–L52.

[41] Fabian, A. C., Sanders, J. S., Taylor, G. B., Allen, S. W., Crawford, C. S., Johnstone, R. M., and Iwasawa, K. A very deep Chandra observation of the Perseus cluster: shocks, ripples and conduction. *MNRAS 366* (Feb. 2006), 417–428.

[42] Fabian, A. C., Sanders, J. S., Williams, R. J. R., Lazarian, A., Ferland, G. J., and Johnstone, R. M. The energy source of the filaments around the giant galaxy NGC 1275. *MNRAS 417* (Oct. 2011), 172–177.

[43] Falcke, H., Goss, W. M., Matsuo, H., Teuben, P., Zhao, J.-H., and Zylka, R. The Simultaneous Spectrum of Sagittarius A* from 20 Centimeters to 1 Millimeter and the Nature of the Millimeter Excess. *ApJ 499* (May 1998), 731–734.

[44] Ganguly, R., Brotherton, M. S., Cales, S., Scoggins, B., Shang, Z., and Vestergaard, M. Outflows and the Physical Properties of Quasars. *ApJ 665* (Aug. 2007), 990–1003.

[45] Gastaldello, F., and Molendi, S. Abundance Gradients and the Role of Supernovae in M87. *ApJ 572* (June 2002), 160–168.

[46] Genzel, R., Eisenhauer, F., and Gillessen, S. The Galactic Center massive black hole and nuclear star cluster. *Reviews of Modern Physics 82* (Oct. 2010), 3121–3195.

[47] Guo, F., Liu, Y.-H., Daughton, W., and Li, H. Particle Acceleration and Plasma Dynamics during Magnetic Reconnection in the Magnetically Dominated Regime. *ApJ 806* (June 2015), 167.

[48] Hawley, J. F., and Balbus, S. A. The Dynamical Structure of Nonradiative Black Hole Accretion Flows. *ApJ 573* (July 2002), 738–748.

[49] Hayashi, K., Fukazawa, Y., Tozuka, M., Nishino, S., Matsushita, K., Takei, Y., and Arnaud, K. A. Suzaku Observation of the Metallicity Distribution in the Elliptical Galaxy NGC 4636. *PASJ 61* (Dec. 2009), 1185–1196.

[50] Hoffman, M.D., and Gelman, A. The No-U-Turn Sampler: Adaptively Setting Path Lengths in Hamiltonian Monte Carlo. *Journal of Machine Learning Research 15* (Apr. 2014), 1351–1381.

[51] Hopkins, P. F. A new class of accurate, mesh-free hydrodynamic simulation methods. *MNRAS 450* (June 2015), 53–110.

[52] Hopkins, P. F., Quataert, E., and Murray, N. Stellar feedback in galaxies and the origin of galaxy-scale winds. *MNRAS 421* (Apr. 2012), 3522–3537.

[53] Hornstein, S. D., Ghez, A. M., Tanner, A., Morris, M., Becklin, E. E., and Wizinowich, P. Limits on the Short-Term Variability of Sagittarius A* in the Near-Infrared. *ApJL 577* (Sept. 2002), L9–L13.

[54] Hoshino, M. Particle Acceleration during Magnetorotational Instability in a Collisionless Accretion Disk. *ApJ 773* (Aug. 2013), 118.

[55] Ji, J., Irwin, J. A., Athey, A., Bregman, J. N., and Lloyd-Davies, E. J. Elemental Abundances in the X-Ray Gas of Early-Type Galaxies with XMM-Newton and Chandra Observations. *ApJ 696* (May 2009), 2252–2268.

[56] Kass, R. E., and Raftery, A. E. Bayes Factors. *JASA 90* (June 1995), 773–795.

[57] Katsuda, S., Tsunemi, H., Mori, K., Uchida, H., Kosugi, H., Kimura, M., Nakajima, H., Takakura, S., Petre, R., Hewitt, J. W., and Yamaguchi, H. Possible Charge-exchange X-ray Emission in the Cygnus Loop Detected with Suzaku. *ApJ 730* (Mar. 2011), 24.

[58] Katz, N., Weinberg, D. H., and Hernquist, L. Cosmological Simulations with TreeSPH. *ApJS 105* (July 1996), 19.

[59] Keel, W. C., Maksym, W. P., Bennert, V. N., Lintott, C. J., Chojnowski, S. D., Moiseev, A., Smirnova, A., Schawinski, K., Urry, C. M., Evans, D. A., Pancoast, A., Scott, B., Showley, C., and Flatland, K. HST Imaging of Fading AGN Candidates. I. Host-galaxy Properties and Origin of the Extended Gas. *AJ 149* (May 2015), 155.

[60] Kereš, D., Katz, N., Davé, R., Fardal, M., and Weinberg, D. H. Galaxies in a simulated ΛCDM universe - II. Observable properties and constraints on feedback. *MNRAS 396* (July 2009), 2332–2344.

[61] Kereš, D., Katz, N., Fardal, M., Davé, R., and Weinberg, D. H. Galaxies in a simulated ΛCDM Universe - I. Cold mode and hot cores. *MNRAS 395* (May 2009), 160–179.

[62] Kereš, D., Katz, N., Weinberg, D. H., and Davé, R. How do galaxies get their gas? *MNRAS 363* (Oct. 2005), 2–28.

[63] Kharchenko, V., Bhardwaj, A., Dalgarno, A., Schultz, D. R., and Stancil, P. C. Modeling spectra of the north and south Jovian X-ray auroras. *Journal of Geophysical Research (Space Physics) 113* (Aug. 2008), A08229.

[64] Kim, D.-W., and Fabbiano, G. X-Ray Scaling Relation in Early-type Galaxies: Dark Matter as a Primary Factor in Retaining Hot Gas. *ApJ 776* (Oct. 2013), 116.

[65] Konami, S., Matsushita, K., Tsuru, T. G., Gandhi, P., and Tamagawa, T. Suzaku Metal Abundance Patterns in the Outflow Region of M82 and the Importance of Charge Exchange. *PASJ 63* (Nov. 2011), S913–S924.

[66] Kowal, G., de Gouveia Dal Pino, E. M., and Lazarian, A. Particle Acceleration in Turbulence and Weakly Stochastic Reconnection. *Physical Review Letters 108*, 24 (June 2012), 241102.

[67] Lawrie, D. G. Velocity dispersion of planetary nebulae in the nuclear bulge of M31. *ApJ 273* (Oct. 1983), 562–575.

[68] Lehe, R., Parrish, I. J., and Quataert, E. The Heating of Test Particles in Numerical Simulations of Alfvénic Turbulence. *ApJ 707* (Dec. 2009), 404–419.

[69] Leitherer, C., Schaerer, D., Goldader, J. D., Delgado, R. M. G., Robert, C., Kune, D. F., de Mello, D. F., Devost, D., and Heckman, T. M. Starburst99: Synthesis Models for Galaxies with Active Star Formation. *ApJS 123* (July 1999), 3–40.

[70] Li, J., Ostriker, J., and Sunyaev, R. Rotating Accretion Flows: From Infinity to the Black Hole. *ApJ 767* (Apr. 2013), 105.

[71] Li, M., Bryan, G. L., and Ostriker, J. P. Quantifying Supernovae-Driven Multiphase Galactic Outflows. *ArXiv e-prints* (Oct. 2016).

[72] Li, Y.-P., Yuan, F., and Wang, Q. D. Confronting the Jet Model of Sgr A* with the Faraday Rotation Measure Observations. *ApJ 798* (Jan. 2015), 22.

[73] Li, Z., Jones, C., Forman, W. R., Kraft, R. P., Lal, D. V., Di Stefano, R., Spitler, L. R., Tang, S., Wang, Q. D., Gilfanov, M., and Revnivtsev, M. X-ray Emission from the Sombrero Galaxy: A Galactic-scale Outflow. *ApJ 730* (Apr. 2011), 84.

[74] Li, Z., and Wang, Q. D. Chandra Detection of Diffuse Hot Gas in and around the M31 Bulge. *ApJL 668* (Oct. 2007), L39–L42.

[75] Lister, M. L., Aller, M. F., Aller, H. D., Homan, D. C., Kellermann, K. I., Kovalev, Y. Y., Pushkarev, A. B., Richards, J. L., Ros, E., and Savolainen, T. MOJAVE: XIII. Parsec-scale AGN Jet Kinematics Analysis Based on 19 years of VLBA Observations at 15 GHz. *AJ 152* (July 2016), 12.

[76] Liu, J., Mao, S., and Wang, Q. D. Charge-exchange X-ray emission of M82: Kα triplets of O VII, Ne IX and Mg XI. *MNRAS 415* (July 2011), L64–L68.

[77] Liu, J., Wang, Q. D., Li, Z., and Peterson, J. R. X-ray spectroscopy of the hot gas in the M31 bulge. *MNRAS 404* (June 2010), 1879–1885.

[78] Liu, J., Wang, Q. D., and Mao, S. Charge-exchange X-ray emission of nearby star-forming galaxies. *MNRAS 420* (Mar. 2012), 3389–3395.

[79] Liu, S., and Melia, F. New Constraints on the Nature of Radio Emission in Sagittarius A*. *ApJL 561* (Nov. 2001), L77–L80.

[80] Loewenstein, M., and Davis, D. S. An In-depth Study of the Abundance Pattern in the Hot Interstellar Medium in NGC 4649. *ApJ 757* (Oct. 2012), 121.

[81] Marrone, D. P., Moran, J. M., Zhao, J.-H., and Rao, R. An Unambiguous Detection of Faraday Rotation in Sagittarius A*. *ApJL 654* (Jan. 2007), L57–L60.

[82] Martin, C. L. Mapping Large-Scale Gaseous Outflows in Ultraluminous Galaxies with Keck II ESI Spectra: Variations in Outflow Velocity with Galactic Mass. *ApJ 621* (Mar. 2005), 227–245.

[83] Martins, F., Genzel, R., Hillier, D. J., Eisenhauer, F., Paumard, T., Gillessen, S., Ott, T., and Trippe, S. Stellar and wind properties of massive stars in the central parsec of the Galaxy. *AAP 468* (June 2007), 233–254.

[84] McKernan, B., Yaqoob, T., George, I. M., and Turner, T. J. The Kinematics and Physical Conditions of the Ionized Gas in NGC 4593 from Chandra High-Energy Grating Spectroscopy. *ApJ 593* (Aug. 2003), 142–159.

[85] McNamara, B. R., and Nulsen, P. E. J. Heating Hot Atmospheres with Active Galactic Nuclei. *ARAA 45* (Sept. 2007), 117–175.

[86] McNamara, B. R., Russell, H. R., Nulsen, P. E. J., Hogan, M. T., Fabian, A. C., Pulido, F., and Edge, A. C. A Mechanism for Stimulated AGN Feedback in Massive Galaxies. *ArXiv e-prints* (Apr. 2016).

[87] McNamara, B. R., Wise, M., Nulsen, P. E. J., David, L. P., Sarazin, C. L., Bautz, M., Markevitch, M., Vikhlinin, A., Forman, W. R., Jones, C., and Harris, D. E. Chandra X-Ray Observations of the Hydra A Cluster: An Interaction between the Radio Source and the X-Ray-emitting Gas. *ApJL 534* (May 2000), L135–L138.

[88] Melia, F., Liu, S., and Coker, R. A Magnetic Dynamo Origin for the Submillimeter Excess in Sagittarius A*. *ApJ 553* (May 2001), 146–157.

[89] Narayan, R., SÄ dowski, A., Penna, R. F., and Kulkarni, A. K. GRMHD simulations of magnetized advection-dominated accretion on a non-spinning black hole: role of outflows. *MNRAS 426* (Nov. 2012), 3241–3259.

[90] Narayan, R., and Yi, I. Advection-dominated accretion: Self-similarity and bipolar outflows. *ApJ 444* (May 1995), 231–243.

[91] Neilsen, J., Markoff, S., Nowak, M. A., Dexter, J., Witzel, G., Barrière, N., Li, Y., Baganoff, F. K., Degenaar, N., Fragile, P. C., Gammie, C., Goldwurm, A., Grosso, N., and Haggard, D. The X-Ray Flux Distribution of Sagittarius A* as Seen by Chandra. *ApJ 799* (Feb. 2015), 199.

[92] Neilsen, J., Nowak, M. A., Gammie, C., Dexter, J., Markoff, S., Haggard, D., Nayakshin, S., Wang, Q. D., Grosso, N., Porquet, D., Tomsick, J. A., Degenaar, N., Fragile, P. C., Houck, J. C., Wijnands, R., Miller, J. M., and Baganoff, F. K. A Chandra/HETGS Census of X-Ray Variability from Sgr A* during 2012. *ApJ 774* (Sept. 2013), 42.

[93] Ostriker, J. P., Jiang, Y., Novak, G. S., Choi, E., and Ciotti, L. AGN Feedback from "RRIOS" - Rotating-Radiating-Inflow-Outflow-Solutions. (In Preparation).

[94] Paumard, T., Genzel, R., Martins, F., Nayakshin, S., Beloborodov, A. M., Levin, Y., Trippe, S., Eisenhauer, F., Ott, T., Gillessen, S., Abuter, R., Cuadra, J., Alexander, T., and Sternberg, A. The Two Young Star Disks in the Central Parsec of the Galaxy: Properties, Dynamics, and Formation. *ApJ 643* (June 2006), 1011–1035.

[95] Porquet, D., Dubau, J., and Grosso, N. He-like Ions as Practical Astrophysical Plasma Diagnostics: From Stellar Coronae to Active Galactic Nuclei. *SSR 157* (Dec. 2010), 103–134.

[96] Porquet, D., Mewe, R., Dubau, J., Raassen, A. J. J., and Kaastra, J. S. Line ratios for helium-like ions: Applications to collision-dominated plasmas. *AAP 376* (Sept. 2001), 1113–1122.

[97] Pounds, K. A., King, A. R., Page, K. L., and O'Brien, P. T. Evidence of a high-velocity ionized outflow in a second narrow-line quasar PG 0844+349. *MNRAS 346* (Dec. 2003), 1025–1030.

[98] Pringle, J. E. Accretion discs in astrophysics. *ARAA 19* (1981), 137–162.

[99] Quataert, E. Particle Heating by Alfvénic Turbulence in Hot Accretion Flows. *ApJ 500* (June 1998), 978–991.

[100] Quataert, E., and Gruzinov, A. Turbulence and Particle Heating in Advection-dominated Accretion Flows. *ApJ 520* (July 1999), 248–255.

[101] Rafferty, D. A., McNamara, B. R., and Nulsen, P. E. J. The Regulation of Cooling and Star Formation in Luminous Galaxies by Active Galactic Nucleus Feedback and the Cooling-Time/Entropy Threshold for the Onset of Star Formation. *ApJ 687* (Nov. 2008), 899–918.

[102] Rafferty, D. A., McNamara, B. R., Nulsen, P. E. J., and Wise, M. W. The Feedback-regulated Growth of Black Holes and Bulges through Gas Accretion and Starbursts in Cluster Central Dominant Galaxies. *ApJ 652* (Nov. 2006), 216–231.

[103] Rampadarath, H., Garrett, M. A., Józsa, G. I. G., Muxlow, T., Oosterloo, T. A., Paragi, Z., Beswick, R., van Arkel, H., Keel, W. C., and Schawinski, K. Hanny's Voorwerp . Evidence of AGN activity and a nuclear starburst in the central regions of IC 2497. *AAP 517* (July 2010), L8.

[104] Ranalli, P., Comastri, A., Origlia, L., and Maiolino, R. A deep X-ray observation of M82 with XMM-Newton. *MNRAS 386* (May 2008), 1464–1480.

[105] Randall, S., Nulsen, P., Forman, W. R., Jones, C., Machacek, M., Murray, S. S., and Maughan, B. Chandra's View of the Ram Pressure Stripped Galaxy M86. *ApJ 688* (Nov. 2008), 208–223.

[106] Roberts, S. R., Jiang, Y.-F., Wang, Q. D., and Ostriker, J. P. Towards Self-Consistent Modelling of the Sgr A* Accretion Flow: Linking Theory and Observation. *ArXiv e-prints* (Oct. 2016).

[107] Roberts, S. R., and Wang, Q. D. X-ray emission from charge exchange in the Cygnus Loop SNR. *MNRAS 449* (May 2015), 1340–1346.

[108] Różańska, A., Mróz, P., Mościbrodzka, M., Sobolewska, M., and Adhikari, T. P. X-ray observations of the hot phase in Sagittarius A*. *A&A 581* (Sept. 2015), A64.

[109] Rubin, V. C., and Ford, Jr., W. K. Rotation of the Andromeda Nebula from a Spectroscopic Survey of Emission Regions. *ApJ 159* (Feb. 1970), 379.

[110] Sartori, L. F., Schawinski, K., Koss, M., Treister, E., Maksym, W. P., Keel, W. C., Urry, C. M., Lintott, C. J., and Wong, O. I. Extended X-ray emission in the IC 2497 - Hanny's Voorwerp system: energy injection in the gas around a fading AGN. *MNRAS 457* (Apr. 2016), 3629–3636.

[111] Schawinski, K., Koss, M., Berney, S., and Sartori, L. F. Active galactic nuclei flicker: an observational estimate of the duration of black hole growth phases of $\sim 10^5$ yr. *MNRAS 451* (Aug. 2015), 2517–2523.

[112] Schödel, R., Morris, M. R., Muzic, K., Alberdi, A., Meyer, L., Eckart, A., and Gezari, D. Y. The mean infrared emission of Sagittarius A*. *AAP 532* (Aug. 2011), A83.

[113] Schurch, N. J., Warwick, R. S., Griffiths, R. E., and Kahn, S. M. The complex soft X-ray spectrum of NGC 4151. *MNRAS 350* (May 2004), 1–9.

[114] Schwarz, G. Estimating the Dimension of a Model. *Annals of Statistics 90* (1978), 461–464.

[115] Serabyn, E., Carlstrom, J., Lay, O., Lis, D. C., Hunter, T. R., Lacy, J. H., and Hills, R. E. High-Frequency Measurements of the Spectrum of Sagittarius A*. *ApJL 490* (Nov. 1997), L77–L81.

[116] Shcherbakov, R. V., and Baganoff, F. K. Inflow-Outflow Model with Conduction and Self-consistent Feeding for Sgr A*. *ApJ 716* (June 2010), 504–509.

[117] Shen, Y., Greene, J. E., Ho, L. C., Brandt, W. N., Denney, K. D., Horne, K., Jiang, L., Kochanek, C. S., McGreer, I. D., Merloni, A., Peterson, B. M., Petitjean, P., Schneider, D. P., Schulze, A., Strauss, M. A., Tao, C., Trump, J. R., Pan, K., and Bizyaev, D. The Sloan Digital Sky Survey Reverberation Mapping Project: No Evidence for Evolution in the M_{SMBH} -σ_* Relation to z $\sim$ 1. *ApJ 805* (June 2015), 96.

[118] Shigeyama, T. Resonance Line Scattering Modifies X-Ray Surface Brightness of Elliptical Galaxies. *ApJ 497* (Apr. 1998), 587–593.

[119] Sironi, L., and Spitkovsky, A. Relativistic Reconnection: An Efficient Source of Non-thermal Particles. *ApJL 783* (Mar. 2014), L21.

[120] Smith, R. K., Chen, G.-X., Kirby, K., and Brickhouse, N. S. A New Calculation of Ne IX Line Diagnostics. *ApJ 700* (July 2009), 679–683.

[121] Strickland, D. K., and Stevens, I. R. Starburst-driven galactic winds - I. Energetics and intrinsic X-ray emission. *MNRAS 314* (May 2000), 511–545.

[122] Su, Y., and Irwin, J. A. Investigating the Potential Dilution of the Metal Content of Hot Gas in Early-type Galaxies by Accreted Cold Gas. *ApJ 766* (Mar. 2013), 61.

[123] Tang, S., and Wang, Q. D. Missing-iron problem and Type Ia supernova enrichment of hot gas in galactic spheroids. *MNRAS 408* (Oct. 2010), 1011–1019.

[124] Tang, S., Wang, Q. D., Mac Low, M.-M., and Joung, M. R. Type Ia supernova-driven Galactic bulge wind. *MNRAS 398* (Sept. 2009), 1468–1482.

[125] Tombesi, F., Cappi, M., Reeves, J. N., Palumbo, G. G. C., Yaqoob, T., Braito, V., and Dadina, M. Evidence for ultra-fast outflows in radio-quiet AGNs. I. Detection and statistical incidence of Fe K-shell absorption lines. *AAP 521* (Oct. 2010), A57.

[126] Townsley, L. K., Broos, P. S., Chu, Y.-H., Gruendl, R. A., Oey, M. S., and Pittard, J. M. The Integrated Diffuse X-ray Emission of the Carina Nebula Compared to Other Massive Star-forming Regions. *ApJS 194* (May 2011), 16.

[127] Tsuru, T. G., Ozawa, M., Hyodo, Y., Matsumoto, H., Koyama, K., Awaki, H., Fujimoto, R., Griffiths, R., Kilbourne, C., Matsushita, K., Mitsuda, K., Ptak, A., Ranalli, P., and Yamasaki, N. Y. X-Ray Spectral Study of the Extended Emission, 'the Cap', Located 11.6kpc above the Disk of M82. *PASJ 59* (Jan. 2007), 269–282.

[128] van der Heyden, K. J., Bleeker, J. A. M., Kaastra, J. S., and Vink, J. High resolution spectroscopy and emission line imaging of DEM L 71 with XMM-Newton. *AAP 406* (July 2003), 141–148.

[129] Vogelsberger, M., Genel, S., Springel, V., Torrey, P., Sijacki, D., Xu, D., Snyder, G., Nelson, D., and Hernquist, L. Introducing the Illustris Project: simulating the coevolution of dark and visible matter in the Universe. *MNRAS 444* (Oct. 2014), 1518–1547.

[130] Wang, Q. D. X-raying galaxies: A Chandra legacy. *PNAS 107* (Apr. 2010), 7168–7173.

[131] Wang, Q. D., Nowak, M. A., Markoff, S. B., Baganoff, F. K., Nayakshin, S., Yuan, F., Cuadra, J., Davis, J., Dexter, J., Fabian, A. C., Grosso, N., Haggard, D., Houck, J., Ji, L., Li, Z., Neilsen, J., Porquet, D., Ripple, F., and Shcherbakov, R. V. Dissecting X-ray-Emitting Gas Around the Center of Our Galaxy. *Science 341* (Aug. 2013), 981–983.

[132] Werner, N., Zhuravleva, I., Churazov, E., Simionescu, A., Allen, S. W., Forman, W., Jones, C., and Kaastra, J. S. Constraints on turbulent pressure in the X-ray haloes of giant elliptical galaxies from resonant scattering. *MNRAS 398* (Sept. 2009), 23–32.

[133] White, C. J., Stone, J. M., and Gammie, C. F. An Extension of the Athena++ Code Framework for GRMHD Based on Advanced Riemann Solvers and Staggered-mesh Constrained Transport. *ApJS 225* (Aug. 2016), 22.

[134] White, S. D. M., and Frenk, C. S. Galaxy formation through hierarchical clustering. *ApJ 379* (Sept. 1991), 52–79.

[135] Woo, J.-H., and Urry, C. M. Active Galactic Nucleus Black Hole Masses and Bolometric Luminosities. *ApJ 579* (Nov. 2002), 530–544.

[136] Xie, F.-G., and Yuan, F. The Influences of Outflow on the Dynamics of Inflow. *ApJ 681* (July 2008), 499–505.

[137] Xu, H., Kahn, S. M., Peterson, J. R., Behar, E., Paerels, F. B. S., Mushotzky, R. F., Jernigan, J. G., Brinkman, A. C., and Makishima, K. High-Resolution Observations of the Elliptical Galaxy NGC 4636 with the Reflection Grating Spectrometer on Board XMM-Newton. *ApJ 579* (Nov. 2002), 600–606.

[138] Yuan, F., Bu, D., and Wu, M. Numerical Simulation of Hot Accretion Flows. II. Nature, Origin, and Properties of Outflows and their Possible Observational Applications. *ApJ 761* (Dec. 2012), 130.

[139] Yuan, F., Gan, Z., Narayan, R., Sadowski, A., Bu, D., and Bai, X.-N. Numerical Simulation of Hot Accretion Flows. III. Revisiting Wind Properties Using the Trajectory Approach. *ApJ 804* (May 2015), 101.

[140] Yuan, F., and Narayan, R. Hot Accretion Flows Around Black Holes. *ARAA 52* (Aug. 2014), 529–588.

[141] Yuan, F., Quataert, E., and Narayan, R. Nonthermal Electrons in Radiatively Inefficient Accretion Flow Models of Sagittarius A*. *ApJ 598* (Nov. 2003), 301–312.

[142] Yuan, F., Wu, M., and Bu, D. Numerical Simulation of Hot Accretion Flows. I. A Large Radial Dynamical Range and the Density Profile of Accretion Flow. *ApJ 761* (Dec. 2012), 129.

[143] Yuan, Q., and Wang, Q. D. A systematic Chandra study of Sgr A* - I. X-ray flare detection. *MNRAS 456* (Feb. 2016), 1438–1450.

[144] Yusef-Zadeh, F., Wardle, M., Schödel, R., Roberts, D. A., Cotton, W., Bushouse, H., Arendt, R., and Royster, M. Sgr A* and Its Environment: Low-mass Star Formation, the Origin of X-Ray Gas and Collimated Outflow. *ApJ 819* (Mar. 2016), 60.

[145] Zhang, S., Wang, Q. D., Foster, A. R., Sun, W., and Li, Z. Recombining Hot Plasma in Galactic Bulges as a Diagnostic of Past AGN Activities - 0.8 Ms RGS Spectra Suggest an Active Nucleus in Andromeda 0.4 Myrs Ago. (In Preparation).

[146] Zhang, S., Wang, Q. D., Ji, L., Smith, R. K., Foster, A. R., and Zhou, X. Spectral Modeling of the Charge-exchange X-Ray Emission from M82. *ApJ 794* (Oct. 2014), 61.

[147] Zhao, J.-H., Young, K. H., Herrnstein, R. M., Ho, P. T. P., Tsutsumi, T., Lo, K. Y., Goss, W. M., and Bower, G. C. Variability of Sagittarius A*: Flares at 1 Millimeter. *ApJL 586* (Mar. 2003), L29–L32.

[148] Zhdankin, V., Werner, G. R., Uzdensky, D. A., and Begelman, M. C. Kinetic turbulence in relativistic plasma: from thermal bath to non-thermal continuum. *ArXiv e-prints* (Sept. 2016).

[149] Zwicky, F. Die Rotverschiebung von extragalaktischen Nebeln. *Helvetica Physica Acta 6* (1933), 110–127.